DLR-IB-AT-KP-2016-197

Development and Validation of an End-to-End Simulator for Frequency Scanning Filtered Rayleigh Scattering Techniques

Masterarbeit

Konstantin Cheishvili

Deutsches Zentrum
für Luft- und Raumfahrt

M.Sc. Thesis

Aerodynamics

Konstantine Cheishvili

TU Delft | Faculty of Aerospace Engineering
Department of Aerodynamics and Wind Energy

DLR | Institute of Propulsion Technology
Department of Measurement Systems

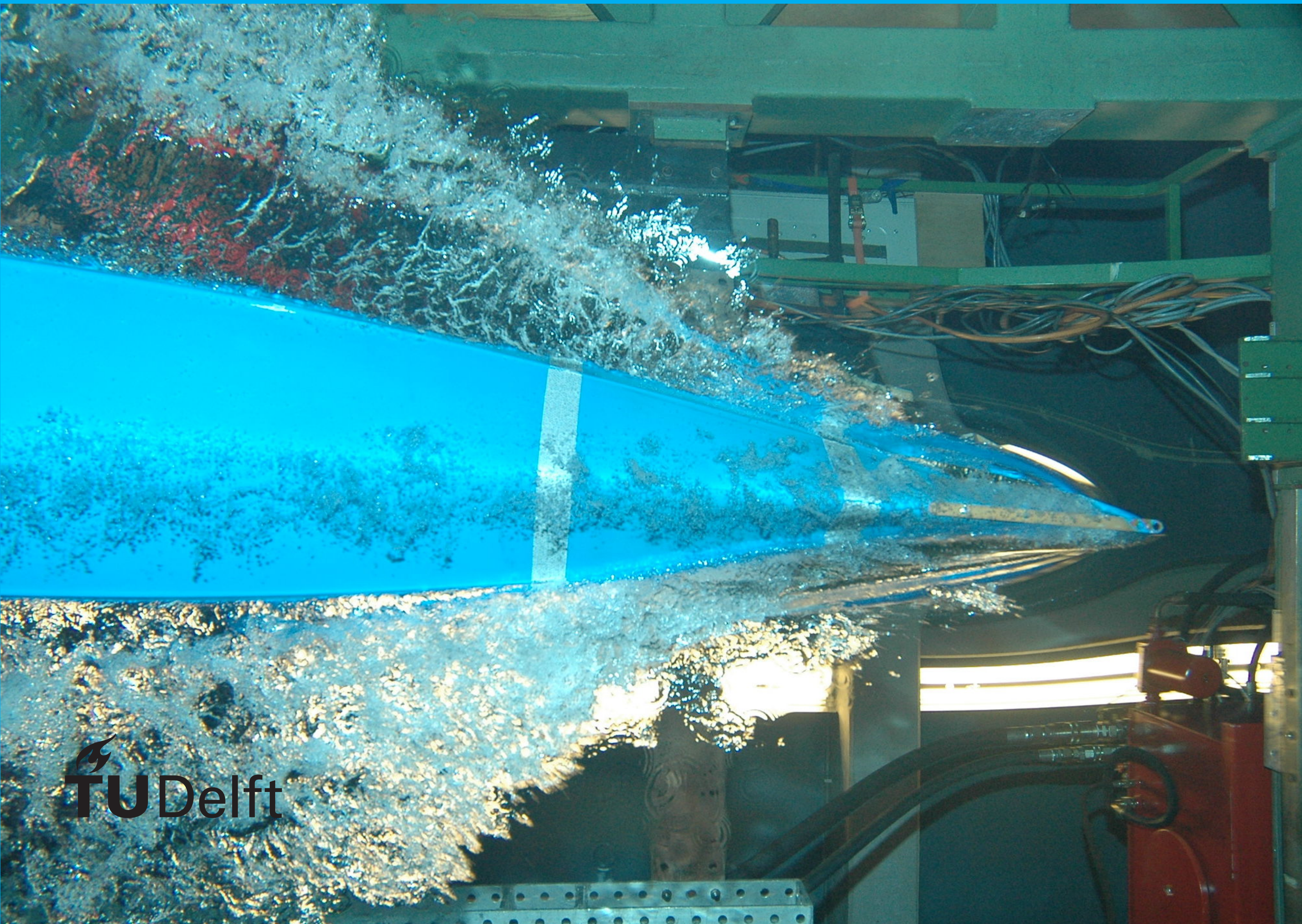

Development and Validation of an End-to-End Simulator for Frequency Scanning Filtered Rayleigh Scattering Techniques

by

Konstantine Cheishvili

to obtain the degree of Master of Science
at the Delft University of Technology,
to be defended publicly on Wednesday August 17, 2016 at 13:00.

Student number:	4416309	
Project duration:	December 1, 2015 – August 31, 2016	
Thesis committee:	Dr. rer. nat. Guido Stockhausen,	supervisor, DLR
	Dr. ir. B. W. van Oudheusden,	chairman, TU Delft
	Dr. ir. F. F. J. Schrijer,	supervisor, TU Delft
	Dr. G. A. Bohlin,	TU Delft

Preface

The German Aerospace Center, abbreviated as DLR, is Germany's national center for aeronautics and space. Its research work is focused on aeronautics, space, energy, transport, defense and security. DLR also plans and implements Germany's space program. It conducts research into Earth and the Solar System, develops eco-friendly technologies to preserve our environment, and enhances power supply, mobility, communication and security.

This master thesis project is conducted at the Department of Measurement Technology at the DLR Institute of Propulsion Technology within project 'OSIRIS' in Cologne, Germany. Optical Sensors for InstRuments In Flight Systems (OSIRIS) is a project of wide context which aims to developing novel flow measurement methods based on laser sources that could be used on airplanes during a flight. This thesis is focused on a frequency scanning method of filtered Rayleigh scattering (FSM-FRS) and its application as a potential in-flight flow measurement technique for determining airplane velocity, off board air pressure and temperature. Being the first stage of the project, this work is limited to a numerical study. The idea is to develop and then validate an end-to-end (e2e) simulator that can be used to investigate different FSM-FRS approaches and optimize them based on the expected measurement accuracies.

Konstantine Cheishvili
Delft, August 2016

Acknowledgements

I thank my supervisors, Dr. rer. nat. Guido Stockhausen and Dr. ir. F. F. J. Schrijer. Without your constant encouragement, support, and advice, I would never been able to complete this thesis. I also thank my co-workers from the Department of Measurement Technology at the DLR for being always very friendly and helpful to me. My special thanks go to Dr. Ulrich Doll and Eike Burow for supervising and tolerating me for many months. I must say, I have never enjoyed working as much as I did at DLR. From a personal standpoint, I would like to thank my friends and family for having faith and believing in me, even when I was doubting myself.

Contents

List of Figures

List of Tables

List of Symbols

Abbreviations

$1C$	One velocity component
$3C$	Three velocity components
DLR	German Aerospace Center
$e2e$	End-to-End
FRS	Filtered Rayleigh Scattering
$FSM-FRS$	Frequency Scanning Method of Filtered Rayleigh Scattering
PCF	Photonic Crystal Fiber
SNR	Signal-to-Noise Ratio

Greek Symbols

α	Probe geometry angle	$[^\circ]$
$\alpha(\nu)$	Filter absorption coefficient	$[-]$
β	Angle between laser polarization direction and z-axis	$[^\circ]$
$\Delta\nu_D$	Net Doppler shift	$[Hz]$
Δx	Percent statistical error in x $(u,\ v,\ w,\ T,$ or $P)$	$[\%]$
$\Delta_\Omega x$	Small lens angle assumption error in x $(u,\ v,\ w,\ T,$ or $P)$	$[m/s,\ K,$ or $Pa]$
ϵ	Optical efficiency	$[\%]$
η	Quantum efficiency	$[\%]$
$\frac{\partial\sigma_{ash}}{\partial\Omega}$	Ash particle differential scattering cross section	$[m^2]$
$\frac{\partial\sigma}{\partial\Omega}$	Diatomic molecule differential scattering cross section	$[m^2]$
κ	Confocal ellipsoid parameter	$[-]$
λ	Wavelength	$[m]$
ν	Frequency	$[Hz]$
ν_c	Laser frequency	$[Hz]$

Ω	Lens solid angle	$[sr]$
ϕ	Angle between laser polarization vector and observation direction	$[^\circ]$
ρ	Ash particle density	$[kg/m^3]$
ρ_0	Depolarization factor	$[-]$
σ	Total scattering cross section	$[m^2]$
σ_L	Laser power standard deviation	$[W]$
σ_l	Laser lineshape standard deviation	$[Hz]$
σ_x	Statistical standard deviation in x ($u,\ v,\ w,\ T,$ or P)	$[m/s,\ K,$ or $Pa]$
σ_ν	Laser frequency measurement standard deviation	$[Hz]$
σ_f	Ash particle scattering profile standard deviation	$[Hz]$
τ	Total filter transmission	$[-]$
τ_b	Filter transmission due to bound state transitions	$[-]$
τ_u	Filter transmission due to unbound state transitions	$[-]$
θ	Scattering angle	$[^\circ]$
θ_y	Angle between observation direction and y-axis	$[^\circ]$
θ_z	Angle between observation direction and z-axis	$[^\circ]$
ε	Molar attenuation coefficient	$[m^2/mol]$
φ	Integration variable	$[rad]$

Latin Symbols

$\hat{L}$	Laser propagation direction	$[-]$
$\hat{O}$	Observation direction	$[-]$
$\hat{P}$	Total Rayleigh scattered light power per steradian	$[W/sr]$
$\hat{v}$	Airplane velocity vector	$[m/s]$
$\mathrm{d}t$	Light collection time	$[s]$
a	Modulation amplitude	$[Hz]$
A_T	Temperature dependent coefficient	$[-]$
B_T	Temperature dependent coefficient	$[-]$
c	Concentration	$[mol/m^3]$

C_0	Frequency dependent coefficient	$\left[W \cdot s^4 \cdot Pa \cdot Sr \cdot m^{-1} \cdot kg^{-2}\right]$
c_L	Speed of light in vacuum	$\left[299,792,458\ m/s\right]$
C_T	Temperature dependent coefficient	$\left[-\right]$
D	Lens diameter	$\left[m\right]$
d	Scattering particle diameter	$\left[m\right]$
D_L	Laser beam diameter	$\left[m\right]$
D_T	Temperature dependent coefficient	$\left[-\right]$
f	Lens focal length	$\left[m\right]$
$f_\#$	Lens f-number	$\left[-\right]$
f_m	Modulation frequency	$\left[Hz\right]$
g	Rayleigh-Brillouin scattering profile	$\left[-\right]$
g_{ash}	Ash particle scattering profile	$\left[-\right]$
h	Planck's constant	$\left[6.62607 \times 10^{-34}\ J \cdot s\right]$
H_n	Fourier coefficients	$\left[-\right]$
I_L	Laser intensity	$\left[W/m^2\right]$
k_B	Boltzmann constant	$\left[1.38065 \times 10^{-23}\ m^2 \cdot kg \cdot s^{-2} \cdot K^{-1}\right]$
L	Filter length	$\left[m\right]$
m	Scattering particle mass	$\left[kg\right]$
N	Number density of scattering particles	$\left[m^{-3}\right]$
n	Index of refraction	$\left[-\right]$
N_{MC}	Number of Monte Carlo simulations	$\left[-\right]$
N_{PE}	Number of photoelectrons	$\left[-\right]$
P	Pressure	$\left[Pa\right]$
P_L	Laser power	$\left[W\right]$
P_R	Total collected Rayleigh scattered light power	$\left[W\right]$
P_{Rf}	Collected Rayleigh scattered light power spectral profile	$\left[W\right]$
P_r	Room pressure	$\left[Pa\right]$
P_s	Settling chamber pressure	$\left[Pa\right]$

R	Ideal gas constant	$\left[8.31446\ J \cdot K^{-1} \cdot mol^{-1}\right]$
R_F	Calibration factor	$\left[W \cdot s^4 \cdot K \cdot Sr \cdot m^{-1} \cdot kg^{-2}\right]$
S_0	Frequency dependent coefficient	$[-]$
S_1	Frequency dependent coefficient	$[-]$
S_2	Frequency dependent coefficient	$[-]$
T	Temperature	$[K]$
t	Time	$[s]$
T_F	Filter temperature	$[^\circ C]$
T_m	Modulation period	$[s]$
T_c	Flow potential core temperature	$[K]$
T_r	Room temperature	$[K]$
T_s	Settling chamber temperature	$[K]$
u	Airplane forward velocity component	$[m/s]$
u_D	Doppler velocity	$[m/s]$
u_N	Flow core velocity	$[m/s]$
V	Interrogation volume	$[m^3]$
v	Airplane side velocity component	$[m/s]$
V_p	Ash particle volume	$[m^3]$
w	Airplane vertical velocity component	$[m/s]$
w_0	Beam waist radius	$[m]$
WN	Wavenumber	$[cm^{-1}]$
Y	Tenti S6 model parameter	$[-]$
${N_{PE}}'$	1st harmonic of N_{PE}	$[-]$
${N_{PE}}''$	2nd harmonic of N_{PE}	$[-]$
${N_{PE}}^R$	Intensity independent signal ratio	$[-]$
${S_L}'$	1st harmonic of $\tau(\nu)$	$[-]$
${S_L}''$	2nd harmonic of $\tau(\nu)$	$[-]$

1

Introduction

There are numerous flow measurement techniques and sensors used today based on different architectures, such as mechanical flow meters, pressure-based meters, optical flow meters, etc. Most of the measurement methods deliver only a single flow parameter like temperature, pressure or a velocity component. Some of them can be used to measure two parameters simultaneously. However, almost none of the methods are applicable for measuring the three mentioned flow parameters at the same time. Also, many techniques imply physically inserting a probe in the flow that alters the flow and adversely affects the measurement uncertainty.

A non-intrusive and seeding free flow measurement technique that allows simultaneous measurements of temperature, pressure, and one velocity component of a flow is filtered Rayleigh scattering (FRS). FRS is an optical measurement method based on laser light scattering and was conceived in the late 20th century. The underlying principle of FRS is a molecular Rayleigh scattering. When narrow-bandwidth laser light passes through a gas medium, the molecules scatter the light elastically. The scattered light is shifted and broadened in the frequency domain by the Doppler effect due to bulk and thermal motion of the gas molecules (Mielke et al. 2005). The frequency composition of the scattered light contains the information about gas temperature, pressure, and the bulk velocity. The scattered light passes through a filter before it is analyzed to suppress laser light reflections as well as scattering from large particles travelling with the flow.

1.1. Motivation

Flow measurement sensors based on FRS have the potential to be used in both scientific and industrial applications. Measurements of thermodynamic properties and bulk velocity can be utilized to study the flow behaviour. FRS probes can be applied as measurement sensors in technical flows, transportation, buildings, etc. The project OSIRIS views this technique as a potential replacement or backup to conventional sensors on board of airplanes. Reliable knowledge of aircraft speed, outside air temperature, density, and pressure is essential at every phase of the flight. These parameters are crucial for control purpose and also represent an input to the autopilot. Current airliners' airspeed measurement architecture is based on varying and redundant sensor systems (total pressure sensors, static pressure sensors and temperature sensors, air pressure ducts, ADM transducers, ADR reference unit computers) (Barny 2010). Such independent 'chains' of airspeed measurement units are provided for both the Captain and the First Officer. For safety reasons, an additional 'standby' channel is required. This allows the crew to replace the failing system by a backup one. However, both the primary and the secondary channels are based on similar architecture with comparable failure modes. To improve this redundancy, novel measurement approaches must be investigated.

The proposed FRS device is composed of light emitting and receiving units. The emitter produces a focused laser beam which illuminates a certain measurement volume. A portion of this light is scattered by the gas molecules towards the receiving unit, which collects, records and processes its spectral properties. These data are analyzed using a signal processing software, yielding the desired flow parameters.

The use of FRS can significantly reduce the probability that a common failure mode occurs. Prevalent problems associated with pitot tubes (pressure-sensitive instruments used for measuring airplane velocity) are related to blockage or mechanical damage due to icing, dust, bird strike, etc. The pitot tubes are placed outside of the airframe, they are invasive and alter the flow field. This is not favorable for the aerodynamics. In addition, they are affected by the boundary layer of the airplane. The FRS hardware would be placed inside the cabin, with the laser focused through a window. Icing is a potential error source as it is with pitot tubes, however heating up a window is much easier than an off board sensor. Besides, laser based sensors are non-invasive. They do not affect the airflow, and are not affected by external factors such as bird strike and blockage. However, due to its complex physics and hardware setup, the FRS needs additional research and refinement before entering commercial service.

There are several approaches how to conduct measurements of multiple parameters via FRS, and they can be divided into two groups: interferometric and non-interferometric. An in-flight FRS measurement system must be robust and dependable to be fully functional on board of an airplane. This is especially challenging for FRS methods relying on etalons and interferometers that are problematic to stabilize. General robustness of a setup is also a desirable quality for any experiment. Based on the literature study (Konstantine, 2016) frequency scanning methods of FRS (FSM-FRS) were identified as the possible non-interferometric candidates to measure all three flow parameters simultaneously. Different FSM-FRS approaches were conceived by Grinstead et. al (1998), Mach & Varghese (1999), Jagodzinski (2007), and Doll et. al. (2014). While there are several approaches to FSM-FRS, this thesis is focused on developing an end-to-end (e2e) simulator that can predict the measurement uncertainties of different FSM-FRS techniques and setup options. Based on this platform, FSM-FRS probes can most efficiently be optimized in advance with respect to specific measurement cases or experiments. This is fundamental because FSM-FRS setups are complex and there are numerous factors that are decisive for the accuracy and need to be considered.

1.2. Requirements & Goals

As already mentioned, the presented end-to-end simulator can be applied to any FSM-FRS experiment. However, the inspiration for developing this software and its first practical application comes from the OSIRIS project. Since it is about optimizing the in-flight FSM-FRS probe based on calculated (predicted) measurement uncertainties, there are some requirements proposed by the DLR. In order for the FSM-FRS technique to be usable in-flight and also to be competitive with conventional measurement devices, these requirements

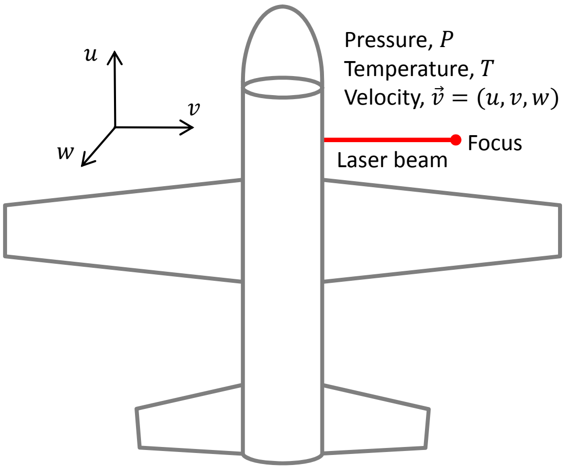

Figure 1.1: In-flight FRS geometry

need to be fulfilled.

First of all, the FSM-FRS probe must measure temperature, pressure, and three velocity components, $\hat{v} = (u, v, w)$, as shown in Fig. 1.1. This should be done in real time. Since most of the flight time is spent in a cruise condition at around 10 km altitude from the sea level, the FSM-FRS probe is going to be optimized for this flight stage. The air temperature and pressure are around 225 K and 26500 Pa at this altitude (The Engineering Toolbox, 2016). A forward velocity component, u, is around 250 m/s. Other perpendicular components are around 25 m/s. Obviously, these numbers are not constants and change throughout the flight. However, the idea is to have the rough estimates of the thermodynamic parameters and the velocity vector for which the FSM-FRS probe can be optimized. The desired accuracies in these parameters are given in terms of statistical standard deviations and they are listed in table 1.1. These numbers come from the aviation industry. In order to allow the FRS probes (or other measurement sensors) to be used on board of airplanes, these accuracy goals must be fulfilled. However, it must be noted that achieving the given accuracy requirements is not imperative for the OSIRIS project at this stage. It is more important is to show the potential of the FSM-FRS technique. The temporal resolution of the measurements must be at least 1 Hz. In order to apply the technique through airplane windows, the light collection optics should fit inside a 15 cm diameter window, and a working distance of 25 cm (laser focused from optics) can be assumed, i.e. laser focus is 25 cm outside of a plane window. This ensures that the focal point is outside of the plane's boundary layer. At 25 cm away from the airframe the local velocity is still affected by the presence of the aircraft. However, this velocity is still closer to a freestream value than the one measured by

Parameter	Accuracy (σ)
Velocity (u)	± 0.33 m/s
Velocity (v, w)	± 0.18 m/s
Temperature	± 0.45 K
Pressure	± 11 Pa

Table 1.1: OSIRIS project accuracy goals

pitot tubes. In addition, it is possible to choose the most optimal window where the airflow deflection is minimal.

The scattering medium is air. However, in addition, it is provided that there are 10000 aerosol particles per cubic centimeter of air at this altitude which scatter the light as well. Again, this number comes from the aviation industry and any measurement system must be able to cope with this. These particles are a combination of the volcanic ash and water droplets. Their diameter is approximately 10 nm and they have a density (index of refraction) similar to the water.

The main goal of OSIRIS is not to find the best alternative to current on-board measurement systems, but to see whether the FSM-FRS method could be useful and theoretically competitive with conventional devices, that is, if it can potentially fulfill the above mentioned requirements in the parameter accuracy. Even though the main direction of the research has been chosen by DLR, there are various approaches to the FSM-FRS that need to be investigated.

1.3. Convention

The master thesis is about an optical flow measurement method based on lasers. Therefore, quantities such as a light wavelength λ and frequency ν are frequently used. The light wavelength and frequency are related by:

$$c_L = \lambda \nu \tag{1.1}$$

where c_L is a speed of light. Sometimes, it is more convenient to use a term called wavenumber. The light wavenumber WN given in cm^{-1}, is related to its wavelength by:

$$WN = \frac{1}{\lambda \cdot 100} \tag{1.2}$$

where λ is given in meters. Throughout this thesis, these three quantities are used interchangeably.

2

Research Objectives

Literature review on the subject (Konstantine, 2016) showed the potential of FSM-FRS as a viable and appealing non-interferometric FRS method to perform simultaneous measurements of pressure, temperature, and velocity of a flow. There were two main reasons: a possibility to simultaneously measure pressure, temperature, and velocity of a flow and a feasibility to implement the FSM-FRS based probes on board of airplanes. FSM-FRS is a complex flow measurement technique. It has many variables regarding geometry, optics and laser sources that could be optimized. As the name suggests, it relies on scanning the incident laser frequency and then recording the Rayleigh scattered light signal. There are only a handful of research groups worldwide working with this technique and investigating different approaches. However, there is no tool which could be used for designing and optimizing FSM-FRS experiments.

The main objective of this thesis is to bring together known FSM-FRS methods, complement them with new approaches, and fill remaining knowledge gaps. The resulting end-to-end simulator predicts accuracies for the different methods in pressure, temperature, and velocity of a flow depending on varying experimental parameters. This simulator is going to be a very useful tool and an asset for the FRS community. It can be used to optimize different parameters and set up the best possible FSM-FRS experiment for a given flow case. It can be viewed as a possible way to realize the full potential of the FSM-FRS techniques.

Another important objective is to use e2e simulator to conceptualize and optimize the FSM-FRS probe for the DLR project OSIRIS which is aimed on measuring temperature, pressure, and all three components of the plane velocity in-flight. This will demonstrate the software capabilities. Based on the results, it can be decided whether or not FSM-FRS techniques have a potential as in-flight flow measurement devices. Important questions to answer are:

- What are the possible frequency scanning FRS techniques and which one performs best in terms of the expected measurement accuracies?
- What is a possible FSM-FRS probe layout for measuring a temperature, pressure, and a single or multiple velocity component(s)?
- Which variables regarding geometry, optics, laser sources, and other FSM-FRS parameters can be optimized and what is an efficient procedure for doing so?

- What is the optimal configuration for measuring all three velocity components?
- To what extent do the expected accuracies in the flow parameters fulfill the OSIRIS requirements?
- To what extent is it possible to validate the end-to-end simulator?

These questions will be qualitatively answered in the next chapters of the thesis.

2.1. Thesis Outline

- **Chapter 1** starts with an introduction to FSM-FRS, explaining why the thesis is focused on this technique, and what the motivation is. It also discusses the DLR project OSIRIS and its importance for this research.
- **Chapter 2** mentions the main thesis objectives.
- **Chapter 3** includes the theoretical foundations of the end-to-end simulator and the FSM-FRS techniques. It also touches upon the FSM-FRS approaches found in literature.
- **Chapter 4** reviews the end-to-end simulator, its functionality, and shows how the uncertainty analysis is performed. The OSIRIS specific information and features are also included.
- **Chapter 5** presents the simulation results obtained using the end-to-end simulator. Optimizations for 1C (for measuring single velocity component) and 3C (for measuring all three velocity components) FSM-FRS probes in the context of the OSIRIS are given.
- **Chapter 6** reviews the experiment performed to validate the end-to-end simulator. A comparison between the experiment and e2e simulations is shown.
- **Chapter 7** summarizes the thesis and presents the concluding remarks, as well as the future work that could be done.

3

Theory

3.1. Filtered Rayleigh Scattering

In this section, the theoretical background of FRS is presented. It starts with explaining the physics of Rayleigh scattering and its dependency on the flow parameters, followed by a short review of the devices that can be used for light detection. The section ends by discussing the importance and functions of a filter in the FRS experiment.

3.1.1. Rayleigh Scattering

When laser light with a wavelength λ is incident on a particle with a diameter $d < 0.1\lambda$, elastic light scattering occurs. This process is known as a Rayleigh scattering. The dimensions of molecules and atoms are in the range of Angstroms (10^{-10} m), while the wavelength of visible, ultraviolet, and infrared light is in the range of hundreds of nanometers (10^{-9} m). Therefore, light scattering from molecular or atomic gases is essentially Rayleigh scattering, forming the basis for the FRS technique. For atmospheric studies and an in-flight application of FRS, the scattering medium is air.

The physics of a Rayleigh scattering was described in detail by Forkey (1996) in his PhD thesis. When a laser beam is incident on a region of a flow with pressure P, temperature T, and flow velocity $\vec{v}$, the total Rayleigh scattered light power per steradian from an interrogation volume V is given by:

$$\hat{P}_R = NV\frac{\partial\sigma}{\partial\Omega}I_L \tag{3.1}$$

where I_L is the laser intensity, N is the number density of the scatterers, and $\frac{\partial\sigma}{\partial\Omega}$ is the total differential Rayleigh scattering cross section. The typical Rayleigh scattering geometry is depicted in Fig. 3.1. Here, $\hat{L}$ is the laser beam propagation direction, $\hat{O}$ is the observation direction along which the scattered light is collected or observed, and θ is the angle between these vectors, also known as the scattering angle. By further assuming that the ideal gas law is valid, the following equation can be derived:

$$\hat{P}_R = I_L\frac{PV}{k_B T}\frac{\partial\sigma}{\partial\Omega} \tag{3.2}$$

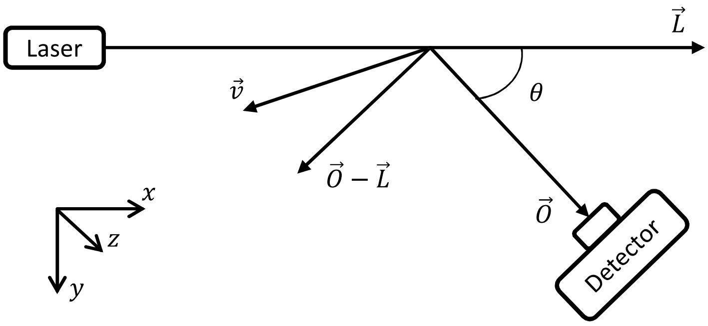

Figure 3.1: Rayleigh scattering geometry

where k_B is a Boltzmann constant. For the diatomic molecules and a linearly polarized incident light, the differential scattering cross section $\frac{\partial\sigma}{\partial\Omega}$ is a function of several angles and also depends on the type of scatterers. A complete description model is given by Miles et al. (2001), according to which, the differential scattering cross section of the diatomic molecules can be calculated using:

$$\frac{\partial\sigma}{\partial\Omega}(\theta_y,\theta_z,\beta)=\frac{3\sigma}{8\pi}\frac{1}{2+\rho_0}\left[\rho_0+(2-2\rho_0)\left(\sin\beta\frac{\cos\theta_y\cos\theta_z}{\sin\theta_z}-\cos\beta\sin\theta_z\right)^2\right] \tag{3.3}$$

where θ_y, θ_z are the angles between the observation direction and y, z-axis, respectively. The laser beam is propagating in the x-direction, and β is the angle between the laser polarization direction and z-axis. ρ_0 is a depolarization factor which depends on the gas composition and the laser wavelength. Bucholtz (1995) provides ρ_0 values for air at atmospheric conditions and for various wavelengths. σ is the total scattering cross section and is given by:

$$\sigma=\frac{32\pi^3(n-1)^2}{3\lambda^4N^2}\left(\frac{6+3\rho_0}{6-7\rho_0}\right) \tag{3.4}$$

where n is the index of refraction of the medium and N is the number density of the molecules. n and N are functions of temperature and pressure. However, n is proportional to N, so they need to be calculated only for one set of values for pressure and temperature, e.g. atmospheric conditions. n is also a function of the wavelength. For an incident laser light with a wavelength more or equal to 230 nm (visible light, near-UV, infrared), the index of refraction of air at atmospheric conditions is given by:

$$(n-1)\times10^8=8060.51+\frac{2480990}{132.274-(1/\lambda)^2}+\frac{17455.7}{39.32957-(1/\lambda)^2} \tag{3.5}$$

So, provided all necessary details, the total Rayleigh scattered power per steradian can be calculated using Eq. 3.2. When Rayleigh scattering is used for diagnostics, the scattered light is collected over a limited solid angle $\Omega=\int_{lens}\mathrm{d}\Omega$ before it is directed towards a detector, as shown in Fig. 3.2. This angle depends on the light collection optics. This results in a modified expression for the total collected scattered power:

$$P_R=I_L\frac{PV}{k_BT}\int_{lens}\frac{\partial\sigma}{\partial\Omega}(\theta_y,\theta_z,\beta)\mathrm{d}\Omega \tag{3.6}$$

The observation direction varies within the lens and so does the differential scattering cross section. So, the integration over the lens solid angle is required. Eq. 3.6 only shows the total

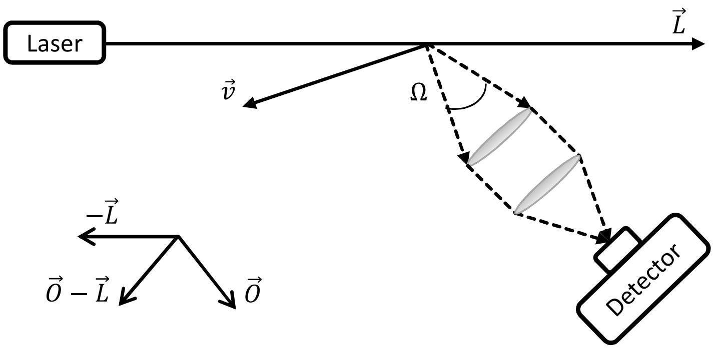

Figure 3.2: Collecting a Rayleigh scattered light

received power, independent of the frequency. It is a single value which does not depend on the flow velocity. Pressure and temperature cannot be determined from a single measured value because there can be multiple combinations of these parameters for the same value of the total power. In reality, the Rayleigh scattered light has a specific frequency composition and is not monochromatic, i.e. it is spectrally broadened. The variation of scattered light power with frequency is given by a function $P_{Rf}(\nu)$. This distribution is sensitive to changes in temperature and pressure of the flow, and in addition the spectral position of the peak strongly depends on the flow velocity. So, in order to obtain the flow parameters, $P_{Rf}(\nu)$ must be determined.

The distribution $P_{Rf}(\nu)$ of Rayleigh scattered light is determined by the spectral profile of the incident laser beam and the Doppler shifts associated with the molecular and bulk motion of the medium. The probability of observing a particular laser frequency, ν, is given by the normalized spectral profile of the laser, $l(\nu-\nu_c)$, centered symmetrically around the origin with ν_c being the laser's central frequency. Spectral profiles of technical lasers typically have a Gaussian, Lorentzian, or Voigt (convolution of Gaussian and Lorentzian functions) shape. When a laser source interrogates a real volume of the molecules, because of their thermal and bulk motion, the molecules are not stationary relative to the laser source. So, each molecule observes a Doppler shifted laser frequency. The detector which detects the scattered light by the molecules observes a second Doppler shift due to the molecular motion relative to it. The thermal molecular motion of the molecules results in a spectrally broadened Rayleigh-Brillouin scattering profile. The scattering profile is centered around the mean (central) scattering frequency $\nu_c+\Delta\nu_D$, where $\Delta\nu_D$ is the net Doppler shift generated by the bulk velocity of the flow that shifts the entire scattering profile.

Spectrally broadened Rayleigh-Brillouin scattering profile can be thought of having two components: one is the central Gaussian profile (thermal broadening) due to a random uncorrelated motion of the molecules, and the other is a triplet of Lorentzian profiles (pressure broadening) arising from correlated motion of the molecules. This correlation is caused by acoustic waves which affect the molecular (atomic) collisions and become stronger as the pressure increases. The resulting scattering profile, denoted by $g(\theta, T, P, \nu)$, depends on flow temperature, pressure, central scattering frequency, and scattering angle. The central scattering frequency is directly related to the flow velocity: in case of a flow with a zero bulk velocity, the Rayleigh-Brillouin scattering profile is centered around the incident laser frequency. However, when the bulk velocity of the molecules is nonzero, the central scattering frequency is Doppler shifted away from the laser frequency. The net Doppler

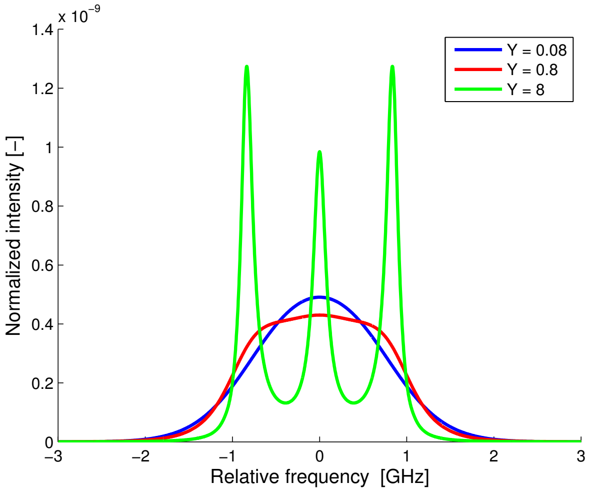

Figure 3.3: Tenti S6 Rayleigh-Brillouin scattering profiles for air

shift $\Delta\nu_D$ can directly be related to one specific directional velocity component which is determined by the directions of light incidence and scattering:

$$\Delta\nu_D(\hat{O},\hat{L},\vec{v}) = \frac{\vec{v}}{\lambda}(\hat{O}-\hat{L}) \tag{3.7}$$

where $(\hat{O}-\hat{L})$ is the vector on which the projection of the velocity is measured. These vectors are clearly shown in Fig. 3.1 and 3.2. It is important to note that $\Delta\nu_D$ is independent of the velocity components perpendicular to $(\hat{O}-\hat{L})$. Also, it must be considered that since the observation direction changes across the lens (when integrating over the lens solid angle), the differential scattering cross section, the observation $(\hat{O})$ and $(\hat{O}-\hat{L})$ directions, the net Doppler shift, and the scattering angle vary within the lens angle. So, in theory, this must be taken into account when calculating the scattered light spectrum. Also, in order to determine all three perpendicular velocity components, at least three separate linearly independent observation directions are required.

In order to relate a Rayleigh-Brillouin scattering profile to thermodynamic parameters of the gas, an appropriate model is needed. The S6 model developed by Tenti et al. (1974) is generally considered to be most accurate for calculating Rayleigh-Brillouin scattering profiles of diatomic gases. In this model, the shape of a profile depends on the thermodynamic state of a gas which is indicated by the so-called Y-parameter. The Y-parameter depends on pressure, temperature, scattering angle and central scattering frequency. More information about the Tenti S6 model, Y-parameter and the origin of the shape of the scattering profile can be obtained from the articles by Tenti et al. (1974) and Forkey et al. (1998). Rayleigh-Brillouin profiles for air, calculated using the Tenti S6 model for various Y-parameters, are given in Fig. 3.3. Here, air temperature is 300 K and pressure values are $0.1\cdot10^5$, $1\cdot10^5$, and $10\cdot10^5$ Pa for Y-parameters of 0.08, 0.8, and 8, respectively. The Y-parameter changes with flow temperature or pressure, and also with the scattering angle. For low Y-parameter values, the spectral profile looks like a Gaussian profile, dominated by thermal broadening where the motion of the molecules is uncorrelated. However, as the Y-parameter increases, the shape of the scattering profile changes more and more into a Lorentzian triplet. This is called the hydrodynamic regime where the motion of the molecules is correlated and the pressure has significant impact on the shape of the scattering profile. Forkey et al. (1998)

define Y-parameter for air as follows:

$$Y = 0.230\left[\frac{T(K)+111}{T(K)^2}\frac{P(\text{atm})\lambda(\text{nm})}{\sin\left(\frac{\theta}{2}\right)}\right] \tag{3.8}$$

The Tenti S6 numerical code is available for various fluids. The only input variables are gas specific constants, temperature, pressure, scattering angle, and central scattering light frequency. So, it can be used to calculate $g(\theta, T, P, \nu)$. The actual Rayleigh scattering lineshape from the interrogation volume, $P_{Rf}(\nu)$, is then given by the convolution of the laser lineshape and the Rayleigh-Brillouin scattering profile multiplied with the total collected scattered power:

$$P_{Rf}(\nu) = I_L\frac{PV}{k_B T}\int_{lens}\frac{\partial\sigma}{\partial\Omega}\int_{-\infty}^{+\infty} l(\nu-(\nu_c+\Delta\nu_D)-\nu')g(\theta,T,P,\nu')\mathrm{d}\nu'\mathrm{d}\Omega \tag{3.9}$$

3.1.2. Detector

Rayleigh scattered light can be spectrally analyzed using etalons or interferometers. These rely on a set of reflective surfaces or mirrors to create an interference pattern which strongly depends on the frequency composition of the light. However, such interferometers are very sensitive to the distance between the reflective surfaces. So, the smallest perturbations in a temperature and pressure or even mechanical vibrations change the distance between the mirrors and significantly affect the measurement accuracy. In a controlled environment such as a laboratory room, it is no problem to stabilize the interferometer. However, for an in-flight application, it is problematic to use a device which is this sensitive to the environment.

Detection of light can be accomplished using devices relying on the photoelectric effect. The effect is the production of electrons or other free carriers when light shines upon a material. These electrons are often called photoelectrons. The most common detectors, utilizing the photoelectric effect to measure a light intensity, are: charge-coupled device (CCD) camera, complementary metal oxide semiconductor (CMOS) camera, photodiode (PD), avalanche photodiode (APD), and photomultiplier tube (PMT). The drawback of these devices is that they can only detect the total light intensity and are insensitive to its frequency. Camera detectors are generally used in imaging. They contain arrays of pixels, and for each pixel incoming photons are converted into electrons and then converted into an intensity value. PMT, APD, and PD detectors have no spatial sensitivity, instead they have one active area and convert all photons that hit this area into electrons. These electrons are then amplified to produce a current or voltage signal. For single point measurements (0D), as required in OSIRIS, PMT, APD, and PD are more viable options because camera detectors are more expensive and complex.

Detectors have different noise sources, the most important: dark noise, read-out noise, and photon shot noise (Jagodzinski, 2007). Dark noise comes from heat and cosmic noise and depends on the exposure or measurement time. The read-out noise originates from digitizing the signal. The photon shot noise is a result of signal fluctuations due to the quantum properties of photons and depends on the square root of the signal level. Another important factor is the quantum efficiency of the detector, describing the probability of photons being converted into the electrons. The number of minimum/maximum photons that can be detected per given time (dynamic range) is also a very significant detail. So, when choosing the detector, one must keep these parameters in mind.

3.1.3. Notch Filter

$P_{Rf}(\nu)$ is the spectral distribution of collected light, which has been scattered by the molecules or atoms under consideration. As described before, its shape and net Doppler shift away from the original laser frequency contain the aspired information about flow velocity, temperature, and pressure. These parameters can easily be determined from a measured $P_{Rf}(\nu)$. However, aerosols and other large particles contained in the measurement volume also scatter light. Since the dimensions of such particles are larger compared to molecules or atoms, they scatter light differently. This process is called Mie scattering. Mie scattering occurs when laser light with wavelength λ is incident on a particle with a diameter $d \geq \lambda$. Because typical aerosols and dust particles are considerably larger, thermal and acoustic broadening effects are minimal. Therefore, the lineshape of the Mie scattered light, when using a single frequency laser as an excitation light source, is very narrow in frequency (almost monochromatic, follows the lineshape of the laser source). The scattering frequency is shifted from the laser frequency by the Doppler shift due to the bulk velocity of the fluid. Because of the large particle size, the Mie scattering signal is very strong, thus it contaminates the Rayleigh scattering signal. If it is possible to actually measure the spectral light distribution then the Mie scattering is not a problem, since the part of the spectrum where it occurs can be left out. However, in FSM-FRS, $P_{Rf}(\nu)$ can not be directly measured and it is determined based on the dependency of the detected scattered light power on the incident laser frequency. So, in order to accurately determine the molecular scattering profile $P_{Rf}(\nu)$, the Mie scattering must be modelled or removed from the signal. Modelling is not as simple because exact concentration and type of the scattering particles are unknown.

Since the spectral lineshape of the Mie scattered light is very narrow, a notch filter can be used to suppress this unwanted signal while still transmitting a significant part of the much broader Rayleigh profile (Miles et. al., 1990; 1991). The notch filter utilized in FRS experiments mostly consists of a glass cell filled with a molecular or atomic vapor (iodine, mercury, potassium, etc.) and it is positioned before the detector, so that the collected scattered light passes through the filter before reaching the detector, as shown in Fig. 3.5. The working principle of such a notch filter is better illustrated in Fig. 3.4. Here, the dashed curve corresponds to the transmission of a molecular filter. The amount of

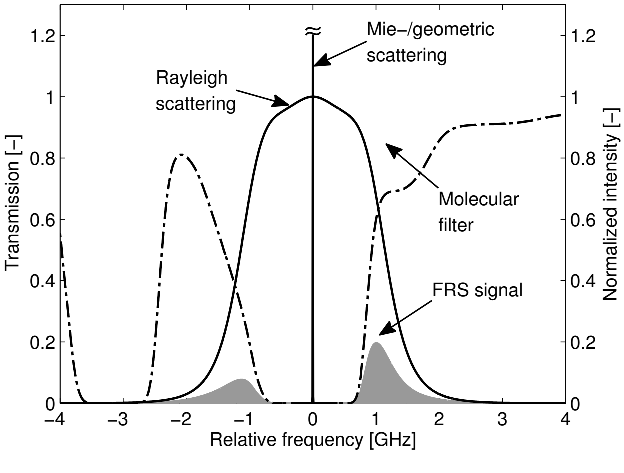

Figure 3.4: Transmission of a notch filter and a Rayleigh spectrum

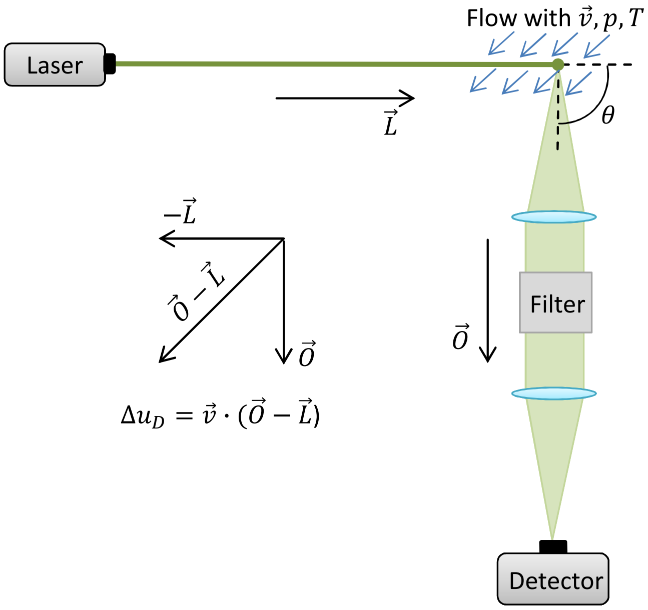

Figure 3.5: Generic FRS setup for measuring the flow parameters

transmission (absorption) depends on the light frequency. The Rayleigh and Mie scattering profiles are also shown. As can be seen, the filter features specific absorption wells where for specific frequency ranges the transmission (the ratio of the transmitted light power to the incident light power) is very low. If the central scattering frequency (Doppler shifted frequency, $\nu + \Delta\nu_D$) is within this absorption well, the Mie scattered light is completely blocked. However, a considerable part of the Rayleigh spectrum is still transmitted. As a rule of thumb, the transmission values within this absorption feature must be lower than 10^{-5} for most technical applications. If the incident light frequency ν_c is also within the filter absorption well, then the reflections and the geometrically scattered portions of the laser light are also very effectively attenuated.

The transmission of the molecular filter $\tau(\nu)$ is a function of the light frequency ν given that the light rays are normal to the surface of the cell. This transmission function of the used filter must be known in advance (numerically and/or empirically). It depends on the filter saturation temperature (temperature at which all molecules are vaporized) and the filter length (Miles et. al., 1992). So, the transmission function can be tuned by adjusting the above-mentioned filter parameters. Since the detector is insensitive to the frequency, it integrates the scattered and then filtered power over all frequencies:

$$P_T = I_L \frac{PV}{k_B T} \int_{lens} \frac{\partial\sigma}{\partial\Omega} \int_{-\infty}^{+\infty} \tau(\nu) \int_{-\infty}^{+\infty} l(\nu - (\nu_c + \Delta\nu_D) - \nu') g(\theta, T, P, \nu') \mathrm{d}\nu' \mathrm{d}\nu \mathrm{d}\Omega \qquad (3.10)$$

Often, the scattered light is collected during a finite time $\mathrm{d}t$. So, instead of using the formula for detected scattered power, it is more convenient to work with the total detected scattered energy E_T which is simply the integral of the scattered power over the collection time $\mathrm{d}t$. The number of Rayleigh-Brillouin scattered photons from an interrogation volume that are collected during the exposure time can be found by dividing E_T by the energy of one scattered photon $h(\nu_c + \Delta\nu_D)$. In reality, only a fraction of these photons actually reach the detector and only a number of them induce the release of a photoelectron from the intensifier surface of the detector. This is determined by the total efficiency of a collection optics ϵ (taking into account the transmission and reflection losses), and the quantum efficiency of the photocathode η. So, for a given incident laser frequency ν_c, the number of photoelectrons N_{PE} emitted due to a filtered Rayleigh scattering signal from an interrogation volume is given by:

$$N_{PE} = \epsilon\eta \frac{I_L \mathrm{d}t}{h(\nu_c + \Delta\nu_D)} \frac{PV}{k_B T} \int_{lens} \frac{\partial\sigma}{\partial\Omega} \int_{-\infty}^{+\infty} \tau(\nu) \int_{-\infty}^{+\infty} l(\nu - (\nu_c + \Delta\nu_D) - \nu') \\ g(\theta, T, P, \nu')\mathrm{d}\nu' \mathrm{d}\nu \mathrm{d}\Omega \tag{3.11}$$

Since the observation direction varies within the collection lens, the net Doppler shift, scattering cross section, and Rayleigh-Brillouin profile are not constant within the lens. Therefore, they need to be integrated over the lens angle as shown in Eq. 3.11. However, by assuming that the incident laser light is monochromatic, and that the lens solid angle is small enough so the variables remain sufficiently constant within the lens, the following equation is derived:

$$N_{PE} = \epsilon\eta \frac{\Omega I_L \mathrm{d}t}{h(\nu_c + \Delta\nu_D)} \frac{PV}{k_B T} \frac{\partial\sigma}{\partial\Omega} \int_{-\infty}^{+\infty} \tau(\nu) g\big(\theta, T, P, \nu - (\nu_c + \Delta\nu_D)\big)\mathrm{d}\nu \tag{3.12}$$

In this case, the observation direction, net Doppler shift, differential scattering cross section, and the Rayleigh-Brillouin profile are defined along the center line of the lens (optical axis). This is a much more useful formula because it is significantly less complex and computationally relatively inexpensive. More about the validity of the assumptions is discussed in section 4.2.1.

3.2. Confocal Imaging

The intensity of Rayleigh scattered light is directly proportional to the volume of an illuminated medium. Knowing this volume is crucial for point (0D) FRS measurements. First of all, the focal volume must be small enough so that variation of the vector quantities within it becomes negligible. Secondly, it must be known in order to simulate the FRS spectrum and calculate the expected number of photoelectrons induced in a detector. The notion of a focal volume depends on how it is defined.

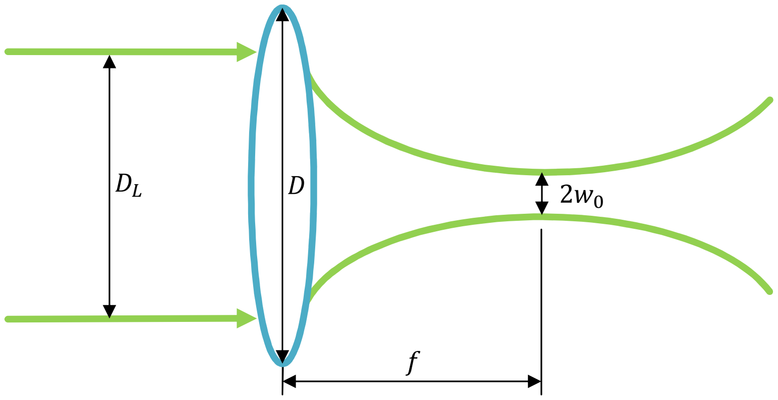

Figure 3.6: Gaussian beam waist

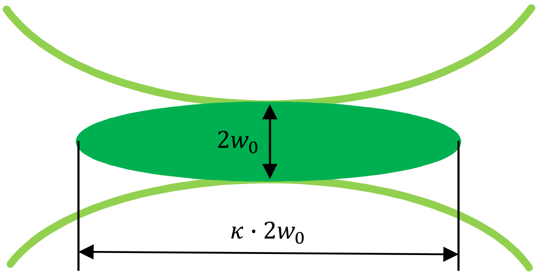

Figure 3.7: Confocal volume

A laser beam whose transverse magnetic and electric field amplitude profiles are given by a Gaussian function is called a Gaussian beam. The radial intensity distribution of such a beam is a Gaussian function as well. In reality, laser beams are not perfect Gaussian beams. A parameter M^2, related to the divergence of the beam, defines the laser beam quality. M^2 of the ideal Gaussian beam is 1. As the beam quality deteriorates, M^2 becomes larger. When laser light with a frequency ν_c and a beam quality M^2 passes through a lens, it is being focused as shown in Fig. 3.6. Here, f is the lens focal length and D_L is the $1/e^2$ diameter of the beam (diameter at which the beam intensity drops down to $1/e^2$ of the value given at the center of the beam). The focused beam radius at its waist w_0 is given by

$$w_0(\nu_c) = \frac{4c_L}{\pi\nu_c}\frac{f}{D_L}M^2 \tag{3.13}$$

where w_0 is again defined as the radius at which the intensity of the beam drops to $1/e^2$ of the value at the center, and c_L is the speed of light. Obviously, Fig. 3.6 is not drawn to scale, since the laser diameter is usually much smaller than the lens diameter and the beam only passes through a small part of the lens. The intensity of the laser beam is highest in the waist. So, scattered light should be collected from a region close to the beam waist. If it is collected by the same lens as used to focus the laser beam and along the same optical axis (scattering angle $\theta = 180°$, also known as backscattering mode), then by correctly placing a pinhole or aperture behind the lens, only in-focus light will be collected (Wolf, 2008). In this case, the out-of-focus light is eliminated. The confocal volume, V, depends on the lens properties and is given by:

$$V(\nu_c) = \pi^{\frac{3}{2}}\kappa w_0^3(\nu_c) \tag{3.14}$$

$$\kappa = \frac{2.33}{\sin\left[\arctan\left(\frac{D}{2f}\right)\right]} \tag{3.15}$$

where D is the lens diameter. The confocal volume has the shape of an oblate ellipsoid, with its longest principal axis oriented along the direction of beam propagation, as shown in Fig. 3.7. The ratio of the ellipsoid major axis to its minor axis is given by κ. Since the beam waist is a function of the laser frequency (wavelength), the confocal volume is also a function of the laser frequency. In total, the beam waist contains a $1 - 1/e^2$ fraction of the laser power. So, the average laser intensity in the actual beam waist is given by:

$$I_L(\nu_c) = \frac{P_L(1-\frac{1}{e^2})}{\pi w_0^2(\nu_c)} \tag{3.16}$$

It can be assumed that the intensity is constant throughout the ellipsoid. This is a valid assumption, since the laser intensity does not change significantly along the laser propagation direction if κ is high enough.

3.3. Frequency Scanning Method

With conventional detectors (CCD, PMT, PD, APD) and without the use of interferometers, all spectral information on the flow field's aero-thermal properties is lost due to on-chip integration. So, these detectors measure the light intensity and not its spectral distribution. A single detected intensity value is not sufficient to determine temperature, pressure, and the velocity component related to the Doppler shift of the flow. One way of resolving this issue is to use multiple incident laser frequencies, i.e. the frequency scanning method.

For the frequency scanning method of filtered Rayleigh scattering, the central scattering frequency of Rayleigh scattered light is scanned across the absorption feature (well) of a notch filter by varying the incident laser frequency. As already mentioned before, the central scattering frequency is related to the incident laser frequency by the net Doppler shift $\Delta\nu_D$, which depends on the flow velocity along $(\hat{O}-\hat{L})$. The scattered light signal that reaches the detector is collected during the scan. As the frequency is scanned, the position of the Rayleigh-Brillouin scattering profile within the filter absorption well changes, and so does the amount of the transmitted Rayleigh scattered light power through the filter. So, the detected Rayleigh scattered signal depends on the laser frequency. This process is schematically explained in Fig. 3.8.

The obtained curves (detected light signal vs. scanning frequency) are functions of the flow parameters and can be used to determine temperature, pressure, and velocity component along $(\hat{O}-\hat{L})$. In order to effectively block Mie scattering, the central scattering frequency must always be kept within the high absorption region (transmission less than 10^{-5}) of the filter. To stop geometrically scattered light and laser reflections from reaching the detector, the incident laser frequency must also always lie within the filter absorption well. It is important to note that the temporal resolution of the FSM-FRS method is limited by the time required to make a complete scan and obtain the curve. It is also limited by the time required to average out flow parameter fluctuations.

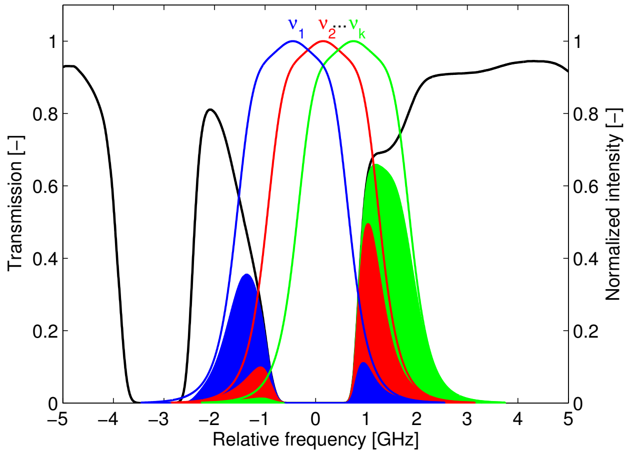

Figure 3.8: Frequency scanning method (Doll et al., 2014)

Forkey (1996) listed five desired notch filter criteria for the FSM-FRS: high transmission outside of the absorption feature, low transmission within the absorption well, a sharp cutoff edge between minimum and maximum transmission within much less than 1 GHz, a linewidth (frequency range over which the filter has a low transmission) of the absorption feature greater or equal to 1 GHz, and an easy variability of the absorption feature linewidth. The low transmission within the absorption notch ($< 10^{-5}$) is necessary to get rid of the Mie scattered photons and background reflections at the laser frequency. The large transmission outside of the absorption notch and sharp cutoff edges improves the detection of the Rayleigh-Brillouin scattering signal. The wide absorption linewidth is required to keep both the original laser frequency and the Doppler shifted central scattering frequency and have a wider range for frequency scanning. Easy variability of the filter absorption feature properties is advantageous for optimizing the scanning region for the specific flow cases and experiments. This can be done by varying the filter cell length and temperature.

The spectral width (linewidth) of the filter absorption features is in the range of several GHz. Therefore, for the FSM-FRS, the frequency of an incident laser is also scanned within this range. Such frequency change is too little to be noticed by the naked eye, but it can be measured using a wavelength meter that utilizes an array of interferometers to do so. There are other methods to measure the light frequency. For example, the laser frequency can be stabilized at an absorption maximum of a vapor filter, and changes in the transmitted light power can be related to the changes in the frequency if the filter transmission curve is known. However, this is not important at the moment. The frequency of a laser can be scanned by controlling piezoelectric actuators which squeeze or expand the laser resonator. The changes in the resonator length change the lasing frequency. With a proper control loop, specific frequencies can be selected with a high resolution. The temperature of an intra-cavity etalon can also be varied to adjust the frequency scanning range.

3.3.1. Direct-detection

Direct-detection is the simplest of the frequency scanning FRS methods. There are two approaches: discrete and continuous frequency scanning methods. In a discrete scanning method, as the name suggests, the frequency of a laser takes on discrete values. For each discrete laser frequency, Rayleigh scattered light is collected over some time, $\mathrm{d}t$. During the collection time, the frequency of the laser remains unchanged. This is visualized in Fig. 3.9a. Here, wavenumbers are used instead of the frequencies. The relative wavenumber is just given with respect to some initial value before starting the scan.

The plot visualizes a discrete frequency scan for a 1 Hz measurement rate. The number of discrete frequencies and the collection time per frequency depend on the temporal resolution of the measurement, the frequency scanning resolution (number of steps by which the laser frequency can be varied), and the usable filter absorption feature linewidth. The temporal resolution limits the time required for the complete frequency scan from one end of the absorption feature to the other. Depending on the net Doppler shift, the usable filter absorption feature linewidth can be different from the actual linewidth: for example, if there is a positive Doppler shift due to a flow velocity, the frequency of the scattered light will be higher than that of the incident light. So, in order to make sure that both the incident and the scattered light frequencies remain within the absorption well, the upper cutoff scanning frequency for the incident laser must be lower than the upper end of the filter absorption well by a margin $\Delta\nu_D$.

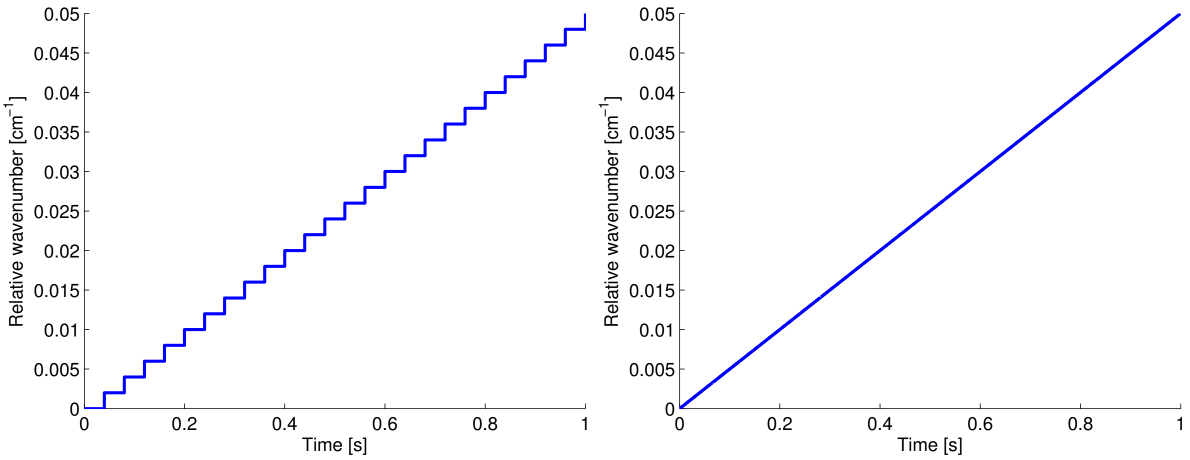

(a) Discrete frequency scanning (b) Continuous frequency scanning

Figure 3.9: Direct-detection frequency scanning

For each discrete laser frequency, a number of created photoelectrons within the detector can be calculated using Eq. 3.11. This results in a curve showing N_{PE} vs. the discrete laser frequency ν_c, as given by Eq. 3.17.

$$N_{PE}(\nu_c) = \epsilon\eta\frac{\Omega I_L(\nu_c)\mathrm{d}t}{h(\nu_c+\Delta\nu_D)}\frac{PV(\nu_c)}{k_B T}\frac{\partial\sigma}{\partial\Omega}(\nu_c)\int_{-\infty}^{+\infty}\tau(\nu)g\big(\theta,T,P,\nu-(\nu_c+\Delta\nu_D)\big)\mathrm{d}\nu \qquad (3.17)$$

This curve is solely a function of the temperature, pressure, and the flow velocity along $(\hat{O}-\hat{L})$, given that all other parameters are properly modelled and calculated. A least-squares fitting algorithm can be used to extract the flow parameters from this curve. Forkey (1996) and Doll et. al. (2012; 2014) both used a Levenberg-Marquardt least-square fitting algorithm for their 2D discrete frequency scanning FRS.

The discrete frequency scanning method is very attractive, but it has some limitations, such as the temporal resolution and the time required to switch between frequencies. For example, if the measurement rate is 1 Hz, the laser wavenumber resolution is 0.001 cm^{-1}, and the linewidth of the frequency scanning region is 1 GHz ($\approx$ 0.033 cm^{-1}), then there are 33 discrete frequencies to scan. For each frequency the scattered light must be collected for approximately 0.03 s. The frequency scanning region can be even wider. Scanning these frequencies wouldn't be a problem if the collection time was long enough. However, it is very hard to make discrete frequency steps and stabilize the laser frequency each time when $\mathrm{d}t$ is so small. Problem is the time required to switch from one discrete frequency to another. These jumps (switches) need to be done almost instantaneously, or at least the time required must be negligible compared to $\mathrm{d}t$. This is very hard to accomplish for the above-mentioned frequency scanning parameters. A possible solution is the continuous frequency scanning FRS.

In continuous FSM-FRS, instead of making discrete frequency steps, the frequency of an incident laser is scanned continuously from the starting value to the end. The total time for the scan remains unchanged, but the scattered light is collected throughout the whole scan duration. From a technical perspective, it could be easier to perform such a continuous scan. The continuous scanning process is depicted in Fig. 3.9b.

In order to obtain the signal equivalent to discrete FSM-FRS, which could be used for the least-squares fit, the detected signal must be integrated over the same collection time $\mathrm{d}t$ as used in discrete FSM-FRS. The modified expression for a number of induced photoelectrons within a detector is given by:

$$N_{PE}(\bar{\nu}_c) = \epsilon\eta \frac{\Omega I_L(\bar{\nu}_c)}{h(\bar{\nu}_c + \Delta\nu_D)} \frac{PV(\bar{\nu}_c)}{k_B T} \frac{\partial\sigma}{\partial\Omega}(\bar{\nu}) \int_{\Delta \mathrm{d}t} \int_{-\infty}^{+\infty} \tau(\nu) g\big(\theta, T, P, \nu - (\nu_c(t) + \Delta\nu_D)\big) \, \mathrm{d}\nu \mathrm{d}t \tag{3.18}$$

where $\bar{\nu}_c$ corresponds to the average incident laser frequency over the integration time, $\mathrm{d}t$. It is important to note that both the discrete and the continuous frequency scanning methods are conceptually equivalent if the collection and integration times match.

3.3.2. Frequency Modulation

Modulated frequency scanning FRS is a very attractive method as well. Even when a Rayleigh scattering measurement is confined to a point in space (as opposed to 2D planar measurements), high power laser sources are still required to produce a detectable signal. This is even more crucial in the presence of molecular filters. The modulated FSM-FRS technique utilizes modulated absorption spectroscopy techniques to improve the detectability of a weak Rayleigh scattered signal. It relies on lock-in amplifiers to detect a modulated FRS signal.

In modulated FSM-FRS, the laser frequency is dithered (modulated) at a rapid rate while simultaneously scanned (swept) across the filter absorption feature, as illustrated in Fig. 3.10. The Rayleigh scattered light carries the same modulation and so does the measured signal beyond the molecular filter. Homodyne (single frequency) detection of the transmitted signal is then accomplished by using a lock-in amplifier synchronized with the modulation frequency. The signal detected by a PMT or photodiode is fed to the lock-in amplifier. What the lock-in amplifier actually does is multiplying the detected signal with an internal reference signal which is synchronized with the modulation frequency. In the end, only the signal that is modulated at the dither frequency is detected. So, background and any other noise are completely rejected.

Jagodzinski (2007) provided the most in-depth model for modulated FRS. When modulating the incident laser frequency, the mean (central) scattering frequency can be expressed

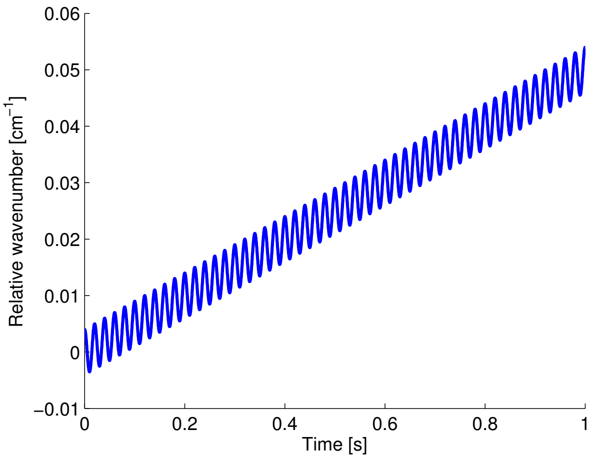

Figure 3.10: Modulated frequency scanning

as:

$$\nu(t) = \nu_c(t) + \Delta\nu_D + a\cos(2\pi\nu_m t) \tag{3.19}$$

where a is a modulation amplitude, ν_m is a modulation frequency, $\Delta\nu_D$ is the net Doppler shift, and ν_c is the incident laser frequency that is being scanned across the filter absorption feature. Assuming that the scattered light is monochromatic, the resulting time-varying absorption constant of the filter is given by:

$$\alpha(\nu(t)) = \alpha\big[\nu + a\cos(2\pi\nu_m t)\big] \tag{3.20}$$

$\alpha(\nu)$ equals $1-\tau(\nu)$ and already includes the effects of filter temperature and cell length. This function is periodic in 2π and can be expanded in a Fourier series if it is assumed that the mean scattering frequency is constant during one modulation period, $\nu(t) \approx \nu$. This is true if the modulation frequency is much higher than the rate at which the frequency is slowly swept. The expanded function is given by:

$$\alpha(\nu(t)) = \alpha(\nu, a, t) = \frac{H_0(\nu, a)}{2} + \sum_{n=1}^{\infty} H_n(\nu, a)\cos(2\pi n\nu_m a) \tag{3.21}$$

The Fourier coefficients, H_n, are calculated using:

$$H_n(\nu, a) = \frac{2}{\pi}\int_0^{\pi} \alpha(2\pi\nu + a\cos\varphi)\cos(n\varphi)\mathrm{d}\varphi \tag{3.22}$$

Scattered light passes through the filter before being detected. The homodyne detection of this signal is done using the lock-in amplifier. It mixes the detected signal with a reference sinusoidal signal oscillating at an integer multiple n of the modulated signal. This integer multiple corresponds to the Fourier component of the signal to be recorded. Since the Fourier series functions are expanded via an infinite series, the number of terms has to be truncated for practical purposes. Jagodzinski (2007) showed that in fact only the first 4-5 coefficients are relevant. Higher order terms are negligible. For moderate modulation amplitudes, the n^{th} harmonic lock-in signal is simply proportional to the n^{th} derivative of the filter absorption (transmission) signal. Basically, the lock-in amplifier detects the n^{th} derivative of the actual transmitted signal. The following expressions were utilized for the first and second harmonic ($1f$ and $2f$) lock-in filter transmission signals (equivalent to $\tau(\nu)$ from the direct-detection FSM-FRS):

$$\begin{aligned}
S_L{}'(\nu, a) = {} & -H_1 + \frac{1}{2}(H_0H_1 + H_1H_2 + H_2H_3 + H_3H_4) - \frac{1}{6}\Big(\frac{3}{4}H_0^2H_1 + \frac{3}{4}\Big[H_1^2(H_1 \\
& + H_3) + H_2^2(H_3 + H_5) + H_3^2(H_5 + H_7) + H_4^2(H_7 + H_9)\Big] + \frac{3}{2}H_1(H_2^2 + H_3^2 + H_4^2) \\
& + \frac{3}{2}H_0(H_1H_2 + H_2H_3 + H_3H_4 + H_4H_5) + \frac{3}{2}H_1(H_2H_4 + H_3H_5) + \frac{3}{2}H_2\Big[H_3(H_4 \\
& + H_6) + H_4(H_5 + H_7)\Big] + \frac{3}{2}H_3H_4(H_6 + H_8) + \frac{3}{2}H_4H_5(H_8 + H_{10})\Big)
\end{aligned} \tag{3.23}$$

$$\begin{aligned} S_L''(\nu,a) = {} & -H_2 + \frac{1}{2}\Big[\frac{H_1^2}{2}(H_0H_2 + H_1H_3 + H_2H_4 + H_3H_5)\Big] - \frac{1}{6}\Big(\frac{3}{4}H_0^2H_2^2 + \\ & \frac{3}{4}\Big[H_1^2(H_0+H_4) + H_2^2(H_2+H_6) + H_3^2(H_4+H_8) + H_4^2(H_6+H_{10})\Big] + \\ & \frac{3}{2}H_2(H_1^2 + H_3^2 + H_4^2 + H_5^2) + \frac{3}{2}H_0(H_1H_3 + H_2H_4 + H_3H_5) + \frac{3}{2}H_1\Big[H_2(H_3 + \\ & H_5) + H_3(H_4+H_6) + H_4(H_5+H_7) + H_5(H_6+H_8)\Big] + \frac{3}{2}H_2(H_3H_7 + H_4H_8 \\ & + H_5H_9) + \frac{3}{2}H_3\Big[H_4(H_5+H_9) + H_5(H_6+H_{10})\Big] + \frac{3}{2}H_4H_5(H_7+H_{11})\Big) \end{aligned} \tag{3.24}$$

The Fourier components H_n are all functions of the frequency ν and the modulation amplitude a. The expressions are independent of the modulation frequency given the fact that it is high enough to ensure that the mean (central) scattering frequency during one modulation period remains nearly constant. In a real experiment, the actual detected signal is given in different units and multiplied by constant conversion factors. That is because the lock-in amplifier and the photodiode produce current or voltage signals. However, scaling these signals is not an issue since the conversion factors are given and specified for the electronic devices.

The formulae of the 1st and 2nd harmonics of the transmission were derived under the assumption of monochromatic scattered light. They need to be convoluted with Rayleigh-Brillouin scattering profiles. So, the obtained expressions for the harmonics of the filter transmission function can be used to derive the formulae for the detected signal of modulated FSM-FRS which are proportional to the 1st and 2nd derivatives ($1f$ and $2f$) of the continuous FSM-FRS signal.

$$\begin{aligned} N_{PE}'(\bar{\nu}_c) = \epsilon\eta \frac{\Omega I_L(\bar{\nu}_c)}{h(\bar{\nu}_c + \Delta\nu_D)} \frac{PV(\bar{\nu}_c)}{k_BT} \frac{\partial\sigma}{\partial\Omega}(\bar{\nu}) \int_{\Delta \mathrm{d}t} \int_{-\infty}^{+\infty} & S_L'(\nu,a) \\ & g\big(\theta,T,P,\nu - (\nu_c(t) + \Delta\nu_D)\big)\mathrm{d}\nu\mathrm{d}t \end{aligned} \tag{3.25}$$

$$\begin{aligned} N_{PE}''(\bar{\nu}_c) = \epsilon\eta \frac{\Omega I_L(\bar{\nu}_c)}{h(\bar{\nu}_c + \Delta\nu_D)} \frac{PV(\bar{\nu}_c)}{k_BT} \frac{\partial\sigma}{\partial\Omega}(\bar{\nu}_c) \int_{\Delta \mathrm{d}t} \int_{-\infty}^{+\infty} & S_L''(\nu,a) \\ & g\big(\theta,T,P,\nu - (\nu_c(t) + \Delta\nu_D)\big)\mathrm{d}\nu\mathrm{d}t \end{aligned} \tag{3.26}$$

It is also possible to feed the detector signal to two lock-in amplifiers, synchronized at different frequencies. This allows the detection of both the 1st and the 2nd harmonics. If they are divided by each other ($1f/2f$), the signal becomes independent of the scattered light power. The result is a frequency dependent but scattering intensity independent ratios $N_{PE}{}^{R}(\bar{\nu}_c)$:

$$N_{PE}{}^{R}(\bar{\nu}_c) = \frac{\int_{\Delta \mathrm{d}t}\int_{-\infty}^{+\infty} S_L'(\nu,a) g(\theta,T,P,\nu - (\nu_c(t)+\Delta\nu_D))\mathrm{d}\nu\mathrm{d}t}{\int_{\Delta \mathrm{d}t}\int_{-\infty}^{+\infty} S_L''(\nu,a) g(\theta,T,P,\nu - (\nu_c(t)+\Delta\nu_D))\mathrm{d}\nu\mathrm{d}t} \tag{3.27}$$

This expression is also independent of the optical and quantum efficiencies.

3.3.3. State of the Art

A direct-detection frequency scanning FRS technique has been developed by Forkey (1996) and Doll et. al. (2014). They both built an experimental setup for performing 2D simultaneous measurements of pressure, temperature, and a single velocity component of the flow. A Levenberg-Marquardt least-squares algorithm has been used for fitting the flow parameters to a FSM-FRS spectrum. However, they have not created a single tool for predicting the parameter accuracies and optimizing different setups beforehand.

Modulated frequency scanning FRS has been developed by Mach and Varghese (1999), and Jagodzinski (2007) only for the purpose of measuring the flow velocity. This technique could operate in frequency-scanning or frequency-locked mode. In frequency scanning modulated FRS, an incident laser was split into two beams. One beam was focused at a point of interest in a medium with a nonzero flow velocity and another one in a stationary medium. The frequency of the incident laser was scanned across the absorption feature of a filter while simultaneously modulating it at a rapid rate. The detected Rayleigh scattered signals from both interrogation volumes ($1f$, $2f$, or $1f/2f$) were functions of the scanning frequency (or time). Cross-correlating these signals gave an estimate about the Doppler shift and the corresponding velocity component of a flow. Needless to say, the thermodynamic state of both the stationary and non-stationary mediums must be the same.

In frequency-locked mode, the entire beam was focused to the point of interest in a flow. In a calibration sweep with a stationary flow, the modulated frequency of the incident laser was swept across the filter absorption well and the magnitude of $1f$, $2f$, or $1f/2f$ signals was recorded as a function of the frequency. Afterwards, the frequency of the laser was fixed to an arbitrary value. Now for the actual measurement of an unknown flow velocity again the amplitudes of the $1f$, $2f$, or $1f/2f$ signals were recorded. By finding the laser frequency corresponding to the measured amplitude in the calibration curve and subtracting the fixed laser frequency from it, the Doppler shift (and thus the specific velocity component) could be determined. Again, the thermodynamic parameters of the flow must be same as they were during the calibration. Also, a sufficient dynamic range of frequencies must be covered during the calibration sweep. The frequency-locked mode offers higher measurement rates (temporal resolution) than the frequency scanning method, since there is no need to scan the frequencies. However, it can not be used to determine pressure and temperature of a flow.

Grinstead et al. (1998) also developed a frequency-locked modulated FRS velocimeter. However, their approach was radically different: contrary to the other methods, the frequency of the scattered light was fixed and locked to an absorption maximum of a notch filter by controlling the incident laser frequency. This was achieved by monitoring a frequency-modulated absorption signal and using it as a feedback. At the absorption resonance of a filter, intensity of the transmitted light is minimal. So, the filter absorption curve has a local minimum at that frequency. Therefore, the first derivative of the absorption signal must be zero. Grinstead et al. (1998) used $1f$ homodyne detection based on a lock-in amplifier. They controlled the incident laser frequency in order to null the frequency-modulated $1f$ signal (keep close to 0, i.e. locked). Independent of the Doppler shift due to a flow velocity, the frequency of the scattered light was always the same. However, the frequency of the incident laser, when the scattered light was frequency locked, varied depending on the Doppler shift and could be measured as an output of the loop control electronics. The difference to the filter resonance frequency and the incident laser frequency was the effective Doppler shift from which the flow velocity component could be determined. The advantage of this approach over Jagodzinski's frequency-locked method is that there is no need for the calibration sweep. Also, higher temporal resolutions can be achieved. However, it requires implementing rather complex feedback loop.

Obviously, a direct-detection FSM-FRS can be used for measuring all three flow parameters in the laser focus. In principle, a modulated frequency scanning FRS can also do that given the adequate post-processing by fitting all parameters instead of focusing only on the velocity. However, a frequency-locked modulated FRS technique can not be used for that because it only provides a single output value: the scattered signal amplitude or the frequency drift from an absorption resonance of a filter. It is very interesting to see how the modulated and direct-detection FSM-FRS methods compare and how they can be further improved.

4

End-to-End Simulator

4.1. Overview

The main purpose of the end-to-end simulator is to investigate and analyze different FSM-FRS approaches. It brings together several FSM-FRS techniques available in literature and complements them with new approaches that have never been used before. The e2e simulator is going to be a very useful tool for FRS system design. It can be used to simulate or mimic FSM-FRS experiments and know the expected accuracies in advance. The simulator can also be utilized for optimizing FSM-FRS experiments for specific flow conditions. It is also possible to use it in a preliminary stage of FSM-FRS probe design. Using an uncertainty quantification, the end-to-end simulator calculates the expected accuracies in pressure, temperature, and velocity of the flow for a proposed FSM-FRS configurations. This output can be used for the optimization of experimental arrangements and components. Required inputs include the parameters of the laser system, the optical layout and the details about the flow case to be simulated. The input and output of the simulator is explained in detail in section 4.5.

In this thesis, the design of an in-flight FRS probe is presented as an application of the e2e simulator. The idea behind the project OSIRIS is to show the potential of FRS probes for in-flight application and to optimize different setups. Since the project sets technical requirements for FRS to be applicable to in-flight use, some input parameters are fixed or can be varied only within a limited range. More on this topic is given in the next sections as well.

4.2. Uncertainty Quantification

Uncertainty quantification (UQ) is one of the most important features of the end-to-end simulator. It is crucial for investigating different FSM-FRS methods and optimizing them. For a given FRS measurement method and setup, the uncertainty quantification provides an estimate of the expected accuracy. The UQ of the e2e simulator consists of two parts: systematic and statistical uncertainties. In this case, the systematic uncertainties arise from model assumptions and simplifications (modelling errors). For a given experimental setup and optics, the systematic uncertainties are more or less independent of the FSM-FRS technique and most other parameters that can be varied, such as the filter temperature. The statistical uncertainties, on the other hand, arise from random uncertainties in parameters and strongly depend on the choice of the FSM-FRS method and other parameters. For the cases considered in this thesis, the systematic uncertainties are insignificant compared to the statistical uncertainties. So, for optimizing the FSM-FRS methods, the statistical analysis is used.

For the statistical analysis the required computational time is considerable. Therefore, it is advantageous to simplify the equations as much as possible without significantly increasing modelling errors and thus sacrificing the accuracy of the simulation. In all studies performed using the e2e simulator, the Levenberg–Marquardt least-squares fitting algorithm is utilized for determining the flow parameters from the FSM-FRS spectra. This algorithm minimizes the least-squares error between the fitted curve and the simulated (or measured) spectrum by fitting pressure, temperature, and Doppler velocity of the flow based on the equations discussed in the previous sections. The Doppler velocity, $u_D = \vec{v} \cdot (\hat{O} - \hat{L}) / \lambda$, is the only sensitive component of the velocity vector that has an effect on the FSM-FRS spectra.

4.2.1. Systematic Uncertainties

The systematic uncertainties are incurred due to the model assumptions and simplifications when using Eq. 3.17, 3.18, 3.25, 3.26, and 3.27. In contrast to statistical uncertainties, they can be avoided if no assumptions are used. Most of the time, they are negligible compared to the statistical errors. After putting in all the required parameters for a given FSM-FRS setup to be investigated, the e2e simulator calculates the systematic uncertainties in the flow parameters incurred by the model assumptions. They need to be estimated to assure the validity of the assumptions.

Laser Lineshape

One of the advantages of the laser for the spectroscopic studies is that it produces a monochromatic (i.e. uniform wavelength) light beam. In reality however, no laser is perfectly monochromatic. So, the laser light is spectrally broadened. The normalized lineshape of the spectral profile $l(\nu - \nu_c)$ can often be described by Gaussian and/or Lorentzian functions. The extent of broadening is given by the full width at half maximum (FWHM) of the laser lineshape function. The FWHM is often provided by laser manufacturers and is directly related to the standard deviation of the distribution function σ_l by the following expression:

$$\mathrm{FWHM} = 2\sqrt{2 \ln 2}\,\sigma_l \tag{4.1}$$

In general, continuous-wave lasers have a much narrower spectral profiles than pulsed lasers. In the context of project OSIRIS, lasers with a lineshape function FWHM < 5 MHz are considered. This is also the specified spectral broadening of a Coherent Verdi V5 laser that is used both in the simulations and the validation experiment.

Important assumption of the e2e simulator is that the incident laser light is monochromatic and has no broadening. Compared to the Rayleigh-Brillouin scattering profile (~GHz), a width of the laser lineshape is negligible (~MHz), and the result of the convolution of these functions is identical to the original Rayleigh-Brillouin profile. This assumption saves computational time. However, it could incur some systematic deviation. To assess the effect of the assumption for a given experimental case and set of flow parameters (temperature, pressure, and Doppler velocity), the FSM-FRS spectrum is computed without the laser lineshape simplification from Eq. 4.2-4.6, depending on the method that is being investigated.

$$N_{PE}(\nu_c) = \epsilon\eta \frac{\Omega I_L(\nu_c)\mathrm{d}t}{h(\nu_c+\Delta\nu_D)} \frac{PV(\nu_c)}{k_B T} \frac{\partial\sigma}{\partial\Omega}(\nu_c) \int_{-\infty}^{+\infty} \tau(\nu) \int_{-\infty}^{+\infty} l(\nu-(\nu_c+\Delta\nu_D)-\nu') g(\theta,T,P,\nu')\mathrm{d}\nu'\mathrm{d}\nu \tag{4.2}$$

$$N_{PE}(\bar{\nu}_c) = \epsilon\eta \frac{\Omega I_L(\bar{\nu}_c)}{h(\bar{\nu_c}+\Delta\nu_D)} \frac{PV(\bar{\nu}_c)}{k_B T} \frac{\partial\sigma}{\partial\Omega}(\bar{\nu}_c) \int_{\Delta\mathrm{d}t} \int_{-\infty}^{+\infty} \tau(\nu) \int_{-\infty}^{+\infty} l(\nu-(\nu_c(t)+\Delta\nu_D)-\nu') g(\theta,T,P,\nu')\mathrm{d}\nu'\mathrm{d}\nu\mathrm{d}t \tag{4.3}$$

$$N_{PE}{}'(\bar{\nu}_c) = \epsilon\eta \frac{\Omega I_L(\bar{\nu}_c)}{h(\bar{\nu_c}+\Delta\nu_D)} \frac{PV(\bar{\nu}_c)}{k_B T} \frac{\partial\sigma}{\partial\Omega}(\bar{\nu}_c) \int_{\Delta\mathrm{d}t} \int_{-\infty}^{+\infty} S_L{}'(\nu,a) \int_{-\infty}^{+\infty} l(\nu-(\nu_c(t)+\Delta\nu_D)-\nu') g(\theta,T,P,\nu')\mathrm{d}\nu'\mathrm{d}\nu\mathrm{d}t \tag{4.4}$$

$$N_{PE}{}''(\bar{\nu}_c) = \epsilon\eta \frac{\Omega I_L(\bar{\nu}_c)}{h(\bar{\nu_c}+\Delta\nu_D)} \frac{PV(\bar{\nu}_c)}{k_B T} \frac{\partial\sigma}{\partial\Omega}(\bar{\nu}_c) \int_{\Delta\mathrm{d}t} \int_{-\infty}^{+\infty} S_L{}''(\nu,a) \int_{-\infty}^{+\infty} l(\nu-(\nu_c(t)+\Delta\nu_D)-\nu') g(\theta,T,P,\nu')\mathrm{d}\nu'\mathrm{d}\nu\mathrm{d}t \tag{4.5}$$

$$N_{PE}{}^R(\bar{\nu}_c) = \frac{\int_{\Delta\mathrm{d}t}\int_{-\infty}^{+\infty} S_L{}' \int_{-\infty}^{+\infty} l(\nu-(\nu_c(t)+\Delta\nu_D)-\nu') g(\theta,T,P,\nu')\mathrm{d}\nu'\mathrm{d}\nu\mathrm{d}t}{\int_{\Delta\mathrm{d}t}\int_{-\infty}^{+\infty} S_L{}'' \int_{-\infty}^{+\infty} l(\nu-(\nu_c(t)+\Delta\nu_D)-\nu') g(\theta,T,P,\nu')\mathrm{d}\nu'\mathrm{d}\nu\mathrm{d}t} \tag{4.6}$$

Afterwards, the simplified equations (Eq. 3.17, 3.18, 3.25, 3.26, or 3.27) are used to fit pressure, temperature, and a Doppler velocity to the obtained spectrum. The differences in the original and the fitted parameters give the estimate about a systematic deviation in temperature, pressure, and Doppler velocity due to neglecting the spectral broadening of the laser light. For lasers with linewidth less than 5 MHz, as intended for OSIRIS, the systematic deviations in pressure, temperature, and velocity components caused by neglecting the laser linewidth are less than 1 Pa, 0.01 K, and 0.01 m/s (rounding accuracies of simulations, see chapter 5), respectively. So, the incurred systematic uncertainties are negligible.

Small Lens Angle

Before scattered light is collected, parallelized and directed towards the molecular filter, it must be collected by a lens. Since the light collection angle is nonzero, the observation direction varies within the lens, as shown in Fig. 4.1. As one can see, $\hat{O}$ is different for each light ray that is collected by the lens. Technically, there is only one collected light ray that is parallel to the optical axis of the lens. Due to this, parameters such as the net Doppler shift, scattering cross section, scattering angle, and a Rayleigh-Brillouin profile differ as well - basically everything that has a directional dependency is not constant over the lens. The degree of variation depends on the lens solid angle Ω, which is defined as the ratio of the lens surface area S, to the square of the focal length f:

$$\Omega = \frac{S}{f^2} = 2\pi\left[1-\cos\left(2\cdot\tan^{-1}\left(\frac{1}{2f_\#}\right)\right)\right] \tag{4.7}$$

where D is the lens diameter, and $f_\#$ is the f-number of the lens, defined as $f_\# = f/D$. The lens solid angle is only a function of $f_\#$ and is inversely related to it. So, as the lens f-number increases, Ω decreases and the parameters within the lens vary less. If $f_\#$ is large enough,

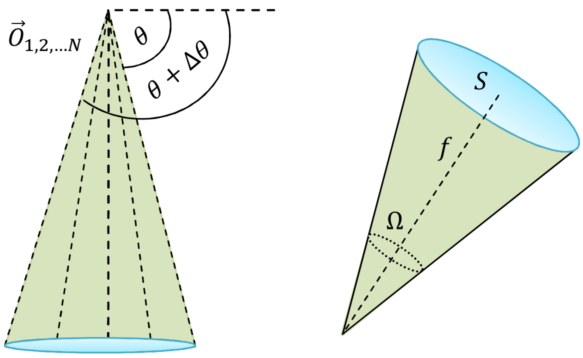

Figure 4.1: Lens solid angle

then Ω is negligible and it can be assumed that the observation direction and thus the other properties do not change within the whole lens. In such a case, the parameters that have a directional dependency can be calculated in the center of the lens (along the optical axis) and assumed to be constant over the lens. This is a very important model simplification that significantly decreases the complexity and the computational time. However, the validity of this assumption strongly depends on the collection optics and could generate a considerable systematic effect. To calculate the extent of the deviation, integration must be performed over the lens solid angle. This can not be done analytically. However, a finite element approach can be used.

A finite element analysis of the lens is visualized in Fig. 4.2. The collection lens is divided into a number of radial and annular sections, N_i and N_j. For each section (i, j) the solid angle is given by $\Delta\Omega_{i,j}$ with $\Omega = \sum_{i=1}^{N_i}\sum_{j=1}^{N_j}\Delta\Omega_{i,j}$. For each section (i, j) the observation direction and all other parameters are evaluated in its center (denoted by dots in Fig. 4.2) and assumed to be constant within the section. As the number of sections increases, $\Delta\Omega_{i,j}$ decreases and the integration becomes more and more accurate. So, if the assumption of a small Ω is removed, then the equations for calculating the FSM-FRS spectra are as follows:

$$N_{PE}(\nu_c) = \sum_{j=1}^{N_j}\sum_{i=1}^{N_i}\epsilon\eta\frac{\Delta\Omega_{i,j} I_L(\nu_c)\mathrm{d}t}{h(\nu_c+\Delta\nu_D)}\frac{PV(\nu_c)}{k_B T}\frac{\partial\sigma}{\partial\Omega_{i,j}}(\nu_c)\int_{-\infty}^{+\infty}\tau(\nu)\, g\big(\theta_{i,j}, T, P, \nu-(\nu_c+\Delta\nu_{D\,i,j})\big)\mathrm{d}\nu \tag{4.8}$$

$$N_{PE}(\bar{\nu}_c) = \sum_{j=1}^{N_j}\sum_{i=1}^{N_i}\epsilon\eta\frac{\Delta\Omega_{i,j} I_L(\bar{\nu}_c)}{h(\bar{\nu}_c+\Delta\nu_D)}\frac{PV(\bar{\nu}_c)}{k_B T}\frac{\partial\sigma}{\partial\Omega_{i,j}}(\bar{\nu}_c)\int_{\Delta\mathrm{d}t}\int_{-\infty}^{+\infty}\tau(\nu)\, g\big(\theta_{i,j}, T, P, \nu-(\nu_c(t)+\Delta\nu_{D\,i,j})\big)\mathrm{d}\nu\mathrm{d}t \tag{4.9}$$

$$N_{PE}{}'(\bar{\nu}_c) = \sum_{j=1}^{N_j}\sum_{i=1}^{N_i}\epsilon\eta\frac{\Delta\Omega_{i,j} I_L(\bar{\nu}_c)}{h(\bar{\nu}_c+\Delta\nu_D)}\frac{PV(\bar{\nu}_c)}{k_B T}\frac{\partial\sigma}{\partial\Omega_{i,j}}(\bar{\nu}_c)\int_{\Delta\mathrm{d}t}\int_{-\infty}^{+\infty}S_L{}'(\nu, a)\, g\big(\theta_{i,j}, T, P, \nu-(\nu_c(t)+\Delta\nu_{D\,i,j})\big)\mathrm{d}\nu\mathrm{d}t \tag{4.10}$$

$$N_{PE}{}''(\bar{\nu}_c) = \sum_{j=1}^{N_j}\sum_{i=1}^{N_i}\epsilon\eta\frac{\Delta\Omega_{i,j} I_L(\bar{\nu}_c)}{h(\bar{\nu}_c+\Delta\nu_D)}\frac{PV(\bar{\nu}_c)}{k_B T}\frac{\partial\sigma}{\partial\Omega_{i,j}}(\bar{\nu}_c)\int_{\Delta\mathrm{d}t}\int_{-\infty}^{+\infty}S_L{}''(\nu, a)\, g\big(\theta_{i,j}, T, P, \nu-(\nu_c(t)+\Delta\nu_{D\,i,j})\big)\mathrm{d}\nu\mathrm{d}t \tag{4.11}$$

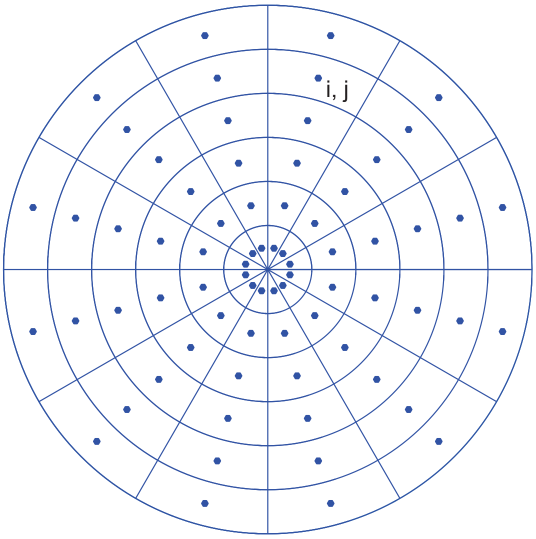

Figure 4.2: Discrete lens sections

$$
{N_{PE}}^{R}(\bar{\nu}_c) = \frac{{N_{PE}}'(\bar{\nu}_c)}{{N_{PE}}''(\bar{\nu}_c)} \tag{4.12}
$$

The number of required sections can be estimated by looking at the convergence in the calculated FSM-FRS spectrum for a given case and method. The number of sections was increased until the change in FSM-FRS spectrum was negligible. It was found that $N_i = 6$ and $N_j = 12$, which corresponded to 72 sections, were already sufficient.

Even though a finite element approach is very attractive and realistic, it requires a lot of computational power. It is not realistic to do the statistical uncertainty quantification with this model. Therefore, the simplified formulae are used for this purpose. To prove the validity of this simplification the systematic deviation caused by it is calculated in a similar way as for the other systematic uncertainties: for a given case and a set of flow parameters, the FSM-FRS spectrum is computed using Eq. 4.8-4.12. Afterwards, the simplified equations are used to fit pressure, temperature, and Doppler velocity to the spectrum. The difference between the original and the fitted parameters provides a measure of the systematic uncertainty incurred due to the small Ω assumption. As a result it was conceived that the small lens angle assumption may sometimes produce a considerable error, and as the simulations will show in chapter 5, it is the only assumption that has to be kept in mind. Forkey (1996) and Doll (2016) showed that usually a collection lens with $f_{\#} = 10$ is sufficient for $< 0.1\%$ accuracy in the flow parameters.

Particle Scattering

The two assumptions mentioned before are more general and not associated with any specific flow case. However, in the project OSIRIS, which is the first application of the e2e simulator, it is given that there are 10000 aerosol particles per cubic centimeter at cruise altitude. These particles are formed by the aggregation of volcanic ash and water droplets. They can be assumed to have a spherical shape and a diameter of 10 nm. Also, their refractive index and density are similar to that of a water. These particles also scatter light along with the air molecules. Since the diameter of the ash particles is much less than the incident light wavelength, $d < 0.1\lambda$, the scattering process is dominated by Rayleigh scattering.

Even though the Tenti S6 model is usually a good numerical model for determining Rayleigh scattering profiles, it cannot be used on arbitrary particle or molecules. Since it is only valid and defined for diatomic molecules. For a rough estimate of the effect of these particles, a simple Doppler broadening formula can be used to determine the scattered light lineshape (HyperPhysics, 2016). The Doppler broadening is effectively thermal broadening and has a Gaussian shape which can be described by a standard deviation, given by:

$$\sigma_f = \sqrt{\frac{k_B T \ln 2}{m {c_L}^2}} (\nu_c + \Delta\nu_D) \tag{4.13}$$

$$m = \rho V_p = \frac{\pi \rho d^3}{6} \tag{4.14}$$

where m is the mass of the particle and V_p is its volume. The Gaussian scattering profile $g_{ash}(T,\nu)$ is centered around a mean (central) scattering frequency and can be calculated by knowing ν_c, $\Delta\nu_D$, and T. In fact, a Tenti S6 Rayleigh-Brillouin scattering profile approaches the thermally broadened lineshape for $Y \ll 1$. It must be noted that the differential scattering cross section is also different for such spherical particles and can be calculated as follows (Miles et al., 2001):

$$\frac{\partial\sigma_{ash}}{\partial\Omega}(\phi) = \frac{9\pi^2 V^2}{\lambda^4}\left(\frac{n^2-1}{n^2+2}\right)^2 \sin\phi^2 \tag{4.15}$$

where ϕ is the angle between the laser polarization vector and the observation direction. Since the refractive index n of ash particles is similar to that of a water, they can be calculated as a function of the temperature and the laser wavelength (Bashkatov & Genina, 2003):

$$n(\lambda, T) = A_T(T) + \frac{B_T(T)}{\lambda^2} + \frac{C_T(T)}{\lambda^4} + \frac{D_T(T)}{\lambda^6} \tag{4.16}$$

where the coefficients $A_T(T)$, $B_T(T)$, $C_T(T)$, $D_T(T)$ are the functions of temperature and can be looked up in the reference. At cruise altitude, the total number of induced photoelectrons for the direct-detection discrete and continuous FSM-FRS can be calculated using:

$$\begin{aligned} N_{PE_T}(\nu_c) = N_{PE}(\nu_c) + \epsilon\eta \frac{10^{10}\Omega V(\nu_c) I_L(\nu_c) \mathrm{d}t}{h(\nu_c + \Delta\nu_D)} \frac{\partial\sigma_{ash}}{\partial\Omega}(\nu_c) \int_{-\infty}^{+\infty} \tau(\nu) \\ g_{ash}\big(T, \nu - (\nu_c(t) + \Delta\nu_D)\big)\mathrm{d}\nu \end{aligned} \tag{4.17}$$

$$\begin{aligned} N_{PE_T}(\bar{\nu}_c) = N_{PE}(\bar{\nu}_c) + \epsilon\eta \frac{10^{10}\Omega V(\bar{\nu}_c) I_L(\bar{\nu}_c)}{h(\bar{\nu_c} + \Delta\nu_D)} \frac{\partial\sigma_{ash}}{\partial\Omega}(\bar{\nu}_c) \int_{\Delta \mathrm{d}t}\int_{-\infty}^{+\infty} \tau(\nu) \\ g_{ash}\big(T, \nu - (\nu_c(t) + \Delta\nu_D)\big)\mathrm{d}\nu\mathrm{d}t \end{aligned} \tag{4.18}$$

where $N_{PE}(\nu_c)$ and $N_{PE}(\bar{\nu}_c)$ come from the Eq. 3.17 and 3.18. Regarding a modulated FSM-FRS, things are slightly different here: since the derivatives of the signals cannot be added like the total number of photoelectrons, formulae have to be adjusted.

$$\begin{aligned} N_{PE}{}'_T(\bar{\nu}_c) = \epsilon\eta \frac{\Omega V(\bar{\nu}_c) I_L(\bar{\nu}_c)}{h(\bar{\nu_c} + \Delta\nu_D)} \int_{\Delta \mathrm{d}t}\int_{-\infty}^{+\infty} {S_L}'(\nu, a)\Big[\frac{\partial\sigma_{ash}}{\partial\Omega}(\bar{\nu}_c) 10^{10} g_{ash}\big(T, \nu - (\nu_c(t) \\ + \Delta\nu_D)\big) + \frac{\partial\sigma}{\partial\Omega}(\bar{\nu}_c)\frac{P}{k_B T} g\big(\theta, T, P, \nu - (\nu_c(t) + \Delta\nu_D)\big)\Big]\mathrm{d}\nu\mathrm{d}t \end{aligned} \tag{4.19}$$

$$
\begin{aligned}
N_{PE}{}''_{T}(\bar{\nu}_c) = \epsilon\eta \frac{\Omega V(\bar{\nu}_c) I_L(\bar{\nu}_c)}{h(\bar{\nu}_c + \Delta\nu_D)} \int_{\Delta \mathrm{d}t} \int_{-\infty}^{+\infty} S_L{}''(\nu, a) \Big[\frac{\partial\sigma_{ash}}{\partial\Omega}(\bar{\nu}_c) 10^{10} g_{ash}\big(T, \nu - (\nu_c(t) \\
+\Delta\nu_D)\big) + \frac{\partial\sigma}{\partial\Omega}(\bar{\nu}_c) \frac{P}{k_B T} g\big(\theta, T, P, \nu - (\nu_c(t) + \Delta\nu_D)\big) \Big] \mathrm{d}\nu \mathrm{d}t
\end{aligned}
\tag{4.20}
$$

$$
N_{PE}{}^{R}_{T}(\bar{\nu}_c) = \frac{\int_{\Delta \mathrm{d}t} \int_{-\infty}^{+\infty} S_L{}'(\nu, a) \Big[\frac{\partial\sigma_{ash}}{\partial\Omega}(\bar{\nu}_c) g_{ash}(T, \nu - (\nu_c(t) + \Delta\nu_D))}{\begin{array}{r} \int_{\Delta \mathrm{d}t} \int_{-\infty}^{+\infty} S_L{}''(\nu, a) \Big[\frac{\partial\sigma_{ash}}{\partial\Omega}(\bar{\nu}_c) g_{ash}(T, \nu - (\nu_c(t) + \Delta\nu_D)) \\ \dfrac{+\frac{\partial\sigma}{\partial\Omega}(\bar{\nu}_c) \frac{P}{k_B T} g(\theta, T, P, \nu - (\nu_c(t) + \Delta\nu_D)) \Big] \mathrm{d}\nu \mathrm{d}t}{+\frac{\partial\sigma}{\partial\Omega}(\bar{\nu}_c) \frac{P}{k_B T} g(\theta, T, P, \nu - (\nu_c(t) + \Delta\nu_D)) \Big] \mathrm{d}\nu \mathrm{d}t} \end{array}}
\tag{4.21}
$$

With the formulae above, the FSM-FRS spectra can be calculated taking into account the additional scattering particles at cruise altitude. In the statistical analysis, the effect of these particles is neglected. The systematic deviation caused by this model simplification is calculated in a same way as in the other cases: for a given set of flow parameters, the FSM-FRS spectrum is computed using Eq. 4.17-4.21. Afterwards, the simplified equations are used to fit pressure, temperature, and Doppler velocity to the spectrum. Again, the difference between the original and the fitted parameters provides a measure of the systematic uncertainty incurred by neglecting the ash particle scattering.

It is important to mention that the spectral profile of a scattered light from the ash particles, $g_{ash}\big(T, \nu - (\nu_c(t) + \Delta\nu_D)\big)$, is not an exact profile because the effects of pressure and scattering angle have been neglected. This is only to give a rough estimate of the deviation and whether it is negligible, not precise numbers. Presence of 10000 aerosol particles per cubic centimeter of air at cruise conditions causes the systematic deviations in pressure, temperature, and velocity components which are less than 1 Pa, 0.01 K, and 0.01 m/s, respectively. So, this source of systematic uncertainty is negligible as well.

4.2.2. Statistical Uncertainties

The random or statistical uncertainty of a measured quantity is directly related to uncertainties associated with a certain number of input quantities through an appropriate mathematical model. The random uncertainties in the presented experimental measurements are caused by stochastic and random changes in the experiment. These changes occur in the measuring instruments. The associated random uncertainties often have a Gaussian normal distribution. In such case, statistical methods can be used to analyze the data. It is important to understand that as long as the input quantities of the measurement model are uncertain, the output quantities are uncertain to some extent as well. This can not be avoided or corrected. However, the experimental setups can be optimized to reduce the sensitivity to random noise in the dependent parameters.

An FSM-FRS experiment also suffers from uncertainties in the input quantities. The whole idea behind the e2e simulator is to assess and minimize the resulting random uncertainty in temperature, pressure, and velocity for a given FRS setup. At first, the input quantities and the corresponding uncertainty ranges are defined based on the FSM-FRS setup. Then they are propagated through the measurement models to gain the uncertainties for the output quantities. For this purpose, a Monte Carlo method is used. Monte Carlo methods for uncertainty quantification rely on repeated random sampling to obtain the numerical results. It is widely used in science and engineering to investigate the impact of statistical uncertainty in specific input quantities on the output quantities. In the Monte Carlo method, at first the domain of possible inputs and their probability distributions are defined. Afterwards the inputs are randomly generated from the given distributions. For each set of input parameters, a computation is performed and the output of interest is determined. At the end, using statistical methods, a distribution of the obtained results is analyzed. A very important parameter for the Monte Carlo method is the number of simulations performed. The statistical distribution of the output variables is only valid (converged) if enough sets of input parameters were tried. Mostly, the number of required simulations is in the range of thousands or tens of thousands for a statistical convergence. Technically, results should be generated with all possibilities and combinations of the input parameters.

So, the first step is to identify the uncertain input quantities in the setup and obtain the corresponding ranges of uncertainty. In short, the FSM-FRS experiment consists of focusing a laser beam of a certain power to a point, scanning the laser frequencies, and detecting the scattered light. From this simple explanation, the potential noise sources can already be isolated: the laser power fluctuates around the mean value. Also, when scanning the laser frequency, the frequency value is uncertain. There is an uncertainty in the light detection process as well. So, it was decided to include these three major noise sources in the e2e simulator. The second step is to determine the uncertainty ranges for the input quantities. The laser power distribution can be assumed to have a Gaussian shape, centered around the mean power value P_L, at which the laser is operating. The standard deviation of this Gaussian distribution σ_L provides an estimate of the error in the laser power. Manufacturers often specify the relative error in the laser power, defined as $\sigma_L/P_L \cdot 100$, given in percentages. With this value known, one can calculate the uncertainty range of the laser power and correspondingly the statistical distribution of the laser intensity. The same can be said about the uncertainties in measuring the laser frequency using a wavemeter. However, the frequency that is measured by a wavemeter can be slightly different from the actual laser frequency. Instead of the relative error, manufacturers define σ_ν which is the standard deviation of the frequency measurement distribution centered around the mean value ν_c at which the laser is operating. So, by knowing σ_ν and σ_L, one can calculate the statistical distributions of the input parameters ν_c and P_L.

The detection noise is slightly more complicated as it depends on the detector. However, by choosing the optimal detector, one can usually assume that the photon shot noise is the limiting factor. The photon shot noise originates from the discrete nature of the electric charge and occurs in the photon counting devices. Shot noise is a Poisson noise by nature. However, for a large number of samples in the distribution (large number of photons, electrons, etc.), it approaches a normal distribution around its mean and becomes indistinguishable from Gaussian noise. Jagodzinski (2007) showed that the shot noise was indeed the most dominant noise source for a PMT detector. Forkey (1996) utilized a CCD camera for the measurements and also used an assumption of shot noise being the limiting factor in the light detection process. Eq. 3.17 and 3.18 show the number of released photoelectrons in the detector. Again, the actual number is slightly different due to the shot noise. Assuming that the number of photoelectrons is large enough, the standard deviation of a Gaussian shot noise is simply given by

$$\sigma_N(\nu_c) = \sqrt{N_{PE}(\nu_c)} \tag{4.22}$$

$$\sigma_N(\bar{\nu}_c) = \sqrt{N_{PE}(\bar{\nu}_c)} \tag{4.23}$$

centered around $N_{PE}(\nu_c)$ and $N_{PE}(\bar{\nu}_c)$. So, for a given interrogation case, the detector generates any number of photoelectrons from this distribution. It is important to note that the uncertainty in the number of photoelectrons counted depends on the signal level. As N_{PE} gets higher, the relative shot noise decreases because the rate at which σ_N increases is lower.

Eq. 4.23 can only be used for calculating σ_N of the induced photoelectrons distribution for a direct-detection FSM-FRS. For modulated FSM-FRS, error propagation must be used. It is easier to denote some of the terms by constants when doing the derivation:

$$C_0(\bar{\nu}_c) = \epsilon\eta \frac{I_L(\bar{\nu}_c)\mathrm{d}t}{h(\bar{\nu}_c + \Delta\nu_D)} \frac{PV(\bar{\nu}_c)}{k_B T} \frac{\partial\sigma}{\partial\Omega}(\bar{\nu}_c)\Omega \tag{4.24}$$

$$S_0(\bar{\nu}_c) = \int_{\Delta \mathrm{d}t} \int_{-\infty}^{+\infty} \tau(\nu) g\big(\theta, T, P, \nu - (\nu_c(t) + \Delta\nu_D)\big) \mathrm{d}\nu \mathrm{d}t \tag{4.25}$$

$$S_1(\bar{\nu}_c) = \int_{\Delta \mathrm{d}t} \int_{-\infty}^{+\infty} S_L{}'(\nu, a) g\big(\theta, T, P, \nu - (\nu_c(t) + \Delta\nu_D)\big) \mathrm{d}\nu \mathrm{d}t \tag{4.26}$$

$$S_2(\bar{\nu}_c) = \int_{\Delta \mathrm{d}t} \int_{-\infty}^{+\infty} S_L{}''(\nu, a) g\big(\theta, T, P, \nu - (\nu_c(t) + \Delta\nu_D)\big) \mathrm{d}\nu \mathrm{d}t \tag{4.27}$$

So, it can be noticed that $N_{PE}(\bar{\nu}_c) = C_0 S_0$, $N_{PE}{}'(\bar{\nu}_c) = C_0 S_1$, and $N_{PE}{}''(\bar{\nu}_c) = C_0 S_2$. From this, it can be seen that $C = \frac{N_{PE}(\bar{\nu}_c)}{S_0}$. Then the formulae for the modulated spectra become:

$$N_{PE}{}'(\bar{\nu}_c) = N_{PE}(\bar{\nu}_c) \frac{S_1(\bar{\nu}_c)}{S_0(\bar{\nu}_c)} \tag{4.28}$$

$$N_{PE}{}''(\bar{\nu}_c) = N_{PE}(\bar{\nu}_c) \frac{S_2(\bar{\nu}_c)}{S_0(\bar{\nu}_c)} \tag{4.29}$$

$$N_{PE}{}^R(\bar{\nu}_c) = \frac{S_1}{S_2} \tag{4.30}$$

With the error propagation formula, the standard deviation in $N_{PE}(\bar{\nu}_c)$ can be propagated into $N_{PE}{}'(\bar{\nu}_c)$ and $N_{PE}{}''(\bar{\nu}_c)$ as follows:

$$\sigma_N{}'(\bar{\nu}_c) = \sigma_N \frac{S_1(\bar{\nu}_c)}{S_0(\bar{\nu}_c)} \tag{4.31}$$

$$\sigma_N{}''(\bar{\nu}_c) = \sigma_N \frac{S_2(\bar{\nu}_c)}{S_0(\bar{\nu}_c)} \tag{4.32}$$

With this, the shot noise and the corresponding distribution in $N_{PE}{}'(\bar{\nu}_c)$, $N_{PE}{}''(\bar{\nu}_c)$, and $N_{PE}{}^R(\bar{\nu}_c)$ can be assessed as well. For ratios, each harmonic spectrum has to be computed and the noise added to it. Then, they need to be divided to calculate $1f/2f$ signal.

Now the uncertainty ranges (probability distribution functions) have been determined for P_L, ν_c, $N_{PE}{}'(\nu_c)$, $N_{PE}(\bar{\nu}_c)$, $N_{PE}{}'(\bar{\nu}_c)$, $N_{PE}{}''(\bar{\nu}_c)$, and $N_{PE}{}^R(\bar{\nu}_c)$. This information can be used to perform the statistical uncertainty analysis using the e2e simulator. The Monte Carlo method is incorporated as follows:

1. Values for pressure, temperature and the velocity vector are set depending on the flow case.

2. For a discrete FSM-FRS, the random variables P_{Li}, ν_{ci} are generated for each discrete frequency from the respective Gaussian input distributions.

3. For continuous and modulated FSM-FRS, the random variable ν_{ci} is generated for the first and the last laser frequencies in the scan. Then the corresponding frequency intervals for the integration are determined and the mean frequencies within the integration bands are found. Afterwards, for each mean frequency, the random variable P_{Li} is generated.

4. The flow parameters from step 1 and the generated random variables are used to determine $N_{PE_i}(\nu_c)$, $N_{PE_i}(\bar{\nu}_c)$, $N_{PE_i}{}'(\bar{\nu}_c)$, $N_{PE_i}{}''(\bar{\nu}_c)$, or $N_{PE_i}{}^R(\bar{\nu}_c)$.

5. Values obtained in step 3 are used to determine $\sigma_{N_i}(\nu_c)$, $\sigma_{N_i}{}'(\bar{\nu}_c)$, $\sigma_{N_i}{}''(\bar{\nu}_c)$, and $\sigma_{N_i}{}^R(\bar{\nu}_c)$.

6. Results from steps 4 and 5 are used to randomly generate new $N_{PE_i}(\nu_c)$, $N_{PE_i}(\bar{\nu}_c)$, $N_{PE_i}{}'(\bar{\nu}_c)$, $N_{PE_i}{}''(\bar{\nu}_c)$, or $N_{PE_i}{}^R(\bar{\nu}_c)$ from their respective distributions due to detection (shot) noise.

7. Obtained noisy spectrum $N_{PE_i}(\nu_c)$, $N_{PE_i}(\bar{\nu}_c)$, $N_{PE_i}{}'(\bar{\nu}_c)$, $N_{PE_i}{}''(\bar{\nu}_c)$, or $N_{PE_i}{}^R(\bar{\nu}_c)$ is used to calculate P_i, T_i, u_{D_i} (pressure, temperature, and Doppler velocity) using the Levenberg-Marquardt least-square fitting algorithm.

8. Steps 1-6 are performed N_{MC} times for $i = 1 \ldots N_{MC}$ and the fitted parameters are saved.

9. Statistical methods are applied to assess the uncertainty in the flow parameters and calculate a signal-to-noise ratio SNR:

$$\bar{P} = \frac{\sum_{i=1}^{N} P_i}{N_{MC}}, \qquad \sigma_P = \frac{\sum_{i=1}^{N} \left(P_i - \bar{P}\right)^2}{\sqrt{N-1}} \tag{4.33}$$

$$\bar{T} = \frac{\sum_{i=1}^{N} T_i}{N_{MC}}, \qquad \sigma_T = \frac{\sum_{i=1}^{N} \left(T_i - \bar{T}\right)^2}{\sqrt{N-1}} \tag{4.34}$$

$$\bar{u}_D = \frac{\sum_{i=1}^{N} u_{D_i}}{N_{MC}}, \qquad \sigma_{u_D} = \frac{\sum_{i=1}^{N} \left(u_{D_i} - \bar{u}_D\right)^2}{\sqrt{N-1}} \tag{4.35}$$

$$SNR(\nu_c) = \frac{N_{PE}(\nu_c)}{\frac{\sum_{i=1}^{N_{MC}} \left(N_{PE_i}(\nu_c) - N_{PE}(\nu_c)\right)^2}{\sqrt{N_{MC}-1}}} \tag{4.36}$$

   where $N_{PE}(\nu_c)$ is an ideal spectrum calculated using the theoretical flow parameters from step 1, and $N_{PE_i}(\nu_c)$ is a noisy spectrum. This SNR calculation procedure is only valid for non-negative signals, i.e. a number of photons, photoelectrons, etc.

10. Doppler velocities are used to calculate the actual velocity components (described more specifically in section 4.4).

With a sufficiently large number of simulations, the averages of the flow parameters converge to the theoretical values from the step 1. This happens because the input and therefore the output parameters are normally distributed around their mean values, and with a large number of simulations the noise is averaged out.

4.3. Experimental Probe Layout

An experimental layout of the FSM-FRS probe is shown in Fig. 3.1 and 3.2. It consists of one light emitting and one receiving unit. Such configurations can only measure one velocity component along the $(\hat{O} - \hat{L})$ direction. The scattering angle θ can be adjusted for any experiment. This layout is addressed as geometry 1 throughout the report. Optical parameters such as the collection lens diameter and the focal length can also be varied.

4.4. OSIRIS Probe Layout

For the project OSIRIS, the proposed laser system must be placed inside the airplane cabin. The beam is guided by fiber optics through the airplane window with a diameter of 15 cm and is focused outside. The focal point is 25 cm from the window to keep it outside of the boundary layer. The scattered light is also collected through the same window. A tentative requirement of using the collection lens with $f_{\#} = 10$ is set. This ensures that sufficient light is collected and at the same time the systematic uncertainty due to the small lens angle assumption is negligible (Doll (2016), Forkey (1996)). For measuring all three velocity components, it is necessary to have a combination of several light emitters and receivers. These can be arranged in different ways and an ideal configuration can be determined. The main motivation for optimizing the probe layouts is to optimize the frequency scanning range which translates into lower uncertainties in temperature, pressure, and velocity. There are two types of units conceived for this project: one is the emitter/receiver unit, the other is just a receiver. The emitter/receiving unit emits and focuses the laser beam and also collects the scattered light with one and the same optics. Since the scattered light is collected in the opposite direction to the laser propagation, the emitter/receiver unit is operating in backscattering mode, where $\theta = 180°$. A possible layout of such a backscattering unit has been proposed by Enns (2014) in his master thesis at DLR and is given in Fig. 4.3. This setup is similar to a generic FRS experimental setup, as given in Fig. 3.5, with several modifications. First and foremost difference is that the scattered light is collected backwards at $\theta = 180°$. A pinhole in front of the detector is used to reduce out-of-focus light and thus limit the signal detection to the desired volume of interest, as explained in section 3.2. The laser is delivered to the focusing lens via an optical fiber. An interference filter (bandpass filter) is used to filter out the fluorescence of the molecular filter (also part of a generic FRS setup). The receiver

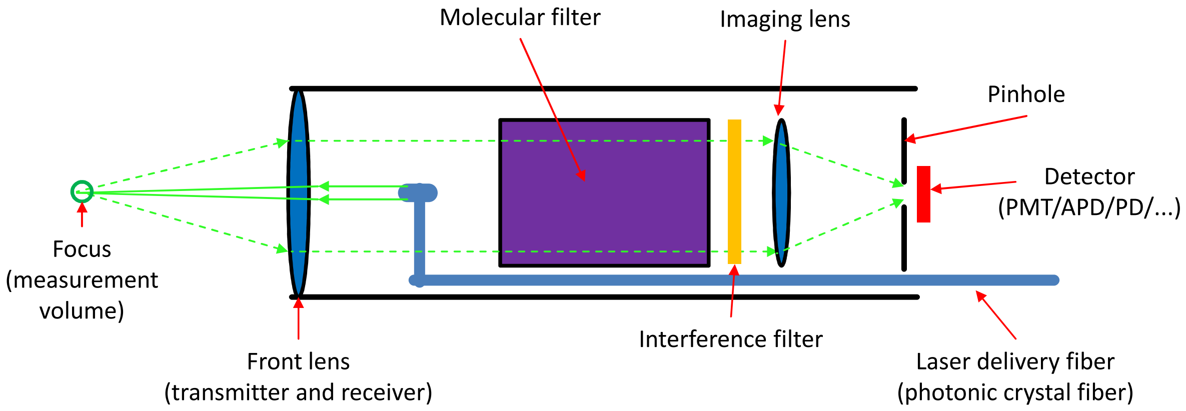

Figure 4.3: OSIRIS emitter/receiver unit layout

unit is very similar to the emitter/receiver unit. It has basically the same setup as shown in Fig. 4.3, but there is no laser delivery fiber. So, it just collects scattered light from the focus which is illuminated by other light sources.

Geometry 1

For OSIRIS, geometry 1 is used with a fixed scattering angle of 180° based on a lens with a focal length of 25 cm and a diameter of 2.5 cm, as shown in Fig. 4.4. Needless to say, it can not measure all three velocity components. It can only determine a single velocity component. This geometry can be realized with the probe shown in Fig. 4.3. Since the scattering angle is exactly 180°, the measured Doppler velocity is related to the actual velocity in the following way:

$$u = -\frac{u_D}{2} \tag{4.37}$$

In the context of project OSIRIS, geometry 1 is used to perform those parameter optimizations that are more or less independent of the probe configuration with multiple receiver/emitter units (3C probe). The proposed geometries for measuring all velocity components are composed of several emitter/receiver units. So each filter's temperature, length and absorption well can be optimized using the model of a single backscattering probe (1C probe) because the observed spectral shapes of the scattered light are similar. Performing these optimizations on complex probes with multiple emitter and receiver units requires much more computing capacity.

Geometry 2

Geometry 2 consists of three backscattering emitter/receiver units with $\theta = 180°$ that operate through different airplane windows, as shown in Fig. 4.4. The laser light propagation and observation directions are shown by the double-headed blue arrows. One emitter/receiver unit is directed in the main flight direction (along u-velocity). The front lens is integrated into an airplane window. Two other units do exactly the same thing but along v and w directions. All three beams come from the same laser system and pass the window perpendicularly. As before, lenses with a focal length of 25 cm and a diameter of 2.5 cm are used. It is assumed that the velocity field around the airplane outside of the boundary layer is the

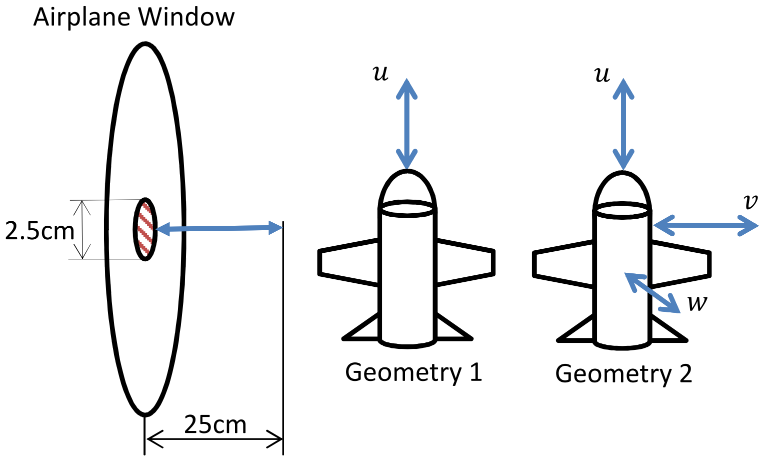

Figure 4.4: Simple geometries for measuring single/multiple velocity components

same. Therefore, the velocity vectors at all three focal spots are equal. Since the scattering angle is exactly 180° for each unit, the Doppler velocity measured in each direction is related to the actual velocity components in the following way:

$$u = -\frac{u_{D_u}}{2}, \qquad v = -\frac{u_{D_v}}{2}, \qquad w = -\frac{u_{D_w}}{2} \tag{4.38}$$

After the three spectra are obtained from these three units, they are evaluated together. It is assumed that temperature and pressure are the same for all three focal spots. So, in simulations, only 5 parameters are fitted: temperature, pressure, and three Doppler velocities.

It is important to note that in order to fulfil the criterion of keeping the filter transmission below 10^{-5} for geometric and particle stray light, the frequency scanning range (useful filter absorption linewidth) is limited and determined by the velocity component that causes the highest net Doppler shift, $\Delta\nu_D$. This is the airplane forward velocity, u. The Doppler velocity, and therefore the net Doppler shift $\Delta\nu_D$ are very high if the backscattering emitter/receiver unit is aligned with the velocity vector ($\vec{v}$ parallel to $\hat{O}-\hat{L}$), as it is the case for geometry 2. Since the forward velocity (u-component) is considerably higher than the other components, the emitter/receiver aligned along u observes the highest net Doppler shift. This is a limiting factor for the frequency scanning range since the laser frequencies must be same for all emitter/receiver units (because a single laser system is used). It must also be mentioned that the sensitivity towards the u-velocity is also highest in this case.

Geometry 3

Geometry 3 is a much more complex configuration. Again, three emitter/receiver units are utilized in a backscattering mode with $\theta = 180°$. However, they operate through the same airplane window and therefore are not perpendicular. This configuration is visualized in Fig. 4.5. As before, the same laser system is used for all units and it is assumed that the velocity vectors at all foci are same. The three emitter/receiver units are oriented at an angle α with respect to each other, with their front lenses being integrated into the one window. While the perpendicular distance of the focal points from the window still is 25 cm, the actual focal length of the lenses is higher and depends on α since the observation direction is not normal to the window anymore. So, in order to keep $f_\# = 10$, the diameters of the lenses should be increased correspondingly. However, it must be ensured that all three collection lenses can still fit into a 15 cm diameter window.

Laser propagation and observation directions are not aligned with the velocity vector of the airplane any more. Therefore, transformations must be made to compute the actual velocity components. For each receiving unit, $(\hat{O}-\hat{L})$ can be defined as OL_1, OL_2, and OL_3 so that

$$u_{D_1} = \vec{v}\cdot OL_1, \qquad u_{D_2} = \vec{v}\cdot OL_2, \qquad u_{D_3} = \vec{v}\cdot OL_3 \tag{4.39}$$

where each vector quantity has x, y, and z components with $\vec{v} = (u, v, w)$. Eq. 4.39 can be expanded into:

$$\begin{aligned} OL_{1_x}u + OL_{1_y}v + OL_{1_z}w &= u_{D_1} \\ OL_{2_x}u + OL_{2_y}v + OL_{2_z}w &= u_{D_2} \\ OL_{3_x}u + OL_{3_y}v + OL_{3_z}w &= u_{D_3} \end{aligned} \tag{4.40}$$

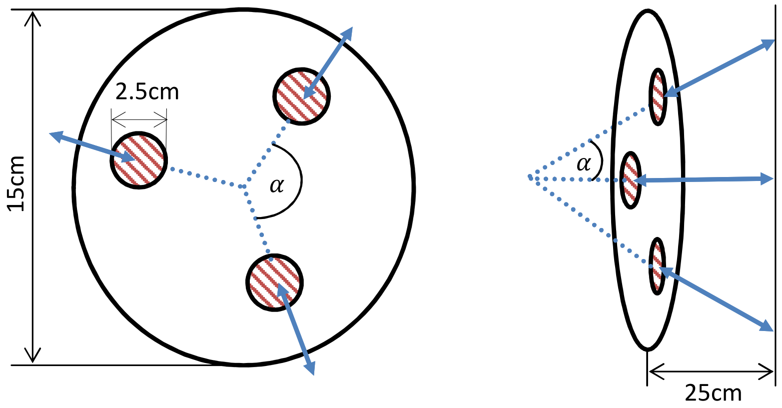

Figure 4.5: Airplane window with a multiple emitter/receiver configuration

This is a system of three equations with three unknowns, so Cramer's rule can be used to determine the velocity vector from the three Doppler velocity values. Again, temperature and pressure are assumed to be constant for all probe positions so only 5 parameters are fitted: temperature, pressure, and three Doppler velocities.

For geometry 3 the angle α can be optimized. This angle determines the sensitivity in the actual velocity components and also the maximum Doppler shifted frequency that limits the frequency scanning range. As a result by minimizing the net Doppler shift and thus maximizing the scan range, geometry 3 allows to reduce the associated measurement uncertainties without sacrificing the sensitivity in the velocity components.

The probe layout imposes limitations for α, namely $0^\circ < \alpha < 120^\circ$. If $\alpha = 0$, all laser beams are aligned along the v-component of the velocity, and there is no sensitivity in other directions. For $\alpha = 120^\circ$ the beams would be in the same plane (parallel to the window) and there would be no sensitivity towards the v-component of the velocity. The values $\alpha > 120$ are physically impossible since the detection units would be directed inwards. In the simulations, a dynamic range with $5^\circ < \alpha < 105^\circ$ has been utilized. Additionally the whole system can be rotated to see if that has any effect.

Geometry 4

In geometry 4 there is only one emitter/receiver unit, complemented by four additional receiver units as visualized in Fig. 4.6: the orientation of the emitter/receiver unit is denoted by the blue arrow, that of the receivers by the green ones. The emitter/receiver unit and thus the laser beam is perpendicular to the window. So, like in geometry 1 and 2, the focal length and the diameter of the lens in this unit are 25 cm and 2.5 cm, respectively. For the receiver units, focal length and diameter of the collection lens depend on α as in geometry 3. While the the central emitter/receiver unit works in backscattering mode with $\theta = 180^\circ$, the four receiving units feature $90^\circ < \theta = (180^\circ - \alpha) < 180^\circ$, which is still considered as a backscattering mode.

In this probe configuration, the laser propagation and observation directions are also not aligned with the velocity vector of the airplane. Therefore, the transformations are required. For each receiving unit, $(\hat{O} - \hat{L})$ can be defined as OL_1, OL_2, OL_3, OL_4, and OL_5 so that

$$u_{D_1} = \vec{v} \cdot OL_1, \quad u_{D_2} = \vec{v} \cdot OL_2, \quad u_{D_3} = \vec{v} \cdot OL_3, \quad u_{D_4} = \vec{v} \cdot OL_4, \quad u_{D_5} = \vec{v} \cdot OL_5 \tag{4.41}$$

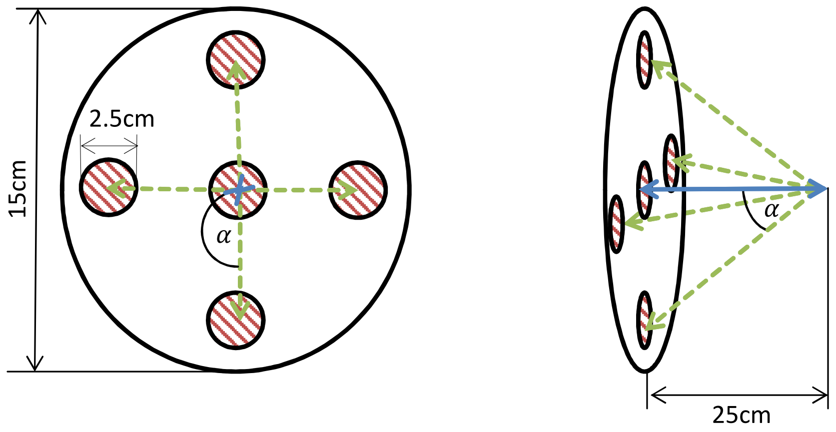

Figure 4.6: Airplane window with a single emitter and multiple receiver configuration

where each vector quantity has three components. Eq. 4.39 can be expanded into:

$$
\begin{aligned}
OL1_x u + OL1_y v + OL1_z w &= u_{D_1} \\
OL2_x u + OL2_y v + OL2_z w &= u_{D_2} \\
OL3_x u + OL3_y v + OL3_z w &= u_{D_3} \\
OL4_x u + OL4_y v + OL4_z w &= u_{D_4} \\
OL5_x u + OL5_y v + OL5_z w &= u_{D_5}
\end{aligned}
\tag{4.42}
$$

This is a system of equations with three unknowns and five equations. So, the system is overdetermined and there is more information than required. The additional information can be used to enhance accuracy, if the system is solved using a least-squares method. In this case, spectra from all receivers are combined and 7 parameters are fitted in the simulations: temperature, pressure, and five Doppler velocities.

The idea behind geometry 4 is also to make the trade-off between the sensitivity towards the velocity components on the one hand and the frequency scanning range on the other hand. So, the angle α can be optimized for this geometry as well. However, α is strongly limited by the window size: according to the project specifications, the diameter of the window is 15 cm. Taking into account the lens diameters, this translates into an angular limitation of approximately $10° \leq \alpha \leq 15°$. This results in the scattering angles close to 180° for receiver which in return limits the sensitivity towards the u and w velocity components. Rotating this probe may also have some effects.

The receiver unit does not include a laser source. So, from a technical perspective, there could be as many receivers as possible. Accuracy of the FSM-FRS techniques increases with the redundancy of the information. However, taking into account the airplane window size and geometry, it would be difficult to have more than four receivers without further restricting α.

4.5. Functionality

4.5.1. Input

The input for the e2e simulator is divided into three blocks: laser parameters, optical parameters, and simulation parameters. Additionally a filter transmission function must be integrated into the code.

- Laser parameters include: laser power, relative uncertainty in laser power, laser wavenumber scanning resolution, central wavenumber of the filter absorption well to be scanned, frequency scanning method, laser frequency modulation amplitude (only for modulated FSM-FRS), laser frequency standard deviation, FWHM of the laser linewidth, laser M^2 value.
- Optical parameters include: chosen geometry, scattering angle (only for geometry 1), geometric configuration angle and rotation angle (only for geometries 3 & 4), focal lengths and diameters of the collection and focusing lenses, optical and quantum efficiencies, filter cell temperatures and lengths, number of radial and annular lens sections (4.2.1).
- Simulation parameters include: simulation resolution (convolution, integration, etc.), measurement rate (temporal resolution), number of Monte Carlo simulations, temperature, pressure, and velocity vector of a flow (for geometry 1 only one component is measured. This can be chosen by the user).

All input parameters mentioned above are user specifiable in a dialogue box. It must be noted that the geometric configuration angle determines the scattering angle for geometry 4.

4.5.2. Output

The output of the e2e simulator includes the following:

- Systematic deviations (bias errors) in the flow parameters due to the model assumptions as discussed in section 4.2.1.
- Statistical uncertainties in the flow parameters due to the random noise in different input parameters as explained in section 4.2.2.
- Percentage of Rayleigh scattered light transmitted through the filter and an estimate of relative photon shot noise when the central scattering frequency is in the center of a filter absorption well.
- Plots of the statistical distribution of the flow parameters, frequency-wise signal to noise ratio, and one exemplary Monte Carlo simulation based on a noisy spectrum with the corresponding fitted curve.

4.6. OSIRIS Parameters

Some technical requirements for OSIRIS have already been mentioned before. They limit the extent to which some of the input parameters can be varied. However, there is some input which needs to be adapted before embarking on an optimization. These parameters are related to the laser and the molecular absorption filter.

The filter and the laser are crucial components of an FRS experiment. As one can see in Fig. 3.4 and 3.8, the laser frequency must coincide with a filter absorption feature. There are several laser-filter combinations that can be used for FRS. For example, a green laser may match an absorption filter containing molecular iodine, also some ultravilolet lasers may be

Parameter	Unit
Laser wavelength range	~532 nm, green
Error in laser frequency	< 2 MHz
Frequency scanning time	1 s
Error in laser power	< 1%
Beam quality, M^2	< 1.1
Beam diameter, D_L	1 mm
Laser linewidth	<5 MHz
Laser power	2W
Window diameter	15 cm
Collection lens f	25 cm
Collection lens D	2.5 cm
Collection lens $f_\#$	10
P (to be measured)	26500 Pa
T (to be measured)	225 K
$\hat{v}$ (to be measured)	$(250, 25, 25)$ m/s
Geometry 3, angle α	$5 - 105°$
Geometry 4, angle α	$10 - 15°$

Table 4.1: Parameters for OSIRIS

combined with filters based on mercury. It is even possible to use some infrared lasers in combination with a potassium atomic vapor filter cell, however the intensity of the Rayleigh scattered light increases with the 4^{th} power of the incident laser frequency. So, in general shorter wavelengths are preferable. This also needs to be taken into account when choosing these components.

For OSIRIS, it was decided to perform simulations and parameter studies with a green laser, the corresponding molecular filter medium is iodine. This combination was chosen for several reasons: first of all, the transmission of iodine cells is very well documented (Forkey, 1996) and is also available as a numerical model. Secondly, a green laser, namely a Coherent Verdi V5, as well as iodine filter cells are already available at the DLR Institute of Propulsion Technology. This laser fulfills the lineshape requirements for OSIRIS. So, this equipment can be used to perform FSM-FRS experiments and validate the end-to-end simulator.

Since the green light is within the visible range, alignment is not very difficult. The power of the laser for a single emitter unit is limited to 2 W. This is due to the eye safety and spatial limitations on board of the airplane which sets how big the laser system can be. The beam diameter depends on the used fiber, however a diameter of 1 mm can be assumed since it is a typical dimension of experiments using a photonic crystal fiber. The used values for the uncertainties in laser power and frequency measurements also came from the specifications of the instruments present at DLR. They are given in table 4.1 together with the other parameters specified for OSIRIS.

4.6.1. Iodine Filter

As mentioned, the most appropriate absorption medium when using green lasers is iodine. The absorption of the iodine filter depends on the cell length (optical path length of the light through the filter medium) and the saturation temperature, at which all the iodine in the cell has been vaporized and is in the gaseous state. Cell length and temperature can be varied and optimized to improve the accuracy of the FSM-FRS methods. Therefore, it is necessary to model and determine the iodine filter transmission as a function of these parameters.

Forkey (1996) provides a semi-empirical numerical model programmed in FORTRAN for calculating the iodine absorption/transmission. When light passes through the filter cell, the iodine electrons absorb the photons and jump onto higher energy states. Iodine has many electronic, vibrational and rotational levels, but only few of them are involved in the transitions triggered by visible light. Based on these transitions Forkey used measured spectroscopic constants from literature to model the absorption of iodine filters as a function of the filter cell temperature and length.

Cell length and temperature are very important parameters because they strongly affect the thermal and pressure broadening of the spectral lines. However, Forkey was primarily interested in the location, shape, and strength of the discrete absorption lines. So, his model only includes transitions between specific bound electronic states and doest not account for the frequency-independent continuum generated by the unbound state, i.e. background absorption. Since the goal of the simulator is to optimize different parameters, including the filter cell temperature and length, it is necessary to model the background continuum as well. This can be done using the spectroscopic constants tabulated by Tellinghuisen (1982). For uniform attenuation of a single species filter (made up of one element), the Beer-Lambert Law states:

$$\tau_u = 10^{-\varepsilon c L} \tag{4.43}$$

where τ_u is the transmission due to unbound states, ε is the corresponding molar attenuation coefficient, c is the molar concentration of the sample species, and L is the filter cell length. ε can be obtained from the article by Tellinghuisen (1982), the filter length is a variable that can be adjusted. The molar concentration of the iodine can be found using the ideal gas law:

$$c = \frac{n}{V} = \frac{P}{RT} \tag{4.44}$$

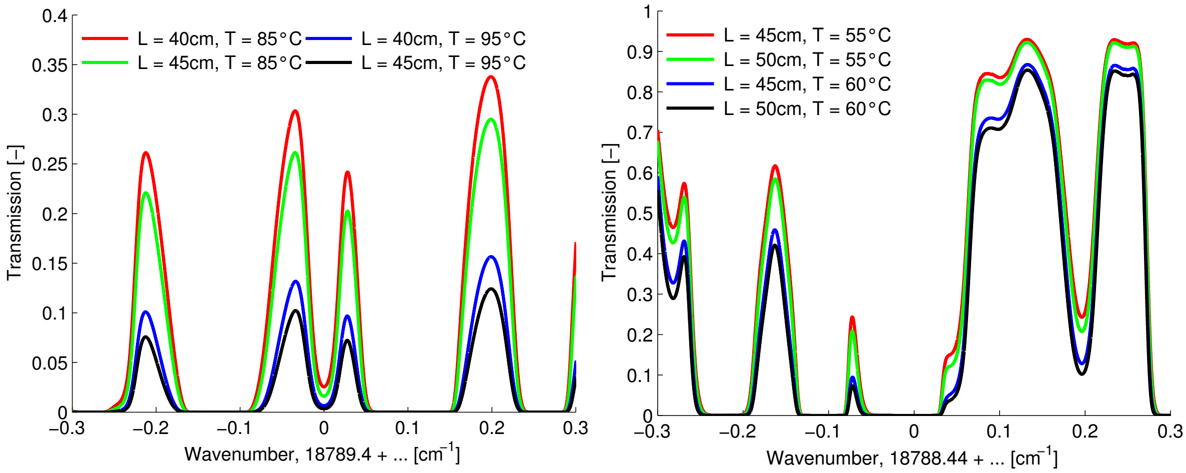

(a) Transmission near 18789.3, 18789.5 cm^{-1}

(b) Transmission near 18788.44 cm^{-1}

Figure 4.7: Iodine filter transmission vs. cell temperature and length

where P and T are the saturation pressure and temperature of the cell and R is the ideal gas constant. With this, the transmission due to unbound states τ_u can be calculated as a function of the filter temperature and length. Then, it can be combined with the filter transmission due to the bound electronic states, τ_b, calculated using Forkey's (1996) model, to yield a total filter transmission given by:

$$\tau = \tau_b \cdot \tau_u \tag{4.45}$$

The augmented iodine transmission model can be used in the e2e simulator for optimization purposes. To maximize the accuracy of the FSM-FRS methods, it is imperative to find the best combination of the filter parameters. Fig. 4.7 shows the transmission of the iodine filter as a function of the cell length and temperature for several absorption features, located at the wavenumbers 18788.44 cm^{-1}, 18789.3 cm^{-1}, and 18789.5 cm^{-1}. As can be seen, increasing the filter length broadens the absorption feature and decreases the overall transmission. As the saturation temperature gets higher, the linewidth of the absorption well also increases and the overall transmission drops.

5

Simulations

Simulations performed by the end-to-end simulator are used to mimic actual FSM-FRS measurements and calculate the expected accuracies in the flow parameters. Results of these simulations are used to optimize different FRS parameters. There are many variables that can be optimized. These include the filter parameters (cell length, temperature, absorption feature), geometric parameters (angles between emitters and receivers), frequency scanning methods (discrete, continuous, modulated), etc. Due to complexity and a required computational time, it is not feasible to optimize all parameters simultaneously. Therefore, they will be investigated consecutively.

Before analysing 3C probe configurations, some of the parameters need to be optimized using a simple backscattering 1C probe configuration, as shown in Fig. 4.3. The results are transferable because the 3C probes are just combinations of these backscattering (with $\theta = 180°$ or being close to 180° for geometry 4) 1C probes. For example, the filter parameters affect the filter transmission and the absorption feature linewidth; for 1C and 3C probes these effects are the same. However, the frequency scanning range depends on both the absorption feature linewidth and the maximum net Doppler shift. The latter varies among the different probe configurations, because the magnitude and the direction of the velocity components measured changes with the probe configurations. However, the net Doppler shift is always in between the values associated with the velocities of 25 m/s (smaller net Doppler shift) and 250 m/s (higher net Doppler shift). Therefore, one could optimize the filter and other general simulation parameters for these two velocities. Afterwards, the optimized sets of parameters can be further compared using the 3C probe configurations.

Since pressure, velocity, and temperature are equally important, the optimization is based on the norm of the relative uncertainty (error) in parameters. For a 1C probe, a backscattering emitter/receiver unit is aligned with a velocity component of 25 m/s or 250 m/s. This velocity component can be directly measured because it is parallel to the laser propagation and observation directions. The norm of the uncertainty is given by:

$$\text{Norm of Error} = \sqrt{\Delta T^2 + \Delta P^2 + \Delta u^2} \tag{5.1}$$

where a the percent uncertainty in one parameter, defined as $\Delta x = \sigma_x / x_0 \cdot 100$ with σ_x being the statistical standard deviation of the respective flow parameter and x_0 its originally set (actual) value. The variable x can be p, T, u, v, or w. For a 3C probe, since all velocity components are measured, the norm is:

$$\text{Norm of Error} = \sqrt{\Delta T^2 + \Delta P^2 + \Delta u^2 + \Delta v^2 + \Delta w^2} \tag{5.2}$$

For all simulations, temperature and pressure are set to cruise altitude values, 225 K and 26500 Pa, respectively. For a 3C probe, the velocity vector is defined as (250, 25, 25) m/s, where the highest component is in the forward direction. Such a velocity vector ensures that the 3C probe can be tested on the perpendicular velocity components which are significantly smaller then the forward one. Also, it is very similar to the actual velocity vector of the airplane where the forward velocity component is dominant.

Optimizations are performed based on direct-detection discrete frequency scanning FRS method, unless specified otherwise. First of all, it requires less computational time than the other frequency scanning methods, secondly, it is the foundation of FSM-FRS from which the other techniques were developed. Again, the idea is to optimize the filter transmission and the frequency scanning range/resolution. It should not matter which FRS-FSM method is used because all of them are equally affected by these parameters. All uncertainties given in tables are rounded upwards. The temporal resolution is 1 Hz (overall measurement time is 1 s). It is important to note that there is no such thing as a minimum velocity that can be measured. As the Doppler sensitive component of the velocity increases, the Doppler shift gets bigger and the frequency scanning range decreases. This adversely affects accuracies in the flow parameters. From this perspective, flow with a zero velocity will have the lowest absolute uncertainties.

5.1. Monte Carlo Convergence

Parameter optimization is based on the statistical uncertainties in temperature, pressure, and velocity which are combined into a single norm of uncertainty (error), relying on Monte Carlo simulations. Since computing capacity is an issue when performing Monte Carlo simulations, it is important to know how many simulations are sufficient such that the statistics are converged. The main goal is not to have the output parameter convergence to the smallest scale possible, but to investigate trends and effects of the input parameters. For two cases with different flow velocities and filter lengths, the number of Monte Carlo simulations was varied from 125 to 32000 in a geometric progression (doubling the number

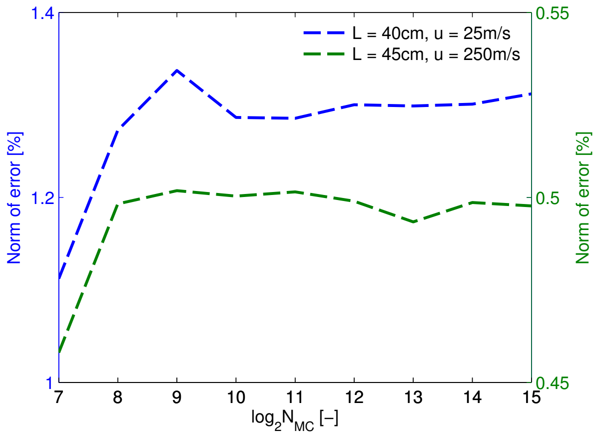

Figure 5.1: Monte Carlo convergence

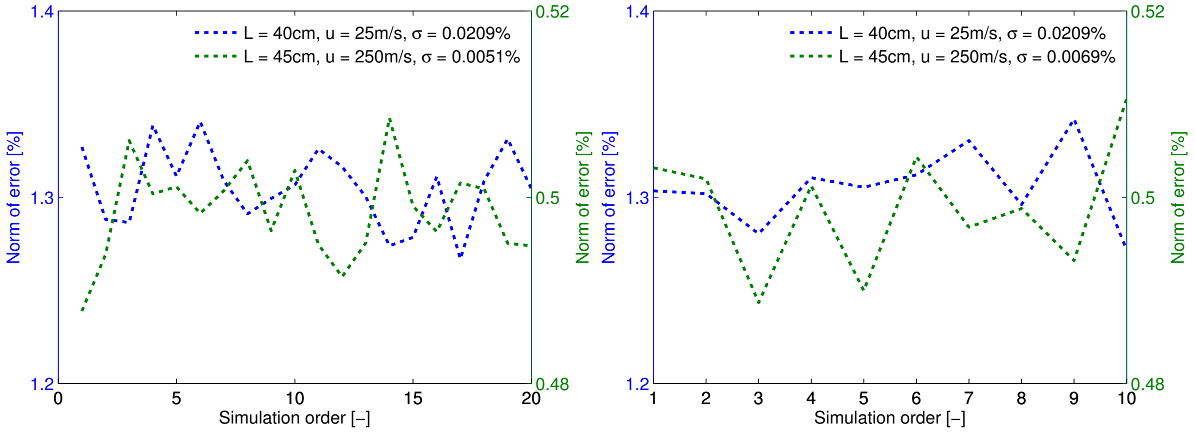

(a) $N_{MC} = 1000$ (b) $N_{MC} = 2000$

Figure 5.2: Monte Carlo simulation consistency

of simulations, N_{MC}, after each step). In both cases, the filter temperature T_F was 85°C and the used iodine absorption feature was the one located at 18789.5 cm^{-1}. The filter lengths L were 40 cm and 45 cm. The wavenumber scanning resolution was 0.001 cm^{-1}. It must be mentioned that these filter parameters are arbitrary and of minor importance for the Monte Carlo convergence.

The obtained results are given in Fig. 5.1. On the logarithmic x-axis, numbers 10-11 correspond to 2^{10} and 2^{11} (approximately 1000 and 2000) Monte Carlo simulations. It seems that they are already sufficient for a sub-percent convergence. To double check this, a series of repeated simulations with identical parameters were performed with $N_{MC} = 1000$ and $N_{MC} = 2000$, the results are given in Fig. 5.2. As can be seen, the standard deviation of the normalized error is in the range of 0.02% or less. So, the aim of resolving percent differences in the relative measurement uncertainty is met. Therefore, from now on, 1000 simulations are used to make preliminary studies and 2000 simulations are used to verify results that have only small variations.

5.2. Wavenumber resolution

Very important factor is the laser wavenumber scanning resolution. As the resolution becomes finer, there are more frequencies available to scan and more data to be used in least-squares fitting. However, as the overall measurement rate is set to 1 Hz, the exposure time for each scanning frequency (or time over which a continuously scanned frequency is integrated) decreases inversely proportional. To make the best use of the given time this trade-off must be investigated. The study has been performed on the same flow cases as before. A filter temperature was 85°C and the 18789.5 cm^{-1} iodine absorption feature was used. The filter lengths 40 cm and 45 cm depending on the velocity. The wavenumber scanning resolution was varied from 0.0005 cm^{-1} to 0.004 cm^{-1}, doubling each time. The results are given in Fig. 5.3 for discrete and for continuous FRS frequency scanning methods.

As can be seen, the norm of the error decreases as the wavenumber scanning resolution increases. Because the numerical resolution of the simulation is 0.0001 cm^{-1}, a wavenumber scanning resolution of 0.0005 cm^{-1} sometimes already results in errors in the convolution part, since the numerical resolution needs to be considerably finer than the wavenum-

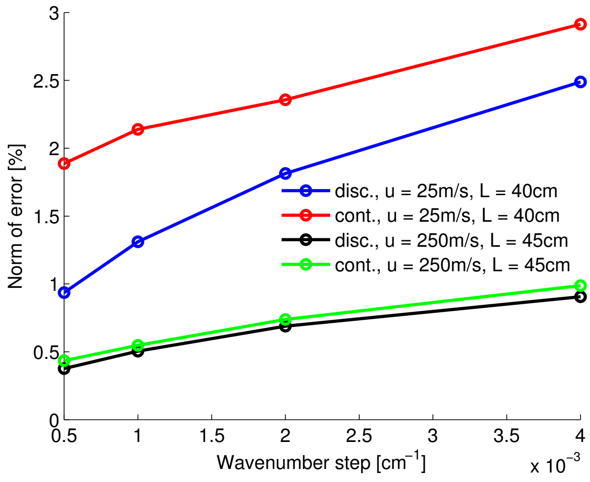

Figure 5.3: Accuracy vs. wavenumber scanning resolution

ber scanning resolution. So, to investigate even finer scanning resolutions, the simulation resolution must be increased. This is possible but not realistic, since the computing time increases dramatically, making it almost impossible to perform parameter studies even with a thousand Monte Carlo simulations. Besides, a technical implementation of higher scanning resolutions is not expected in the foreseeable future. With all things given, a wavenumber scanning resolution of 0.001 cm^{-1} has been chosen for all further studies. This is the finest scanning resolution that can be accurately utilized with a numerical resolution of 0.0001 cm^{-1} and for which a further increase in the numerical resolution has no significant impact. For continuous FSM-FRS techniques, the numerical resolution should be equivalent to the sampling interval of frequency scanning (in wavenumbers). So, the numerical resolution has some experimental importance as well. However, that's beyond the scope of this thesis. Fig. 5.3 also shows the accuracy differences between discrete and continuous FSM-FRS: continuous FSM-FRS performs worse than direct FSM-FRS, especially at low velocities. As the velocity increases, the difference in the norm of the error becomes smaller (also affected by the fact that the normalization factor for the relative error in velocity changes from 25 m/s to 250 m/s). It must be mentioned again that for the continuous frequency scanning FRS methods, the scanning resolution corresponds to the wavenumber integration interval.

5.3. Molecular Filter Optimization

The molecular filter is one of the most important components of any FRS experiment. This section reviews the filter optimization process and suggests possible improvements by using multiple filter cells together.

5.3.1. Absorption Well, Temperature, Length

As already mentioned before, an iodine filter transmission curve depends on filter temperature and length. Also, there are different absorption features that can be scanned by a green laser. These considered features (lines) are located at wavenumbers 18788.44 cm^{-1}, 18789.3 cm^{-1}, and 18789.5 cm^{-1} of the iodine transmission curve, shown in Fig. 4.7. For a given absorption feature, increasing the filter temperature or length lowers transmission,

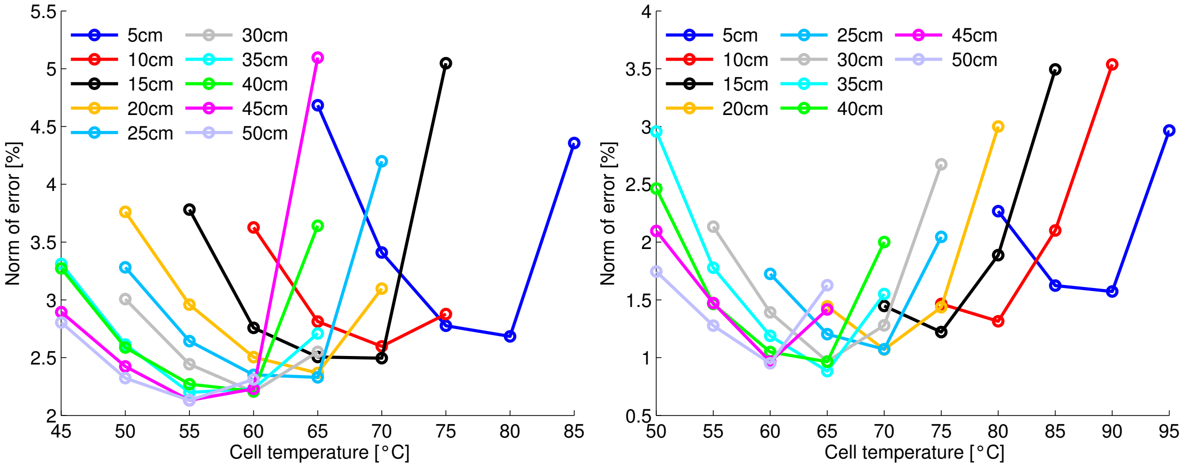

(a) $u = 25$ m/s (b) $u = 250$ m/s

Figure 5.4: Simulation results, absorption feature at 18788.44 cm^{-1}

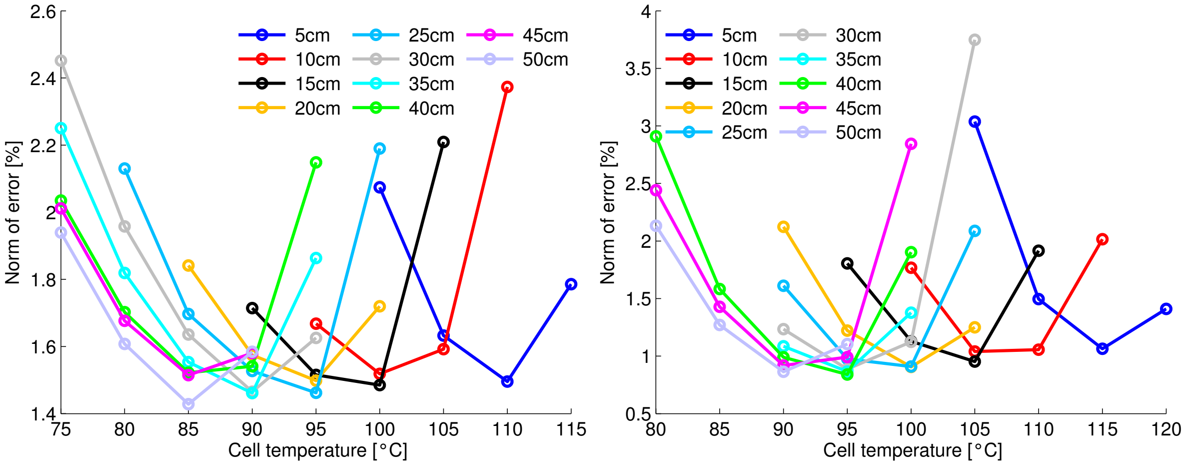

(a) $u = 25$ m/s (b) $u = 250$ m/s

Figure 5.5: Simulation results, absorption feature at 18789.3 cm^{-1}

but increases absorption feature linewidth and therefore the frequency scanning range. While the larger scanning range translates into a better accuracy, the lower transmission means higher shot noise relative to the signal. So, in fact there is a trade-off between filter transmission and absorption feature linewidth.

In order to determine the most appropriate absorption well and filter properties, temperature, length, and the absorption line must be investigated together. This has been done for given cruise conditions (temperature, pressure) and the two velocity cases $u = 25$ m/s and $u = 250$ m/s).

The obtained results are given in Fig. 5.4-5.6, each describing one absorption line. It can be noticed that for a given filter length, a norm of the uncertainty vs. cell temperature curve is U-shaped, indicating the presence of an optimum. When the temperature is too low, the transmission is high but the absorption feature linewidth is very small. So, there is a lot of signal but not enough frequencies. On the other hand, when the temperature is too high, the frequency scanning range is good enough but the intensity of the transmitted light is

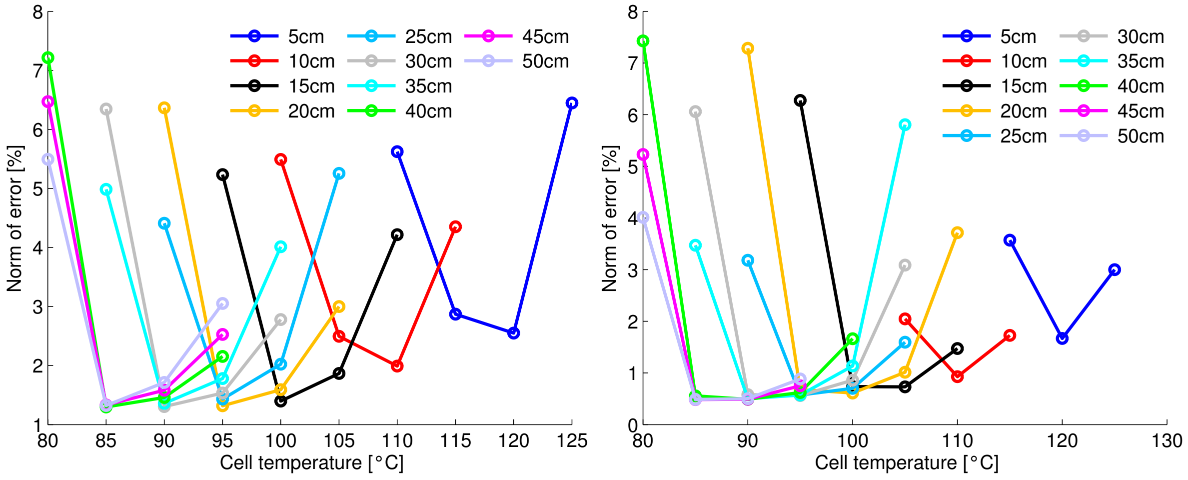

(a) $u = 25$ m/s (b) $u = 250$ m/s

Figure 5.6: Simulation results, absorption feature at 18789.5 cm^{-1}

Wavenumber (cm^{-1})	Length (cm)	Temperature (°C)	Error norm (%)
18788.44	45	55	2.14
18789.3	50	85	1.43
18788.5	40	85	1.30

Table 5.1: Optimized filter parameters for $u = 25$ m/s

Wavenumber (cm^{-1})	Length (cm)	Temperature (°C)	Error norm (%)
18788.44	35	65	0.89
18789.3	40	95	0.85
18788.5	45	85	0.49

Table 5.2: Optimized filter parameters for $u = 250$ m/s

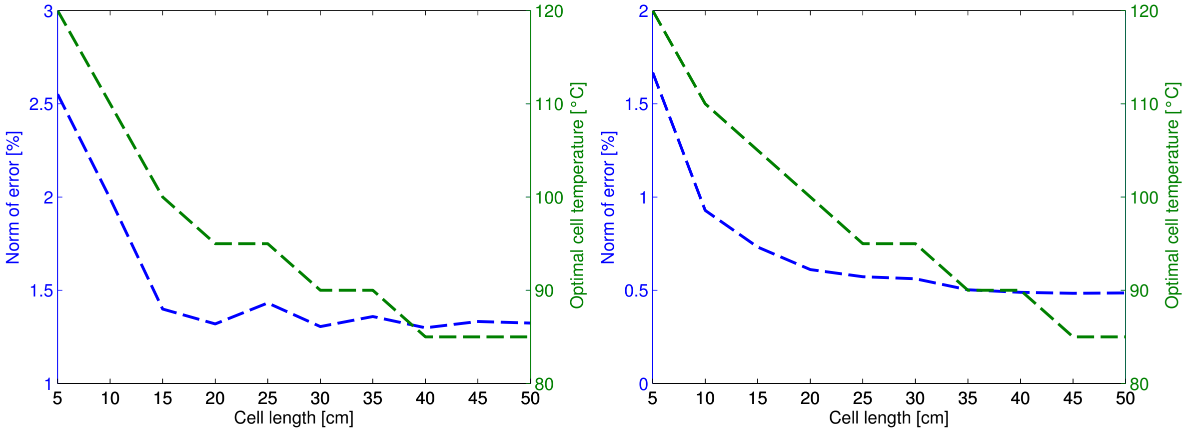

(a) $u = 25$ m/s (b) $u = 250$ m/s

Figure 5.7: Optimal temperatures and the corresponding uncertainties, 18979.5 cm^{-1}

very low and noisy (due to high relative shot noise). So, the optimum lies in between. As the filter length increases, the absorption well width increases and the transmission decreases. Therefore, the possible filter temperatures go down as well. One can see that as the filter length increases, the norm of the uncertainty decreases for the optimal cell temperature. This is true for all absorption lines and for the both velocity cases.

The optimized filter parameters for both velocities are summarized in tables 5.1 and 5.2 for all three absorption features: The filter absorption feature located at 18789.5 cm^{-1} offers the best accuracy for both velocity cases. So, the other absorption features can be dismissed. For u = 25 m/s, the best filter parameters are L = 40 cm and T_F = 85°C. For u = 250 m/s, the best filter parameters are L = 45 cm and T_F = 85°C. This difference is very logical, since the Doppler shift is higher for u = 250 m/s and therefore the frequency scanning range is shorter. So, it needs a slightly longer cell to compensate for this. For u = 25 m/s, there are already sufficient frequencies with L = 40 cm cell. Further increasing the cell length does not improve anything because the transmission decreases and the signal level drops down.

Fig. 5.7 show how the norm of the error changes with the cell length for the optimum cell temperature of the absorption feature at 18789.5 cm^{-1}. The error values are very similar for cells with lengths of 40, 45, and 50 cm. 1000 or 2000 simulations may not be sufficient to resolve these differences. However, there is another important factor that can be used for decision making. If the optimal cell temperature does not decreases after increasing the cell length, it means that the signal level drops down. If the uncertainty is also not reduced (within the Monte Carlo accuracy), then it can be concluded that the previous filter parameters were superior: a high signal level is very important for the signal-to-noise ratio, and one can not afford losing transmission without actually gaining anything in the accuracy. So, the optimized cell parameters are indeed L = 40 cm and L = 45 cm, at T_F = 85°C, for u = 25 m/s and u = 250 m/s, respectively.

5.3.2. Combined Signals

Until now, it was considered that collected Rayleigh scattered light goes through a single filter. In theory, it is possible to split the signal and pass it through different filters. This can be done, for example, by coupling the scattered light into two fibers and placing the fiber exists in front of the two different filters. With this, one obtains twice the information if both spectra are evaluated together. However, the signal level per branch is more than halved. Thus it is important to see if the filter combination improves the accuracy in the parameters.

So, for the optimal filter cell lengths (40-45 cm) and temperatures (80-100°C), combined spectra from two filters were used to determine the flow parameters. This was done for both velocity cases. Fig. 5.8 shows the obtained results. Here, for each curve, the temperature of one filter (T_{F_1}) and the cell lengths of the both filters (L_1, L_2) are fixed. The temperature of the second filter (T_{F_2}) is varied within the specified range. This is repeated for a number of T_{F_1}, L_1 and L_2 close to the optimal values identified in the previous section. It must be noted that the frequency scanning range is determined by the filter which has a narrower absorption feature: Since the laser frequency is same for both diagnostic units, it must be ensured that the central scattering frequency remains within the absorption well for both filters. This wastes some of the frequency scanning range in the filter that has a broader absorption feature. The results for the optimized case, as given in table 5.3, show no improvement over the single filter case. Moreover, it can be noticed that the optimized parameters for the both cells are the same and exactly match the ones from a single filter case. This finding further

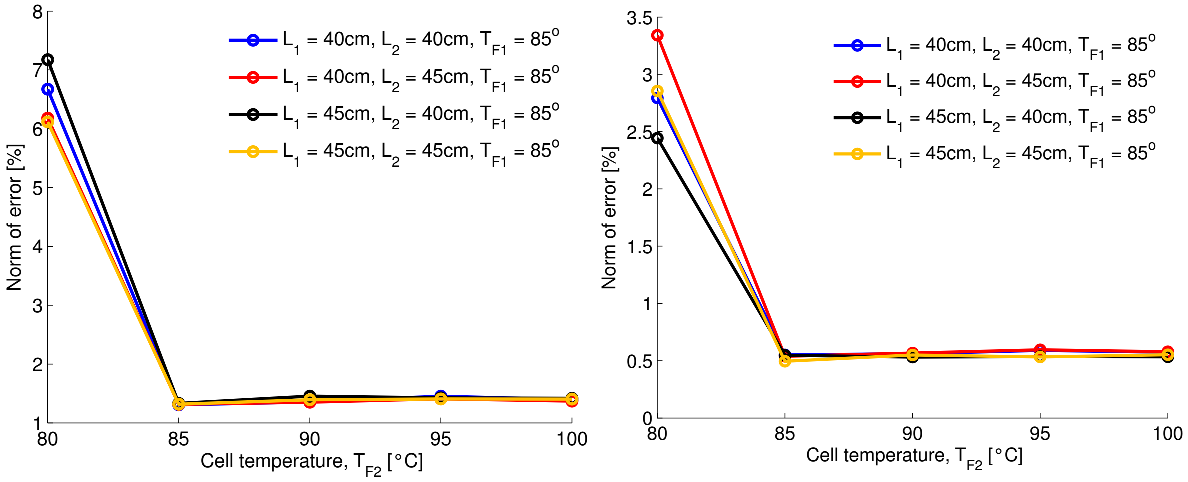

(a) $u = 25$ m/s

(b) $u = 250$ m/s

Figure 5.8: Simulation results for the combined filters, 18789.5 cm^{-1}

Velocity (m/s)	L_1, L_2 (cm)	T_{F_1}, T_{F_2} (°C)	Error norm (%)
25	40, 40	85, 85	1.31
250	45, 45	85, 85	0.50

Table 5.3: Optimized parameters for combined filters, 18789.5 cm^{-1}

stresses the fact that the optimized cell parameters are indeed $L = 40$ cm and $L = 45$ cm, at $T_F = 85$°C, for $u = 25$ m/s and $u = 250$ m/s, respectively. It seems that halving the signal, and wasting some of the frequency scanning range in one of the filters, counteracts the gains in the accuracy due to using two spectra combined. So, there is no point of making a much more complicated setup without any advantages. In practice, it may be possible to shutter one of the fibers during the time when laser frequency goes out of the absorption band of one of the filters. However, this would require additional control unit and electronics which is beyond the scope of OSIRIS project.

5.3.3. Signal Ratios

This idea of filter ratios originates from LIDAR research (Light Imaging, Detection, And Ranging) research. She (1997, 2007), Caldwell et al. (1996), and Hair et al. (2001) all proposed using multiple iodine cells and normalizing the transmitted Rayleigh scattering signals for determining atmospheric temperature and pressure profiles. They did not use frequency scanning FRS, but instead had a fixed incident laser frequency. However, a ratioed spectrum can also be used to determine flow parameters in FSM-FRS. This would remove any dependency on the scattered light power, turning the Eq. 3.17 into:

$$N_{PE}(\nu_c) = \frac{\int_{-\infty}^{+\infty} t_2(\nu) g\big(\theta, T, P, \nu - (\nu_c + \Delta\nu_D)\big) d\nu}{\int_{-\infty}^{+\infty} t_1(\nu) g\big(\theta, T, P, \nu - (\nu_c + \Delta\nu_D)\big) d\nu} \tag{5.3}$$

where $t_1(\nu)$, $t_2(\nu)$ are the transmission curves of filters 1 and 2. While the cancelling of the laser power circumvents the corresponding uncertainty, shot noise is severely amplified

Velocity (m/s)	L_1, L_2 (cm)	T_{F_1}, T_{F_2} (°C)	Error norm (%)
25	40, 40	80, 85	48.11
250	40, 40	80, 85	50.92
25	40, 45	80, 85	97.47
250	40, 45	80, 85	77.67

Table 5.4: Some of the results for the filter ratios, 18789.5 cm^{-1}

due to the detrimental error propagation in the division. Also, the signal level is half of the original one.

Table 5.4 presents results using the filter ratios. As one can see, using multiple filters in a ratioed scheme destroys any accuracy in the parameters. For some configurations, there are convergence problems when using the least-squares fitting as well. The dramatic uncertainty increase affects all parameters, especially pressure. In general, sensitivity towards the signal ratios is very low when using the filters whose absorption features have the same shape. For further studies, it would be advantageous to consider filters with relatively distinct absorption features.

5.4. Modulation Amplitude

For modulated FSM-FRS, two important parameters that come into play are the modulation frequency and amplitude. More specifically, by looking at Fig. 3.10, one can notice that with the modulation on top of the normal frequency scanning, the laser frequency periodically varies with an amplitude of $\pm a$ (modulation amplitude). At the beginning or end of the scan, this may cause the laser frequency to take on values which are outside of the desired filter transmission range. Therefore, the frequency scanning range has to be shortened. Also, there is a dependency between the magnitude of the derivative spectra and the modulation amplitude. Therefore, it is necessary to investigate this parameter.

Fig. 5.9 shows the dependency of the uncertainty on the modulation amplitude. This was calculated for both velocity cases with the optimized filter parameters. $1f$ detection

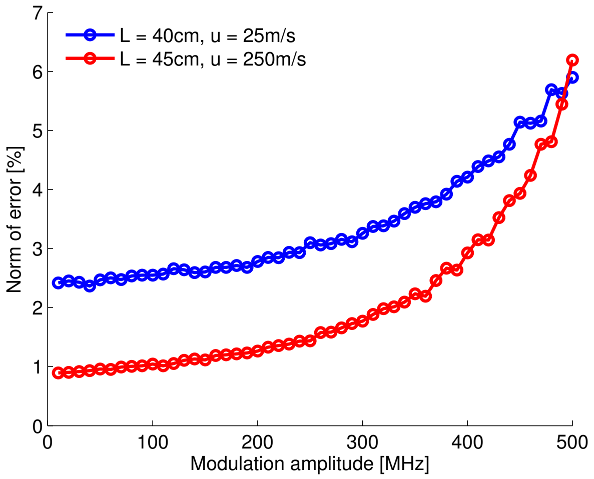

Figure 5.9: Modulation amplitude optimization

was used in the study. However, the results obtained here are also valid for $2f$ or $1f/2f$ detection schemes, because the impact of the modulation amplitude is similar. As one can see, the uncertainty in parameters increases as the modulation amplitude gets bigger. This is expected due to the reasons mentioned above. From this perspective, the modulation amplitude must be as low as possible. However, there are other more conceptual limitations as well.

Even though the laser is assumed to be monochromatic, as already mentioned before, it is spectrally broadened. The modulation amplitude must be significantly larger than the linewidth of the laser's spectral profile (Jagodzinski, 2007). For OSIRIS, the linewidths of the continuous-wave lasers can be assumed to be less than 5 MHz; the modulation amplitude has to be at least a magnitude higher. Jagodzinski (2007) uses a modulation amplitude of about 120 MHz in the experiments. This value is used here as well since it is also 20-30 times higher than the laser linewidth, and the uncertainty incurred is quite small.

The laser modulation frequency is also an important factor. The equations are independent of it, since the lock-in amplifier is synchronized with this frequency. So, this is a parameter that needs to be optimized experimentally. When deriving formulae for modulated FSM-FRS, it was assumed that the mean frequency of the laser during one modulation period remains constant. However, this is not the case since the laser frequency is simultaneously scanned from one end of the filter absorption feature to another. During the modulation period $T_m = 1/f_m$, the frequency change due to a slow scan (linear scan) across the filter absorption feature must be lower than the linewidth of the laser and much smaller than the modulation amplitude. For example, if the measurement rate is 1 Hz, the frequency scanning range is 1 GHz, and the modulation frequency is 1 kHz, then the laser frequency change during one modulation period is 1 MHz. If the modulation amplitude is 120 MHz and the laser linewidth is around 5 MHz, then it is valid to assume that the mean laser frequency is constant during one modulation period.

5.5. 1C Probe Results

Before moving to a 3C probe optimization, it is better to present the optimized results for a 1C probe and show the effects of using different FSM-FRS techniques. So, depending on the velocity component being measured, two different optimum filters parameters were found. For $u = 250$ m/s, the optimum filter length and temperature were 45 cm and 85°C. For $u = 25$ m/s, these values were 40 cm and 85°C, respectively. The filter absorption line at 18789.5 cm^{-1} was found to be the best. If using a modulated FSM-FRS, a modulation amplitude of 120 MHz is a good value to work with. So, for these optimized parameters and both velocity cases, the simulations were performed with $N_{MC} = 10000$. The results are given in tables 5.5-5.8. Here, both the statistical and systematic deviations are shown. For the systematic uncertainties, only the uncertainty incurred by assuming a small collection lens angle is included. The deviations due to neglecting the laser lineshape and the ash particle scattering are below the rounding precision of the presented results (< 1 Pa, < 0.01 K, < 0.01 m/s). More about these assumptions is discussed in section 4.2.1.

As it can be seen, the systematic uncertainties are mostly negligible (except $\Delta_\Omega P$) compared to the statistical uncertainties. Model assumptions are not expected to affect the statistical uncertainties significantly. They just shift the converged (average) parameters from their theoretical values. Temperature and velocity systematic uncertainties are a tiny fraction of the statistical uncertainties. However, pressure has higher uncertainties

Method	σ_P (Pa)	σ_T (K)	σ_u (m/s)	Norm (%)
Discrete	38	0.67	0.32	1.32
Continuous	44	0.68	0.53	2.15
Modulated, $1f$	239	1.80	0.58	2.61
Modulated, $2f$	86	0.47	0.60	2.43
Modulated, $1f/2f$	527	0.68	0.50	2.84

Table 5.5: Statistical errors for the optimized 1C probe, $u = 25$ m/s

Method	σ_P (Pa)	σ_T (K)	σ_u (m/s)	Norm (%)
Discrete	73	0.80	0.58	0.51
Continuous	80	0.79	0.74	0.55
Modulated, $1f$	214	1.53	0.55	1.08
Modulated, $2f$	106	1.04	0.98	0.73
Modulated, $1f/2f$	341	0.89	0.47	1.36

Table 5.6: Statistical errors for the optimized 1C probe, $u = 250$ m/s

Method	$\Delta_\Omega P$ (Pa)	$\Delta_\Omega T$ (K)	$\Delta_\Omega u$ (m/s)
Discrete	20	0.04	0.01
Continuous	21	0.04	0.01
Modulated, $1f$	21	0.04	0.01
Modulated, $2f$	19	0.03	0.01
Modulated, $1f/2f$	19	0.04	0.01

Table 5.7: Small lens angle error for the optimized 1C probe, $u = 25$ m/s

Method	$\Delta_\Omega P$ (Pa)	$\Delta_\Omega T$ (K)	$\Delta_\Omega u$ (m/s)
Discrete	24	0.08	0.08
Continuous	27	0.07	0.06
Modulated, $1f$	25	0.08	0.06
Modulated, $2f$	24	0.09	0.05
Modulated, $1f/2f$	16	0.11	0.07

Table 5.8: Small lens angle error for the optimized 1C probe, $u = 250$ m/s

regarding the small lens angle assumption. It is only for direct-detection FSM-FRS that the systematic uncertainty in the pressure must be taken into account. Otherwise, the statistical uncertainties are dominating.

Direct-detection FSM-FRS methods have a good accuracy in all parameters. Continuous FSM-FRS is less accurate than discrete FSM-FRS, especially in measuring the velocities. Differences in the accuracies of pressure and temperature are small. Modulated $1f$ FSM-FRS offers a good accuracy in velocity, but a relatively poor precision in temperature and pressure. The $2f$ signal, on the other hand, is more accurate in determining pressure and temperature and less accurate in measuring velocity. The ratio of the modulated signals, $1f/2f$, is precise

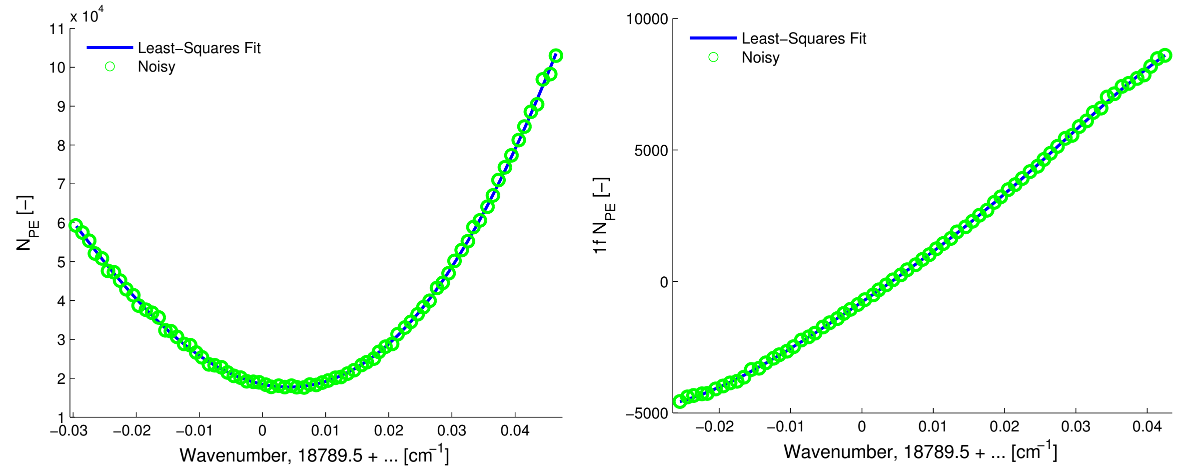

(a) Continuous FSM-FRS

(b) Modulated FSM-FRS, $1f$

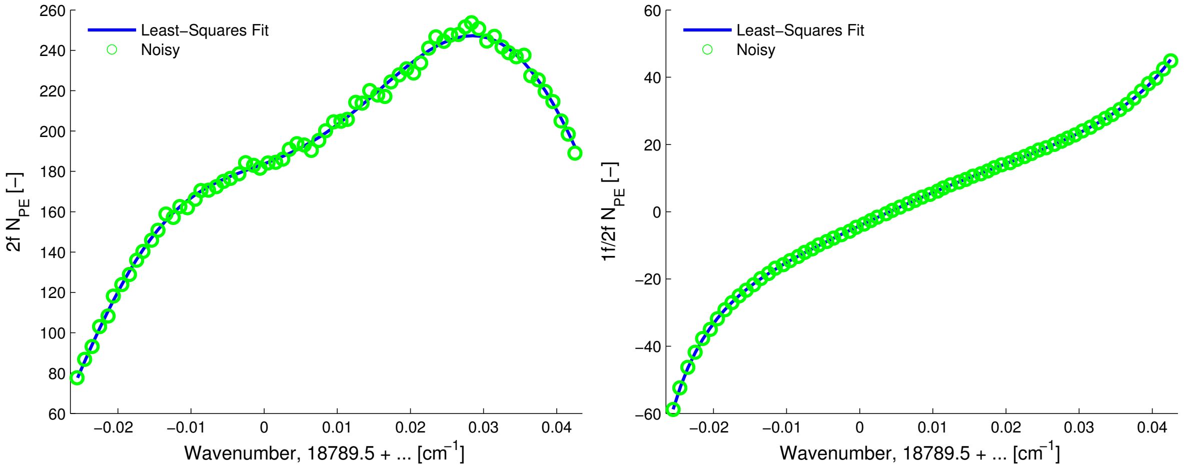

(c) Modulated FSM-FRS, $2f$

(d) Modulated FSM-FRS, $1f/2f$

Figure 5.10: Example simulation spectra for a 1C probe, $u = 25$ m/s

in measuring the velocity and temperature. However, the pressure uncertainty is highest for this technique, since pressure is directly related to the amplitude of the signal. Therefore, when the signal is normalized, as in $1f/2f$, a substantial part of pressure sensitivity is lost. It is not so simple to explain why these different modulated FSM-FRS techniques have distinctive sensitivities in the flow parameters. The governing equations are highly nonlinear and can only be assessed using the e2e simulator.

Fig. 5.10 shows an example simulation with the corresponding least-squares fit curve for each FSM-FRS technique. A discrete FSM-FRS plot is omitted since it is visually identical to a continuous FSM-FRS. For $u = 25$ m/s, a direct-detection FSM-FRS spectrum has a parabolic shape. So, the $1f$ signal looks like a straight line (derivative of the parabola). For a perfect parabola, the $2f$ function must be a horizontal line. Comparing the y-scale of $2f$ to continuous and $1f$ spectrum, the respective curve is close to a straight horizontal line. So, because the $2f$ signal varies less relative to $1f$ signal, the $1f/2f$ signal looks more similar to $1f$.

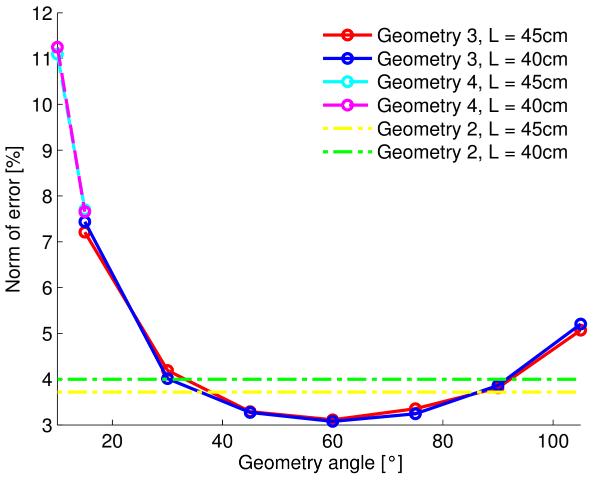

Figure 5.11: 3C probe geometry optimization

5.6. 3C Probe Geometry Optimization

In this section, 3C probes that can simultaneously measure all velocity components will be investigated. As already explained before in section 4.4, three different configurations have been conceived: geometry 2, 3, and 4. Geometries 3 and 4 have an additional parameter, angle α. To investigate the 3C probe and determine the most accurate method and configurations, all geometries have to be evaluated with both sets of filter parameters (temperature and length), that were optimized for the 1C probe. Geometry 2 has no dependency on the angle since the laser beams are orthogonal to each other and parallel to the velocity components. For geometry 3, the angle α was varied from 15° to 105° in steps of 15°. For geometry 4, two α values were tried, 10° and 15°. At all times, the filter temperature was 85°C. The obtained results for different filter lengths and angular configurations are depicted in Fig. 5.11. The direct-detection continuous frequency scanning method has been used. The main goal behind the geometry optimization is to extend the frequency scanning range without sacrificing the sensitivity in the velocity components. This is independent of the FSM-FRS technique used.

For a geometry 2, it is better to use a filter with $L = 45$ cm. This is expected, since all velocity components are aligned with the emitter/receiver units. So, the highest velocity component measured is 250 m/s. This generates a relatively high Doppler shift and requires longer filter cell to extend the frequency scanning range. For the same reasons as a 1C probe aligned with a 250 m/s velocity component, geometry 2 performs best with a filter cell of length 45 cm and temperature 85°C.

Geometry 3 is a more complicated configuration. It can be seen that the optimal value for angle α is 60°. This is exactly in between the whole investigated dynamic range, 0° and 120°. With this angle, the three emitter/receiver units form a tetrahedron. So, it can be concluded that this configuration provides the best trade-off between the sensitivity in the velocity components and the Doppler shift magnitude. The whole idea of geometry 3 is to decrease the Doppler shift perceived by the receivers and increase the frequency scanning range. Therefore, the shorter filter performs better. When α is close to its limits, the configuration with a longer cell becomes more accurate because the maximum observed Doppler shift increases. To summarize, geometry 3 has the highest accuracy when $\alpha = 60°$, $L = 40$ cm, and $T_F = 85°$C.

According to Fig. 5.11, performance of the geometry 4 is strongly limited by the allowable angle α. As α increases, the norm of the uncertainty decreases. However, due to the window size, the absolute limit is $\alpha = 15°$. For $\alpha = 15°$, the configuration with a shorter filter of length 40 cm and temperature 85°C offers a slightly better accuracy. For geometries 3 and 4 (except the beam orthogonal to the window), focal lengths and diameters of the collection lenses change with α in order to keep $f_\# = 10$.

5.7. 3C Probe Results

After performing a 3C probe optimization with a direct-detection method, the optimized angles and parameters will be employed for all FSM-FRS methods. Both, the statistical and systematic errors are given in tables 5.9-5.14. The systematic uncertainties are again represented by small lens angle assumption because the other model simplifications are irrelevant. Similar to the 1C probe, 10000 Monte Carlo simulations were used for each case.

Systematic uncertainties are again negligible compared to the statistical uncertainties, with the exception of geometry 4. For the geometries 2 and 3, the statistical uncertainties in all parameters are much larger than the systematic uncertainties due to a small lens angle assumption. It is only the direct-detection FSM-FRS where the systematic uncertainty in

Method	σ_P (Pa)	σ_T (K)	σ_u (m/s)	σ_v (m/s)	σ_w (m/s)	Norm (%)
Discrete	62	0.53	0.61	0.53	0.53	3.03
Continuous	72	0.56	0.78	0.66	0.66	3.76
Modulated, $1f$	164	1.21	0.56	0.58	0.57	3.36
Modulated, $2f$	82	0.54	0.62	1.11	1.11	6.30
Modulated, $1f/2f$	348	0.69	0.50	0.56	0.56	3.45

Table 5.9: Statistical errors for the optimized 3C probe, geometry 2

Method	σ_P (Pa)	σ_T (K)	σ_u (m/s)	σ_v (m/s)	σ_w (m/s)	Norm (%)
Discrete	59	0.60	0.94	0.29	0.51	2.40
Continuous	70	0.64	1.00	0.59	0.52	3.19
Modulated, $1f$	176	1.35	0.53	0.62	0.29	2.89
Modulated, $2f$	82	0.57	1.35	0.91	1.75	7.92
Modulated, $1f/2f$	355	0.68	0.36	0.55	0.15	2.67

Table 5.10: Statistical errors for the optimized 3C probe, geometry 3

Method	σ_P (Pa)	σ_T (K)	σ_u (m/s)	σ_v (m/s)	σ_w (m/s)	Norm (%)
Discrete	22	0.37	1.85	0.17	1.85	7.47
Continuous	33	0.40	1.86	0.45	1.84	7.62
Modulated, $1f$	125	0.97	1.33	0.48	1.30	5.61
Modulated, $2f$	44	0.26	3.09	0.50	3.27	13.30
Modulated, $1f/2f$	394	0.44	0.78	0.45	0.66	3.54

Table 5.11: Statistical errors for the optimized 3C probe, geometry 4

Method	$\Delta_\Omega P$ (Pa)	$\Delta_\Omega T$ (K)	$\Delta_\Omega u$ (m/s)	$\Delta_\Omega v$ (m/s)	$\Delta_\Omega w$ (m/s)
Discrete	24	0.05	0.07	0.03	0.03
Continuous	24	0.05	0.06	0.04	0.04
Modulated, $1f$	21	0.04	0.06	0.01	0.01
Modulated, $2f$	21	0.05	0.09	0.02	0.02
Modulated, $1f/2f$	16	0.07	0.07	0.03	0.03

Table 5.12: Small lens angle error for the optimized 3C probe, geometry 2

Method	$\Delta_\Omega P$ (Pa)	$\Delta_\Omega T$ (K)	$\Delta_\Omega u$ (m/s)	$\Delta_\Omega v$ (m/s)	$\Delta_\Omega w$ (m/s)
Discrete	21	0.05	0.09	0.02	0.02
Continuous	21	0.05	0.08	0.01	0.01
Modulated, $1f$	20	0.04	0.08	0.01	0.01
Modulated, $2f$	20	0.04	0.08	0.01	0.01
Modulated, $1f/2f$	18	0.04	0.07	0.01	0.01

Table 5.13: Small lens angle error for the optimized 3C probe, geometry 3

Method	$\Delta_\Omega P$ (Pa)	$\Delta_\Omega T$ (K)	$\Delta_\Omega u$ (m/s)	$\Delta_\Omega v$ (m/s)	$\Delta_\Omega w$ (m/s)
Discrete	17	0.03	0.43	0.01	0.09
Continuous	17	0.03	0.33	0.01	0.07
Modulated, $1f$	18	0.03	0.32	0.01	0.03
Modulated, $2f$	17	0.03	0.28	0.01	0.07
Modulated, $1f/2f$	20	0.03	0.35	0.01	0.06

Table 5.14: Small lens angle error for the optimized 3C probe, geometry 4

pressure is slightly more important because the statistical uncertainty in pressure is very low. For geometry 4, along with the pressure, the systematic uncertainty in the u-component of the velocity is significant too. This is due to the fact that because of the limited window size and therefore small angles between the receiver units, sensitivity in the u-component of the velocity is not good enough.

As with the 1C probe, for all geometries, direct-detection FSM-FRS methods are accurate in all parameters. The discrete scanning method is slightly more accurate than the continuous one. Modulated $1f$ FSM-FRS has a very low uncertainty in velocities, but relatively high uncertainties in pressure and temperature. Modulated $2f$ FSM-FRS, on the other hand, is more accurate in determining the thermodynamic parameters but has a poor precision in velocities. The $1f/2f$ signal, which is independent of the scattered light intensity, has superior accuracy in the velocity components. The uncertainty in the temperature is quite low as well. However, the uncertainty in pressure is highest. In general, geometry 3 appears to be the best configuration. This was expected, judging by Fig. 5.11, where the norm of the uncertainty (error) was lowest for this geometry. Geometry 2 is the second best option. Geometry 4 is the least accurate because of the limited window size and the resulting small angle between the receiver units. It would be more accurate if these limitations are removed. However, the pressure and temperature uncertainties are very low for this geometry because five observation directions are used (in difference with three spectra from geometries 2 and 3). The best technique is $1f/2f$ if the pressure uncertainty is not very important. However, if measuring the pressure is crucial, then the direct-detection discrete FSM-FRS is the best choice.

Table 5.15, Fig. 5.12 and 5.13 show the simulation results for the optimized probe of geometry 3. Here, direct-detection discrete and modulated $1f/2f$ FSM-FRS signals, or N_{PE} and ${N_{PE}}^R$, are given. For the discrete FSM-FRS, all flow parameters are quite accurate but still outside of the desired precision ranges. With the $1f/2f$ signal the accuracies in the

Method	P (Pa)	T (K)	u (m/s)	v (m/s)	w (m/s)
Discrete	26501 ± 59	225.00 ± 0.61	250.00 ± 0.94	25.00 ± 0.30	25.01 ± 0.51
$1f/2f$	26614 ± 362	224.92 ± 0.67	249.98 ± 0.35	24.99 ± 0.55	24.99 ± 0.15

Table 5.15: Converged parameters, geometry 3, $\alpha = 60°$

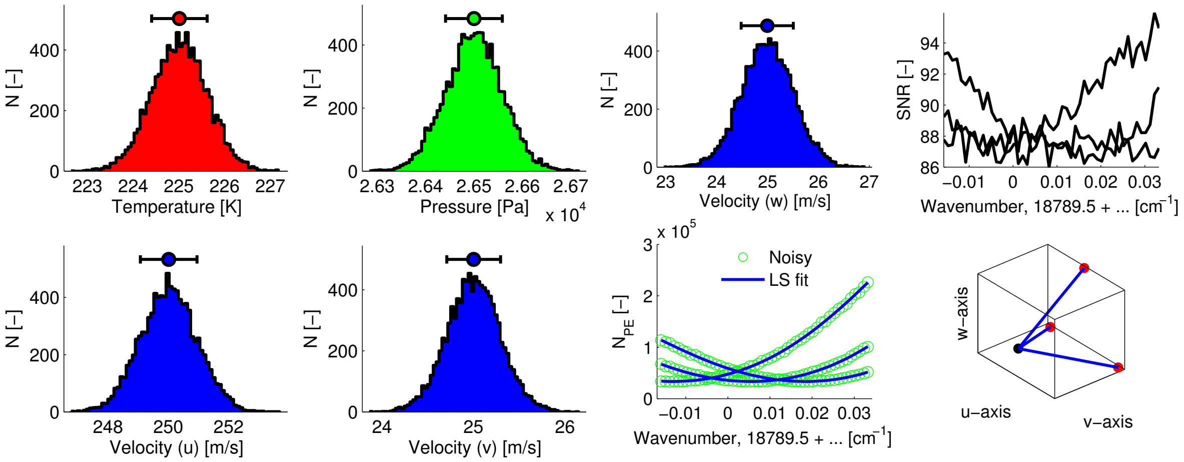

Figure 5.12: Simulation results, geometry 3, $\alpha = 60°$, discrete FSM-FRS

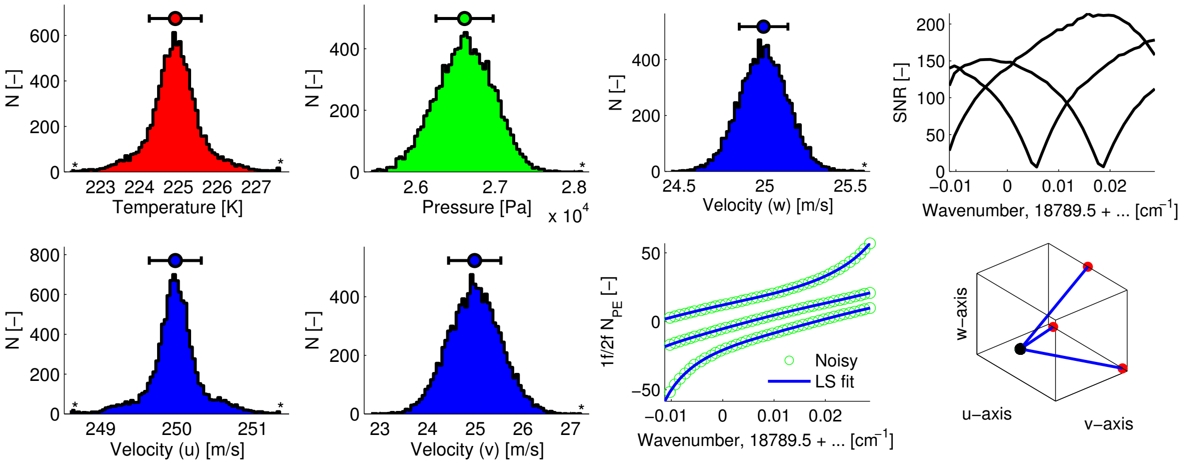

Figure 5.13: Simulation results, geometry 3, $\alpha = 60°$, $1f/2f$ FSM-FRS

parameters, especially in the velocity components, are remarkable. It is only the pressure that is inaccurate. That's why the average value does not converge to the actual pressure (26500 Pa) after 10000 simulations. All other parameters are converged. This happens because the $1f/2f$ signal is much less sensitive towards the pressure. It would require more simulations for the pressure to close in on the expected value.

Fig. 5.12 and 5.13 show a typical output of the e2e simulator. Along with the output parameter distributions, an example simulation spectrum and a geometric configuration of a probe are given as well. As already mentioned, since there are three different emitter/receiver units, the three spectra are combined and used in a least-squares fitting. The plot shows the simulated spectra with noise and the corresponding fitted curves. A definition of the signal-to-noise ratio, as given in section 4.2.2, is only useful for the variables that are always non-negative, such as a photon count or a number of photoelectrons. Therefore, it does not make sense to look at the signal-to-noise ratio plot in the case of a modulated FSM-FRS. So, the corresponding SNR graph in Fig. 5.13 must be neglected.

Decisive factor for the uncertainties is the frequency scanning range which is limited by the highest net Doppler shift occurring among the velocity components. So, if the forward velocity component (set to 250 m/s in this thesis) decreases, then the frequency scanning range will increase, resulting in lower parameter uncertainties.

6

Validation

No matter how good the simulations are, it is always necessary to validate them and the contained numerical models. Otherwise, the end-to-end simulator can not be used reliably in the actual design or optimization process. Due to the variety of investigated FSM-FRS models, it is not possible to perform validation experiments for all of them. Also, the construction of 3C probes exceeds the scope of this thesis, this is something for the future. However, what can be done is the validation experiment for the established direct-detection discrete FSM-FRS with a single emitter and receiver. This method was the foundation, on which the other approaches were implemented numerically.

6.1. Experimental Setup & Procedure

The experimental setup is given in Fig. 6.1 and 6.2. Experiments were conducted in the laboratory at the DLR Institute of Propulsion Technology. A diode pumped solid state laser, Coherent Verdi V5, produces a beam that is coupled into a polarization preserving single-mode photonic crystal fiber (PCF). This fiber guides the laser towards an optical table. When the laser beam exits the fiber, it passes through a half-wave plate which can be used to rotate the polarization vector of the laser and maximize the intensity of Rayleigh scattered light. Afterwards, the beam passes through a birefringent crystal which splits the beam into two parts that have different polarization directions. The original laser light is linearly polarized with 100:1 polarization ratio. So, more than 99% of the laser is linearly polarized. However, once it passes through the photonic crystal fiber, its polarization ratio drops significantly, also the polarization vector becomes unstable in rotation and ratio. Changes in polarization must be avoided for the FRS experiment because the differential scattering cross section strongly depends on it. So, by using the birefringent crystal, the polarization ratio of the beam significantly increases. Afterwards, the beam passes through a combination of two lenses and a pinhole to get rid of the light fraction transferred through the fiber's mantle and have a more or less Gaussian intensity distribution. Then the beam is directed towards a quartz plate using a mirror. The quartz plate reflects around 4% of the beam towards the measurement volume, where the intensity of the reflected light also depends on the polarization direction.

Once the light is reflected from the quartz plate, it goes through a lens and is focused. Scattered light from the beam waist is collected at $\theta = 90^\circ$, filtered, and directed towards the CCD camera using a combination of lenses. After passing the observed focus, the laser

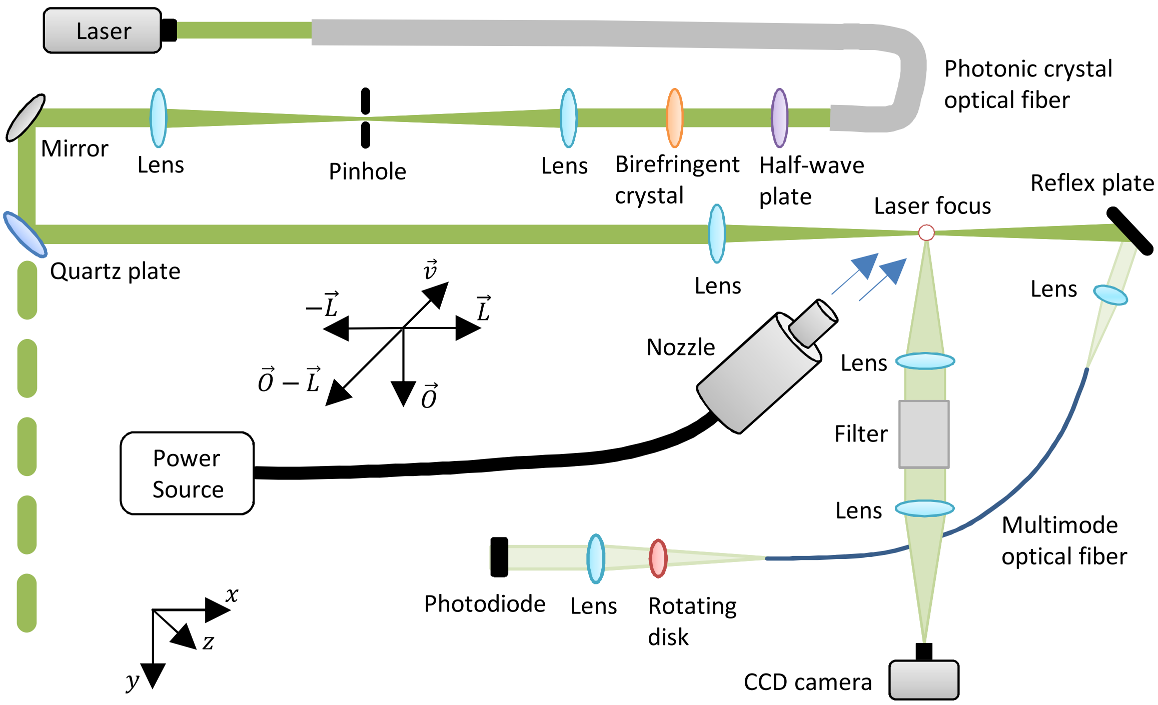

Figure 6.1: Schematic setup of the experiment

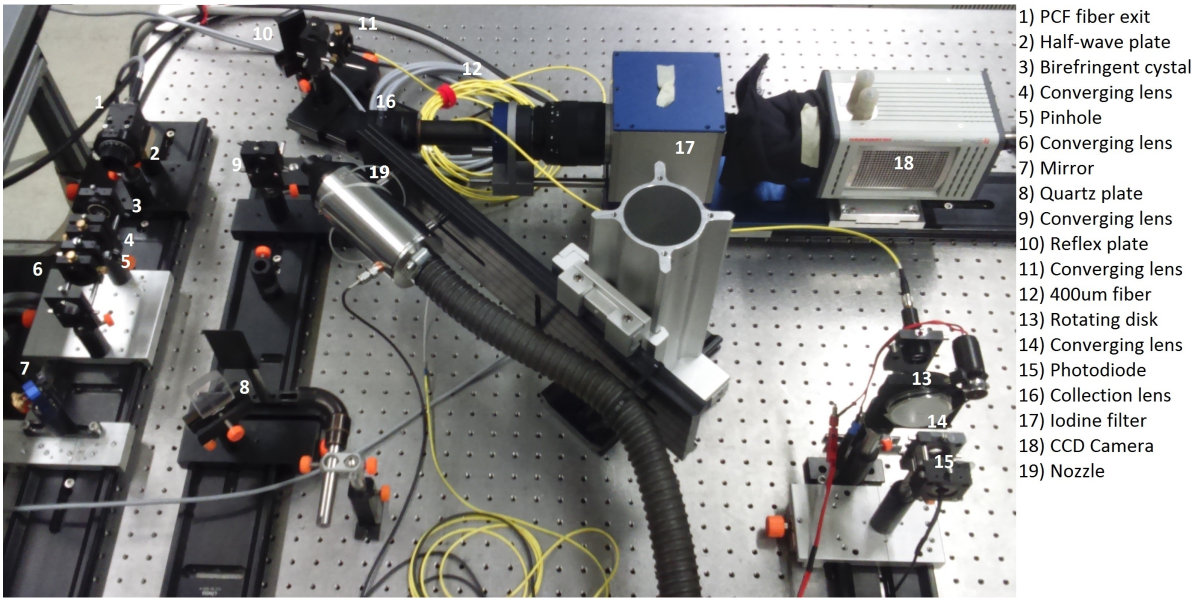

Figure 6.2: Experimental setup

beam illuminates an anodized metal plate, producing a diffusely scattering light spot. The reflected light is collected by a lens and coupled into a 400 μm fiber. After the fiber exit, there is a rotating diffusion disk that averages out the laser speckle. The light that passes through the rotating disk is collected by a lens and directed onto a photodiode. The resulting signal is used to normalize the laser power and account for power drifts and changes in the transmission of the PCF. This setup enables the laser power to be measured with an accuracy below 1%.

Environmental conditions are atmospheric. A flow is generated using a nozzle, which isentropically accelerates air that is supplied by a fan. The result is a conical potential core flow that extends 5 nozzle diameters downstream. Within this core, velocity and temperature of the air can be assumed constant and calculated using the isentropic relations. These depend on the nozzle geometry, settling chamber pressure and temperature as well as the ambient pressure. The pressure in the potential core can be assumed to be atmospheric. The core velocity can be varied by altering the fan's rotational speed. As one can see from Fig. 6.1, the nozzle is positioned at 45° to the observation and laser propagation directions. This is exactly along the vector $(\hat{O}-\hat{L})$, so the actual core velocity can be measured with maximum sensitivity (to be more specific, it is antiparallel to $(\hat{O}-\hat{L})$, but this does not change the sensitivity, simply the Doppler shift becomes negative).

The laser system specifications are the same as mentioned in section 4.6, table 4.1. An iodine filter cell with $L = 5$ cm and $T_F = 70°$C is used. For this filter, only the absorption feature located at a wavenumber 18788.44 cm^{-1} is used for frequency scanning. The reason is that the transmission for the other absorption wells is not low enough and does not satisfy the criterion of being less than 10^{-5}. The frequency of the laser is discretely scanned using the LabVIEW software. By controlling the piezoelectric actuators, the laser resonator can be squeezed, which in turn changes the lasing frequency. Using a wavemeter signal (laser frequency measurement) as a feedback, the laser can be stabilized to the specific frequencies in a control loop. Frequency scanning range and discrete frequencies to be scanned were chosen in order to cover the whole usable filter absorption feature. The experimental setup parameters are given in table 6.1.

Even though the laser system was operating at 2 W power, only the part of the beam reflected from by quartz plate was used for the measurements. The actual laser power in the focus was measured using a laser power meter and was found to be 40 mW. Frequency scanning FRS measurements were performed for multiple flow cases at ambient conditions. For each flow case, three consecutive scans were performed and the obtained spectra were averaged to further increase the signal-noise-ratio. For each case, the thermodynamic parameters (pressure and temperature) were measured before and after the measurements using static sensors and then averaged. Since there was no temporal restriction for the scans and the laser power was relatively low inside the focus, a collection time of 5 s was

Variable	Unit
Laser power	40 mW
Beam diameter	≈ 700 μm
Collection lens f	154 mm
Collection lens D	41.7 mm
Collection lens $f_\#$	3.7
Optical efficiency	≈ 90%
Quantum efficiency	≈ 90%
Filter temperature	70°C
Filter length	5 cm
Collection time	5 s

Table 6.1: Experimental setup parameters

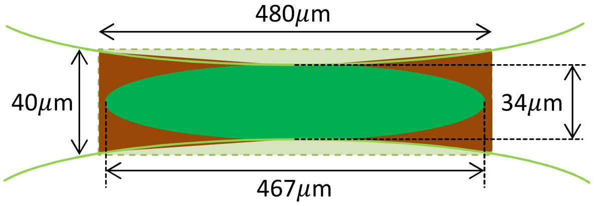

Figure 6.3: Confocal volume and the corresponding CCD pixel area

used. So, once the laser was stabilized at a given frequency, the scattered light was collected using a CCD camera for the duration of 5 seconds. According to the specifications, quantum efficiency of the used CCD camera was approximately 90%. The optical efficiency of the light collection system could not be determined exactly, but it is realistic to say that it was around 90%. So, the total efficiency (optical & quantum) was set to 81% in the simulations.

A CCD camera takes a 2D image and records pixel-wise grayscale intensity values (counts). In order to identify and record the intensity from a focal spot, the confocal volume for the given optical system was calculated based on section 3.2. Then, the beam waist on the CCD image as well as the pixel area corresponding to the confocal volume were defined. The intensity counts from pixel elements within this area were summed up. This provides a measure of the light intensity scattered from the confocal volume. Focal depth of the CCD camera is longer than the focused beam waist, so it can be assumed that the CCD collects all the light from the confocal volume along its optical axis.

The confocal volume and the corresponding CCD pixel area are visualized in Fig. 6.3. As one can see, the CCD pixel area used for the intensity summation is larger than the confocal ellipse. Since the pixel elements are discrete and square shaped, it is not feasible to match the areas (volumes) and only choose the pixel elements that are within the ellipse. The CCD image has a resolution of 512 × 512 pixels, where the edge of each pixel corresponds to 20 μm in the focal plane. The length of the major and minor axis of the confocal ellipsoid are approximately 467 μ and 34 μm. So, the CCD area corresponding to the confocal volume has a length of 24 pixels (480 μm) and a height of 2 pixels (34 μm). This is as close as one can get to the actual confocal volume with this CCD camera. It means that the light scattered outside of the confocal ellipse but within the chosen rectangular pixel area is still collected.

For all experimental cases, the theoretical (actual) parameters calculated or measured using the temperature and pressure sensors are given in table 6.2. T_s and P_s are the measured temperature and pressure in the settling chamber, T_r and P_r are the measured room temperature and pressure, and T_c is a temperature within the core flow calculated using the isentropic relations. The nozzle velocity, u_N, is also isentropically calculated for the core of the flow. Pressure within the core flow is same as the room pressure.

6.2. Post-processing

A goal of the FRS experiment is to determine the flow properties. However, they need to be inferred indirectly from the frequency scanning spectrum. This is done using a Levenberg-Marquardt least-squares fitting algorithm. However, to fit pressure, temperature, and the Doppler velocity values, all the other experimental parameters must be known. These include: scattering cross section, laser intensity, measurement volume, lens angle, optical and quantum efficiencies. It is often impossible to know or calculate them for a given experiment. Therefore, a calibration must be performed. For that reason, the Eq. 3.17 is transformed into:

$$N_{PE}(\nu_c) = R_F \frac{P}{T} \int_{-\infty}^{+\infty} t(\nu) g\big(\theta, T, P, \nu - (\nu_c + \Delta\nu_D)\big) \mathrm{d}\nu \tag{6.1}$$

with R_F being a calibration parameter which can be inferred from a reference measurement under known flow conditions. The number of photoelectrons, created in the Hamamatsu CCD camera used in the experiment, is simply 370000/65536 multiplied by the total intensity counts from the chosen rectangular (focal) pixel area. In principle, the factor R_F is a function of frequency, $R_F = R_F(\nu_c)$. However, the changes in the laser intensity, measurement volume, and the scattering cross section included in the factor R_F are negligible over the whole frequency scanning range (GHz range). Therefore, it is a valid assumption to have a constant R_F value for all frequencies. So, for fitting the flow parameters, only the scattering angle and R_F factor need to be known along with a FSM-FRS spectrum, filter transmission and Rayleigh-Brillouin lineshape model functions.

Before the actual measurement under flow conditions, a reference FSM-FRS measurement is performed to determine the R_F factor. With zero flow velocity and at the known atmospheric conditions (determined using temperature and pressure sensors), three FSM-FRS spectra are obtained and averaged. All the parameters and functions from Eq. 6.1 are known except the R_F factor. So, this forms an overdetermined system of equations with one unknown and many equations (depends on a number of discrete frequencies scanned) which can be solved using a least-squares approach.

As filter transmission function, a measured and interpolated curve is used. It is crucial for the fitting algorithm to have the actual transmission function of the filter used in an experiment. The Forkey (1996) iodine transmission model utilized in the e2e simulator is sufficient for relative parameter studies. However, it can not model the exact transmission of a given filter. First of all, not all electronic transitions are included in the model. Secondly, each filter cell is distinct and has some individual characteristics. So, a measured filter transmission function, was used in the data evaluation.

The e2e simulator uses the Tenti S6 model to determine the Rayleigh-Brillouin scattering profiles. Even though the Tenti S6 is very accurate and regarded in the literature as the best suited all-round model, it is not exact. For example, there are deviations from the actual scattering profiles at atmospheric conditions with moderate Y values. This is also the case for given experimental conditions. However, there is an alternative. Doll (2016) developed an analytical model for calculating Rayleigh-Brillouin scattering profiles and calibrated it for a certain Y-region ($0.68 \leq Y \leq 1.17$, which for air includes atmospheric and close to atmospheric conditions). This model is more accurate at these conditions but can not be generalized because it it is only valid in the calibrated Y-region. Therefore, it can not replace the Tenti S6 in the simulator because the conditions simulated are not necessarily within the calibrated interval (e.g. cruise conditions for the project OSIRIS with $Y \approx 0.4$). However, this analytical model can be used in the post-processing part of the experiment.

With all necessary parameters known, temperature, pressure, and Doppler velocity (T, P, and u_D) of the flow can be fitted. The laser propagation direction is $\hat{L} = (1, 0, 0)$. The observation direction is perpendicular to it, with $\hat{O} = (0, 1, 0)$. Thus the Doppler velocity directional vector is $(\hat{O} - \hat{L}) = (-1, 1, 0)$. Due to the nozzle geometry and a 45° alignment, the velocity vector in the coordinate system of the experiment is given by $\hat{v} = (u, -u, 0)$.

$$u_D = (\hat{O} - \hat{L}) \cdot \hat{v} = -2u \tag{6.2}$$

The nozzle velocity, u_N, equal to the magnitude of the velocity vector, can be found using:

$$u_N = \frac{-u_D}{\sqrt{2}} \tag{6.3}$$

6.3. Results & Comparison

Using the e2e simulator, simulations have been performed with the same parameters as in the experiment with $N_{MC} = 10000$. The confocal volume, in this case, included four additional triangular regions (brown color), as depicted in Fig. 6.3. First of all, these regions are very close to the laser's waist, so laser intensity is almost same. Secondly, it allows to perform the simulations where the confocal volume, from which the scattered light is collected, is as close as possible to the actual interrogation volume used in the experiment. Even though the confocal volume was adjusted for the simulations, it is still not possible to match it exactly with the interrogation volume corresponding to the chosen CCD pixel area. The rectangular area of the CCD image used in the experiment is still larger (compared to the ellipse plus four triangles) and collects more light. One can't use this rectangular area and the corresponding volume in the simulations because the laser intensity outside of the confocal ellipsoid is unknown.

The main purpose of the experiment is to validate the signal level for a direct-detection discrete FSM-FRS. If signal amplitude (number of photoelectrons) and shape are the same as estimated by the simulations, the end-to-end simulator is presumed to make reasonable predictions. Since the other FSM-FRS approaches (continuous scanning, modulated) are derived from a discrete FSM-FRS, they are validated to some extent as well. The number of photoelectrons as a function of the scanning frequency $N_{PE}(\nu_c)$ is a curve that determines parameter accuracies, since the relative shot noise depends on the signal level. If the simulated and measured FSM-FRS signals match, it can be assumed that the signal-to-noise ratios are equivalent because the other noise sources (laser power and frequency) are independent of the signal level.

To create comparable data, the average spectra of three FSM-FRS simulations for each flow case were plotted together with the experimentally obtained values. These are given in Fig. 6.4-6.7. Small circles correspond to the simulated or measured spectrum. The lines that pass through these circles are the fitted curves. The quality of the fit is given by the residual plot. The residual is the remaining deviation between experimental data and the fitted curve. It is related to the noise in the experiment and tells something about the signal-to-noise ratio. Based on the figures, one can see how close experimental FSM-FRS curves are to simulated spectra. The spectral shapes are visually the same for all flow cases.

The experimental FSM-FRS spectra show slightly higher photon counts than the simulated ones. This fixed factor in $N_{PE}(\nu_c)$ can be caused by many reasons. First of all, as already discussed before, there is more light collected in the experiment because of the discrete nature of CCD images, while the confocal volume used in the simulations is slightly smaller. Secondly, 90% quantum and optical efficiencies were the values used in the simulations. The actual quantum efficiency of the camera should be very close to that number, but the optical efficiency may not. It could have been slightly higher. At the end, these two factors (larger interrogation volume and a rough estimate for the optical efficiency) could definitely cause a small difference in the signal levels.

Based on the residual plots, it can be noticed that the noise level in the experiment is lower than in the simulations. This is expected due to the power normalization: in the

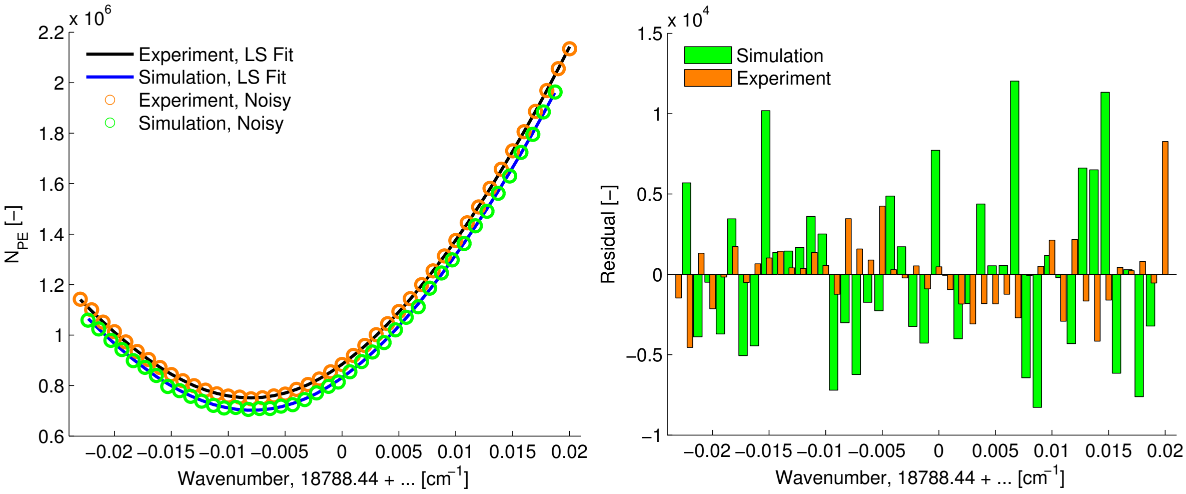

(a) Experiment & simulation spectra (b) Experiment & simulation LS residuals

Figure 6.4: Validation experiment results, case 1

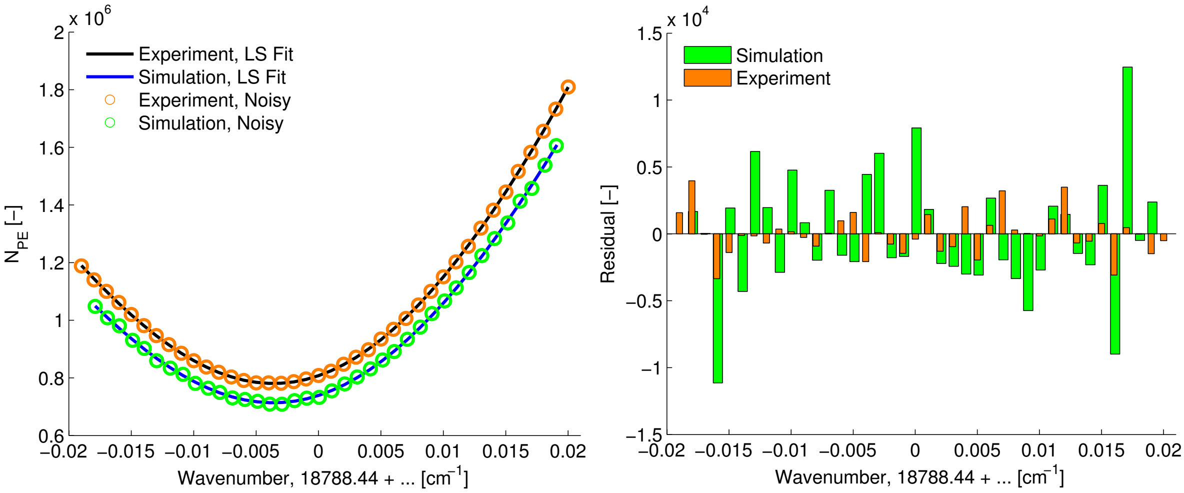

(a) Experiment & simulation spectra (b) Experiment & simulation LS residuals

Figure 6.5: Validation experiment results, case 2

simulations, 1% laser power drift is assumed. This is an uncertainty range provided by the laser manufacturer. However, in the experiment, a photodiode is used to normalize the laser power and account for the power drifts. So, the effective uncertainty in the laser power is the uncertainty in the photodiode signal which is surely less than 1%.

Tables 6.3-6.5 show experimental and simulation results. Simulation statistics are depicted in Fig. 6.8. By comparing tables 6.5 and 6.2, one can conclude that the parameters are almost converged to the mean (theoretical) values. Systematic deviations due to small lens angle assumption introduce considerable uncertainties, especially in pressure. As one can see from tables 6.5 and 6.4, the systematic uncertainty in pressure is larger than its statistical uncertainty. The uncertainties in the velocities are not negligible, but lower compared to the statistical uncertainties. The systematic uncertainty in temperature is negligible.

Measured velocity values are in good agreement with simulation results. For cases 1, 3 and 4, the difference between measured and isentropically calculated velocities is within the

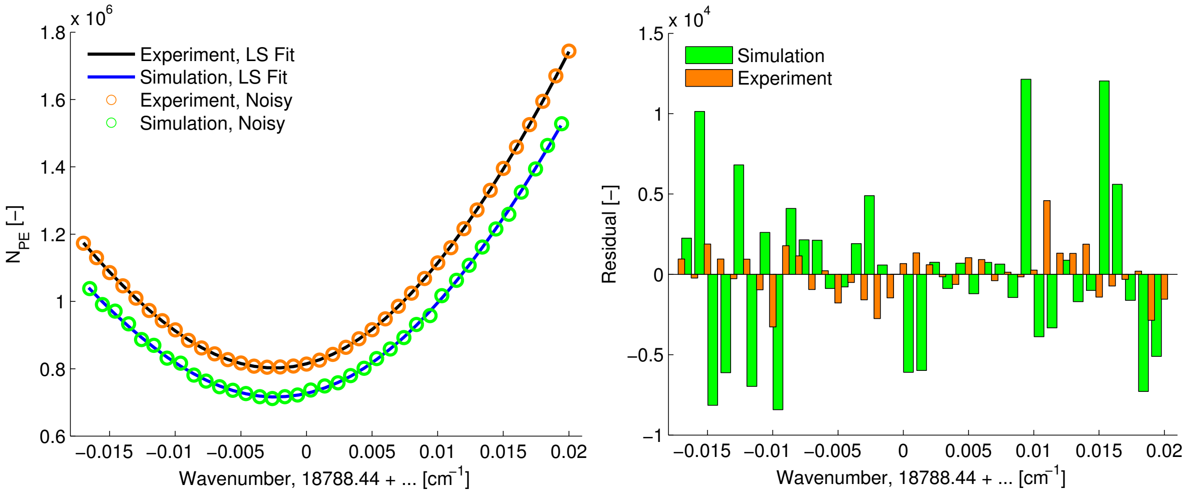

(a) Experiment & simulation spectra (b) Experiment & simulation LS residuals

Figure 6.6: Validation experiment results, case 3

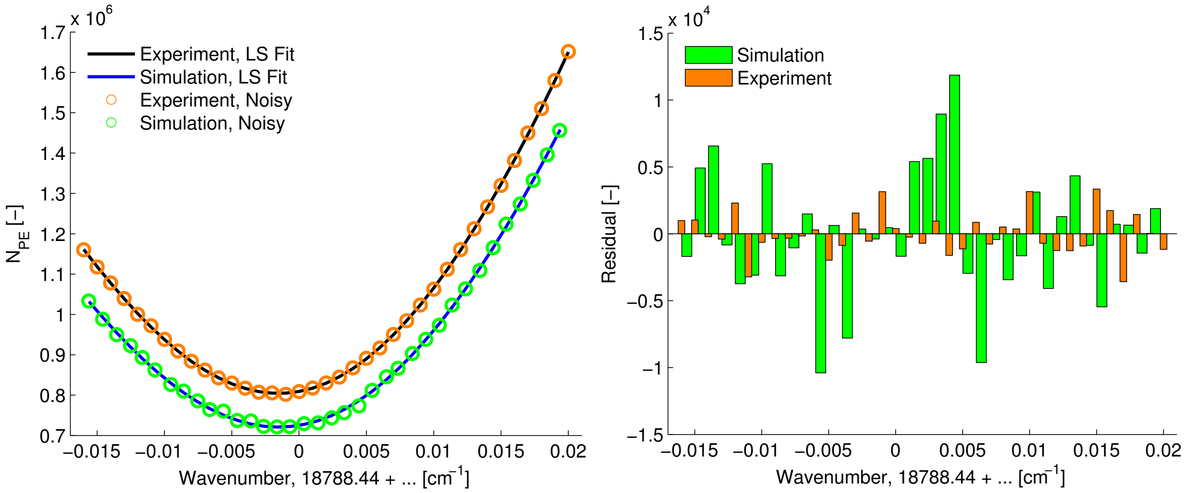

(a) Experiment & simulation spectra (b) Experiment & simulation LS residuals

Figure 6.7: Validation experiment results, case 4

statistical standard deviation. For case 2, it is not so. However, if the confidence interval is increased by multiplying the standard deviation by a factor of 2 or more (> 95% confidence level) and the systematic deviation is also taken into account, then the velocity falls within the expected range. Also the velocity accuracy is limited by measurement uncertainties

Case	P_r (Pa)	P_s (Pa)	T_r (Pa)	T_s (K)	T_c (K)	u_N (m/s)
1	99547	99547	296.15	296.15	296.15	0.00
2	99511	100911	296.15	306.55	305.33	49.83
3	99473	101823	296.15	310.7	308.63	64.81
4	99482	102632	296.15	314.9	312.12	75.34

Table 6.2: Theoretical (real) values

Case	P (Pa)	T (K)	u_N (m/s)
1	99489	296.24	0.09
2	97290	299.22	51.00
3	99902	303.00	64.43
4	101707	307.85	75.31

Table 6.3: Experimental results

Case	$\Delta_\Omega P$ (Pa)	$\Delta_\Omega T$ (K)	$\Delta_\Omega u_N$ (m/s)
1	323	0.01	0.08
2	352	0.01	0.09
3	361	0.02	0.14
4	367	0.02	0.19

Table 6.4: Simulation, small lens angle assumption errors

Case	P (Pa)	T (K)	u_N (m/s)
1	99544 ± 239	296.17 ± 1.33	-0.01 ± 0.57
2	99516 ± 257	305.33 ± 1.52	49.84 ± 0.56
3	99476 ± 267	308.64 ± 1.59	64.81 ± 0.57
4	99483 ± 272	312.14 ± 1.68	75.33 ± 0.58

Table 6.5: Simulation, statistical errors

in the chamber pressure and temperature. The temperature and pressure sensors provide values with a precision of ±0.1°C and ±10 Pa, respectively. There also is a variation in the inlet pressure of ±100 Pa due to the compressor. If these values are propagated through the isentropic relations, one will end up with velocity uncertainties of 2-3 m/s and a temperature uncertainty of ~2 K. These values mark the confidence interval of the experiment and may explain deviations. So, changes in the velocity due to pressure and temperature variations below these limits are to be expected.

The pressure parameter is the least accurate. Due to a low f-number of the collection lens, the small lens angle assumption causes significant uncertainties in pressure. This, if taken into account, will surely affect the statistical uncertainties. In the worst case, statistical and systematic uncertainties will be added. For the cases 1 and 3, the measured pressure falls within the expected uncertainty range (for case 3, the confidence interval needs to be extended). However, for the cases 2 and 4, the measured pressure is outside of the statistically expected ranges.

The measured temperature values are expected to fall within their uncertainty ranges because the systematic uncertainties are negligible. However, that is not the case, since the isentropic relations give the temperature in the potential core of the nozzle with a confidence interval of ±2 K. This deviation could also be explained by an improper alignment of the nozzle. This core extends over a limited distance and gets narrower. If not measured exactly in the core region, temperature values are going to be different because of a convective mixing. Due to spatial constraints, it could not be made sure that the core of the flow passed

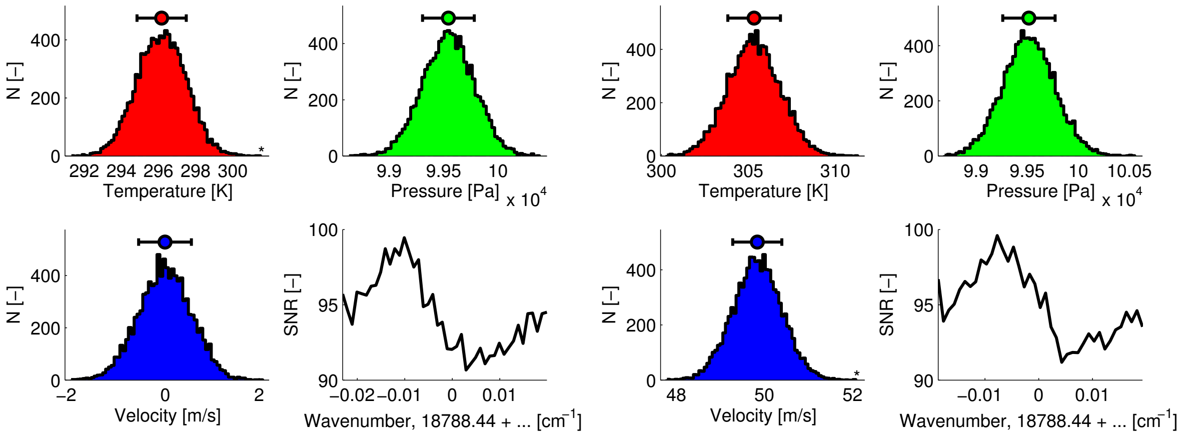

(a) Case 1 (b) Case 2

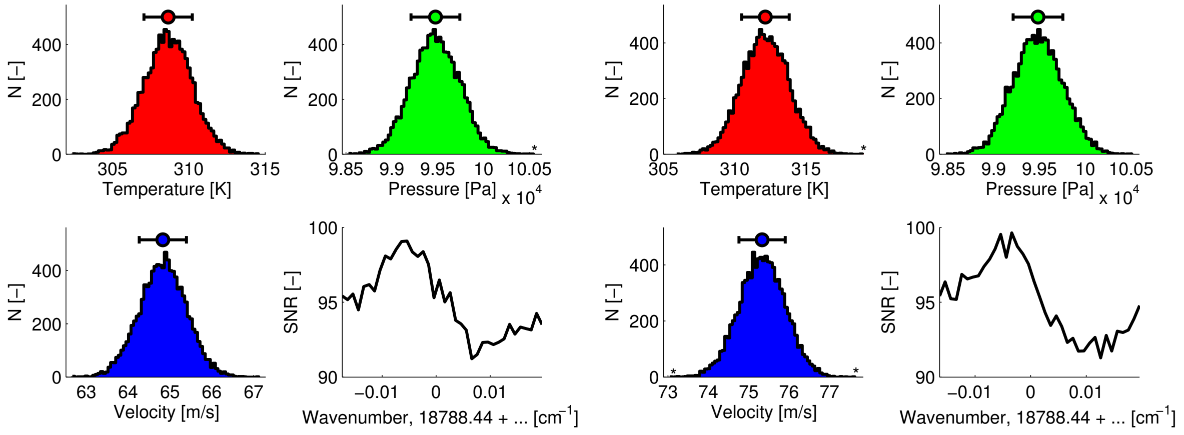

(c) Case 3 (d) Case 4

Figure 6.8: Simulation, statistical distribution of the parameters

exactly through the focal point. This does not affect the velocity as much as the temperature. Since the room temperature is lower than the core temperature, the flow cools down outside of the core. This was the temperature determined in the experiment, since the measurement volume was slightly outside of the core flow. So, the effects of a mixing layer are directly reflected on the temperature. The trend how the temperature increases is same both in the simulation and experiment. Therefore, a better alignment might fix this issue. The statistical uncertainties are most probably not affected.

The main idea behind a validation experiment was not to perform a perfect FSM-FRS measurement and reconstruct the flow parameters exactly. The setup was definitely not optimized for a point FSM-FRS measurement. The goal of an estimate of a signal level and comparing it to the simulations was achieved.

7

Summary

An end-to-end simulator for frequency scanning methods of filtered Rayleigh scattering has been developed in the context of this master thesis. It can simulate several frequency scanning filtered Rayleigh scattering techniques and predict the accuracies in measuring flow temperature, pressure, and velocity. FSM-FRS experiments can be modelled for a variety of optical, environmental, laser, geometric, and simulation parameters. The uncertainty quantification is performed based on systematic and statistical uncertainties. The systematic uncertainties arise from model simplifications and theoretical assumptions. The statistical uncertainties come from random noise in the input parameters. They are quantified with the help of Monte Carlo simulations.

The simulator can be used to model and optimize FSM-FRS experiments or measurement probes. In the context of the DLR project OSIRIS, 3C FSM-FRS probe geometries have been conceived for measuring airplane velocity, off-board temperature and pressure in-flight. Based on calculated statistical uncertainties, different probe parameters have been optimized for maximizing the expected accuracies in pressure, temperature, and velocity.

A validation experiment has been performed to check the accuracy and usability of the end-to-end simulator. A decisive output parameter of the e2e simulator is the expected signal level. The expected FSM-FRS signal level determines the signal-to-noise ratio of a measurement because the shot noise depends on it and the other noise sources (laser power and frequency) are independent of it. So, the main goal of the experiment was to validate the signal level. The experiment was set up at the DLR lab with the available hardware, and the measurements were carried out for different flow cases. The end-to-end simulator was later used to perform simulations for the same setup and flow conditions. The obtained signal levels and shapes from experiments and simulations are in a very good agreement. Therefore, the e2e software has been successfully validated. From now on, it can be used to optimize FSM-FRS experiments or sensors for specific flow conditions.

7.1. Conclusions

After the development, application, and validation of the FSM-FRS end-to-end simulator, the following general conclusions can be drawn:

- When using a laser frequency modulation, the expected uncertainties increase with the modulation amplitude. In general, a direct-detection FSM-FRS is an impressive all-round technique. Using a $1f$ signal of the modulated FSM-FRS results in a low velocity uncertainty but higher temperature and pressure errors. Using a $2f$ signal, on the other hand, gives lower errors in the temperature and pressure but higher uncertainties in the velocity measurements. The FSM-FRS technique with $1f/2f$ signal ratios provides the excellent accuracies in the velocity and temperature, but expects poor precision in the pressure. Also, it is independent of laser intensity fluctuations and background light. This is crucial when performing the measurements in a daylight.

- Only important systematic error is incurred by a small lens angle assumption. However, it is often negligible or very low compared to the statistical errors. The small lens angle assumption error has the biggest impact on the pressure uncertainty. This deviation can be minimized by optimizing the FSM-FRS setup. For OSIRIS, the uncertainties are highest for the geometry 4, arguably because of the geometric constraints.
- When using an FSM-FRS probe in a backscattering configuration with $\theta = 180°$ for measuring a single component of the velocity, the optimized iodine filter lengths are $L = 40$ cm and $L = 45$ cm for $u = 25$ m/s and $u = 250$ m/s, respectively. The saturation temperature of both filters is 85°C. The considered flow temperature and pressure were 225 K and 26500 Pa, comparable to cruise conditions. Splitting the signal into different filters provided no improvement in the expected accuracies of the parameters.
- For measuring all three velocity components, and taking into account all flow parameters, geometry 3 has shown to be superior with a configuration angle of 60°. Geometry 4 has an excellent predicted accuracy in the thermodynamic parameters, but a very poor precision in the velocities. Geometry 2, in general, performs better than geometry 4, but still worse than a geometry 3. When using the $1f/2f$signal with geometry 3, the expected accuracies in the u and w components of the velocity, as well as the temperature, are very close to the values requested by the project. The accuracy in the v-component of the velocity is slightly lower than desired, but still in the same order of magnitude. Pressure parameter is very uncertain and even the direct direct-detection discrete FSM-FRS technique cannot fulfill the accuracy requirement for in-flight application.

7.2. Recommendations

The validation experiment has been performed using the direct-detection discrete frequency scanning method of filtered Rayleigh scattering. Even though the method forms the basis for all the other investigated FSM-FRS approaches, it is desirable to perform additional validation experiments using modulated frequency scanning techniques. This would require a more complex experimental setup, including a lock-in amplifier for detecting the harmonics of a signal. The laser stabilization/modulation will be more challenging as well.

The statistical uncertainties in the flow parameters depend on the expected signal level which has already been validated in the experiment. In addition, it would be interesting to build the 3C FSM-FRS probes and experimentally investigate different flow cases with them.

The mentioned recommendations for the future work are part of the project OSIRIS. Together with this master thesis, only a first stage of the research about the FSM-FRS techniques has been completed. This encompassed a numerical study and a development (validation) of the e2e simulator. The next steps would mostly be comprised of building and testing the FSM-FRS probe prototypes in the laboratory and later on board of airplanes.

Bibliography

[1] H. Barny. New standby lidar instrument (neslie), 2010.

[2] Alexey N. Bashkatov and Elina A. Genina. Water refractive index in dependence on temperature and wavelength: a simple approximation. *SPIE*, 5068:393–395, 2003.

[3] Anthony Bucholtz. Rayleigh-scattering calculations for the terrestrial atmosphere. *Appl. Opt.*, 34(15):2765–2773, 1995. URL `http://ao.osa.org/abstract.cfm?URI=ao-34-15-2765`.

[4] L. M. Caldwell, D. Krueger J. Hair, and C. Y. She. High spectral resolution lidar using an iodine vapor filter at 589 nm. *SPIE*, 2833:40–45, 1996.

[5] Konstantine Cheishvili. Literature review, 2016.

[6] U. Doll, G. Stockhausen, and C. Willert. Endoscopic filtered rayleigh scattering for the analysis of ducted gas flows. *Experiments in Fluids*, 55(3):1–13, 2014.

[7] Ulrich Doll. *Filtered Rayleigh Scattering for simultaneous Determination of pressure, temperature and Velocity fields in gas flows*. PhD thesis, Technical University of Dresden, 2016.

[8] Ulrich Doll, Michael Fischer, Guido Stockhausen, and Christian E Willert. Frequency scanning filtered rayleigh scattering in combustion experiments. In *16th Int Symp on Applications of Laser Techniques to Fluid Mechanics*. The International Symposia on Applications of Laser Techniques to Fluid Mechanics, July 2012.

[9] Andreas Enns. Development of a scattered light sensor for measurement of the parameters based on filtered rayleigh-brillouin and mie scattering. Master's thesis, University of Bielefeld, 2014.

[10] J. N. Forkey, W. R. Lempert, and R. B. Miles. Accuracy limits for planar measurements of flow field velocity, temperature and pressure using filtered rayleigh scattering. *Experiments in Fluids*, 24:151–162, 1998. ISSN 0723-4864. URL `http://dx.doi.org/10.1007/s003480050162`. 10.1007/s003480050162.

[11] J.N. Forkey. *Development and Demonstration of Filtered Rayleigh Scattering: a Laser Based Flow Diagnostic for Planar Measurement of Velocity, Temperature and Pressure*. PhD thesis, Princeton University, 1996.

[12] Jay H. Grinstead, Noah D. Finkelstein, , and Walter R. Lempert. Frequency-locked light scattering: real-time doppler velocimetry with closed-loop feedback control. *Applied Optics*, 37(9):1617–1925, 1998.

[13] John W. Hair, Loren M. Caldwell, David A. Krueger, and Chiao-Yao She. High-spectral-resolution lidar with iodine-vapor filters: measurement of atmospheric-state and aerosol profiles. *Applied Optics*, 40(30):5280–5294, 2001.

[14] HyperPhysics. Broadening of spectral lines, March 2016. URL `http://hyperphysics.phy-astr.gsu.edu/hbase/atomic/broaden.html`.

[15] Jeremy James Jagodzinski. *A Diode Laser-Based Velocimeter Providing Point Measurements in Unseeded Flows Using Modulated Filtered Rayleigh Scattering (MFRS)*. PhD thesis, The University of Texas at Austin, 2007.

[16] Jeffrey Mach and Philip L. Varghese. Frequency-locked light scattering: real-time doppler velocimetry with closed-loop feedback control. *AIAA*, 37(6):695–699, 1999.

[17] Amy F. Mielke, Richard G. Seasholtz, and Kristie A. Elam. Time-average measurement of velocity, density, temperature, and turbulence velocity fluctuations using rayleigh and mie scattering. *Experiments in Fluids*, 39:5280–5294, 2005.

[18] R. Miles and W. Lempert. Two-dimensional measurement of density, velocity, and temperature in turbulent high-speed air flows by uv rayleigh scattering. *Applied Physics B: Lasers and Optics*, 51:1–7, 1990. ISSN 0946-2171. URL `http://dx.doi.org/10.1007/BF00332317`. 10.1007/BF00332317.

[19] R.B. Miles, W.R. Lempert, and J. Forkey. Instantaneous velocity fields and background suppression by filtered rayleigh scattering. In *29th AIAA Aerospace Sciences Meeting*, volume 1, 1991.

[20] R.B. Miles, J.N. Forkey, and W.R. Lempert. Filtered rayleigh scattering measurements in supersonic/hypersonic facilities. In R.B. Miles, J.N. Forkey, and W.R. Lempert, editors, *AIAA, 17th Aerospace Ground Testing Conference*, July 1992.

[21] Richard B Miles, Walter R Lempert, and Joseph N Forkey. Laser rayleigh scattering. *Measurement Science and Technology*, 12(5):R33, 2001. URL `http://stacks.iop.org/0957-0233/12/i=5/a=201`.

[22] C. Y. She. Resonance vapor based lidar for aerosol, temperature, and line-of-sight wind measurements. *SPIE*, 3127:34–41, 1997.

[23] C. Y. She and Jonathan W. Hair Jin-Jia Guo Song-Hua Wu Zhi-Shen Liu Jia Yue, Zhao-Ai Yan. Direct-detection doppler wind measurements with a cabannes-mie lidar: A comparison between iodine vapor filter and fabry-perot interferometer methods. *Applied Optics*, 46(20):4434–4443, 2007.

[24] J. Tellinghuisen. Transition strengths in the visible-infrared absorption spectrum of i_2. *Journal of Chemical Physics*, 76:4736, 1982.

[25] G. Tenti, CD Boley, and R.C. Desai. On the kinetic model description of rayleigh-brillouin scattering from molecular gases. *Canadian Journal of Physics*, 52(4):285–290, 1974.

[26] The Engineering Toolbox. U.S. standard atmosphere, January 2016. URL `http://www.engineeringtoolbox.com/standard-atmosphere-d_604.html`.

[27] David E. Wolf. What is the confocal volume?, 2008.